

energy  
class  
R. ...

2284

**Possibilities for  
Coincidence Spectroscopy  
in the  
Scanning Transmission  
Electron Microscope**

# Stellingen

behorende bij het proefschrift

## Mogelijkheden voor Coïncidentie Spectroscopie in de Raster Transmissie Elektronen Microscop

door

Folbert J. Pijper

1. De betekenis van toevallige samenloop van omstandigheden die in het dagelijks taalgebruik vaak wordt gegeven aan het begrip coïncidentie dient in het kader van dit proefschrift gezien te worden als de foute definitie van coïncidenties, of juist, de definitie van foute coïncidenties.
2. Energiedispersieve coïncidentie spectroscopie tussen energieverlies elektronen en laag-energetische secundaire elektronen leidt tot een beter begrip van de processen die een rol spelen bij de vorming van secundaire elektronen.
3. De kans dat bij het meten van de waarschijnlijkheid van elektronenemissie twee gelijktijdig uitgezonden elektronen als slechts één worden geteld kan aanzienlijk verminderd worden door toepassing van energiselectie op de geëmitteerde elektronen.  
H. Mülleijans and A. L. Bleloch, Phys. Rev. B 46, 8597 (1992).
4. Gezien de hoge sputtersnelheden die op daarvoor gevoelige materialen kunnen ontstaan door focussing van intense elektronen bundels zal enkel-atoom detectie mogelijk zijn door massa analyse van losgesputterde ionen.
5. In een magnetisch eiland in een tokamak plasma behoeven de magnetische oppervlakken géén isothermen te zijn.
6. Om een goede schatting te kunnen maken van de nauwkeurigheid van een meting dienen bij het weergeven daarvan de meetpunten slechts dan met elkaar verbonden te worden wanneer de ruis daarop niet groter is dan de voor een goede weergave benodigde lijndikte.
7. Het feit dat de erkenning van gewetensbezwaren tegen vervulling van de militaire dienst beloond wordt met een vervangende dienst die één derde langer duurt dan de normale dienstplicht, is een indicatie van de onoprechtheid van die erkenning.
8. De werking van de wet op de ruimtelijke ordening demotiveert agrarische ondernemers zich actief bezig te houden met aanleg en onderhoud van landschapselementen.

**Possibilities for  
Coincidence Spectroscopy  
in the  
Scanning Transmission  
Electron Microscope**

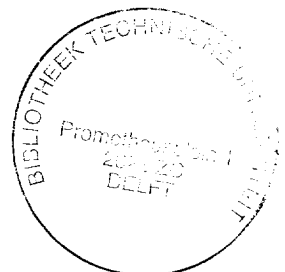
**Proefschrift**

Ter verkrijging van de graad van doctor  
aan de Technische Universiteit Delft,  
op gezag van de Rector Magnificus,  
Prof. ir. K. F. Wakker,  
in het openbaar te verdedigen  
ten overstaan van een commissie  
aangewezen door het College van Dekanen,  
op maandag 20 september 1993 te 16.00 uur

door

**Folbert Jaco Pijper**

geboren te Spijkenisse,  
natuurkundig ingenieur.



Dit proefschrift is goedgekeurd door de promotor  
Prof. dr. ir. P. Kruit

This work was part of a research program of the Foundation for Fundamental Research on Matter (FOM) and financially supported by the Netherlands Technology Foundation (STW), under Contract No. DTN 44-0745.

Pijper, Folbert Jaco

Possibilities for coincidence spectroscopy in the scanning transmission electron microscope / Folbert Jaco Pijper.

Proefschrift Delft. – Met lit. opg. – Met samenvatting in het Nederlands.  
ISBN 90-9006443-5

Copyright © 1993 by F. J. Pijper

Printed in the Netherlands.

drukkerij Elinkwijk — Utrecht — 1993

# Contents

<b>List of Figures</b>	<b>v</b>
<b>Preface</b>	<b>vii</b>
Organization of the Thesis	viii
References	viii
<b>Acknowledgements</b>	<b>ix</b>
<b>1 Introduction</b>	<b>1</b>
1.1 Spectroscopy in the STEM	1
1.1.1 Emitted-Electron Detection in the STEM	3
1.1.2 Electron Energy-Loss Spectroscopy	4
1.2 Coincidence Techniques	4
1.3 Historical Overview	5
1.3.1 ( <i>e, 2e</i> ) Experiments on Gases	5
1.3.2 ( <i>e, 2e</i> ) Experiments on Solids	6
1.3.3 Coincidence Techniques in the Electron Microscope	7
1.4 Possible Applications	9
1.4.1 Virtual-Photo Electron Spectroscopy	10
1.4.2 Coincident Auger Spectroscopy	11
Background Reduction	11
Identifying Specific Auger Features	12
Improving Spatial Resolution in Secondary-Electron Imaging	13
1.4.3 Coincident Energy-Loss Spectroscopy	14
Surface Sensitivity	14
Background Reduction	15
1.4.4 Absolute Detection Efficiencies	17
1.5 References	17
<b>2 Physics of Coincidence Spectroscopy</b>	<b>21</b>
2.1 Possible Processes at Electron Impact	22
2.1.1 Single-Electron Interaction	22
2.1.2 Collective Interaction	24
2.1.3 Delocalization	24

## Contents

2.2	Single-Electron Scattering	25
2.2.1	Energy Conservation	26
2.2.2	Momentum Conservation	29
	Angular Emission Distribution for Free Atoms	32
	Angular Emission Distribution for a Solid	35
	Selection of Momentum Transfer in the STEM	39
2.3	Transport to and Escape from the Surface	40
2.4	Comparison with Photo Absorption	42
2.4.1	Comparison of Energy and Momentum Transfer	42
2.4.2	Comparison of Excitation Probability	43
2.5	References	46
<b>3</b>	<b>Instrumental Aspects of the Coincidence Experiment</b>	<b>49</b>
3.1	Probe Formation	50
3.1.1	Relation between Probe Forming Parameters	50
	Squared Summation Approach	51
	Wave-Optical Approach	53
3.1.2	Acceleration Voltage	55
3.1.3	Energy Spread	57
3.1.4	Probe Current	58
3.1.5	Probe Size	58
3.1.6	Illumination Opening Angle	59
3.1.7	Non-Rotationally Symmetric Aberrations	59
3.1.8	Instabilities	59
3.1.9	Conclusions on Probe Formation	60
3.2	Energy-Loss Measurement	60
3.2.1	Pre-Spectrometer Optics	61
3.2.2	Spectrometer Optics	61
3.2.3	Post-Spectrometer Optics	62
3.2.4	Energy Resolution Versus Acceptance Angle	62
3.3	Emitted-Electron Measurement	65
3.3.1	Parallelizer	65
	Timing Accuracy	67
3.3.2	Transfer Optics	67
	Aberrations of the transfer optics	69
	Timing Accuracy	70
3.3.3	Spectrometer Optics	71
	Timing Accuracy	71
3.3.4	Modes of Operation	72
	Maximizing number of channels at 100 % transmission	72
	Constant $\Delta U$ at 100 % transmission	74
	Maximizing the product of number of channels and transmission	75

Concluding remarks on operating mode for transfer optics	78
3.3.5 Post-Spectrometer Optics	81
3.4 Electron Detection	83
3.4.1 Slow-Electron Detection	84
Background Signals	85
3.4.2 Fast-Electron Detection	85
Background Signals	87
3.4.3 Parallel Electron Detection	88
3.5 Coincidence Parameters	92
3.5.1 False Coincidences	93
3.5.2 True Coincidences	94
3.5.3 True to False Ratio	94
3.5.4 Signal-to-Noise Ratio	95
Single Atom Identification	98
3.6 References	100
<b>4 Setup of the Prototype Experiment</b>	<b>105</b>
4.1 Microscope Column	105
4.1.1 Emitted-Electron Analyzer	107
4.1.2 Electron Energy-Loss Analyzer	108
4.2 Coincidence Electronics	108
4.3 Specimens	109
4.4 Experimental Difficulties	110
4.5 References	111
<b>5 Results of the Measurements</b>	<b>113</b>
Abstract	113
5.1 Introduction	113
5.2 Experimental Setup	116
5.3 Results and Discussion	122
5.4 Acknowledgments	129
5.5 References	129
<b>6 Conclusions and Perspectives</b>	<b>131</b>
6.1 Conclusions	131
6.2 Perspectives	135
6.3 References	136
<b>Summary</b>	<b>137</b>
<b>Samenvatting (Dutch Summary)</b>	<b>139</b>
<b>Curriculum Vitae</b>	<b>141</b>

## List of Figures

1.1	Schematic STEM.	2
1.2	Schematic 2-D secondary-EELS coincidence spectrum.	9
1.3	Schematic Auger coincidence spectra.	12
1.4	Fluorescence yield as a function of $Z$ and energy.	15
1.5	Schematic energy-loss coincidence spectra.	16
2.1	Band-level diagram of electron impact processes.	23
2.2	Schematic band structure of a solid with expected emission spectrum.	26
2.3	Example EELS spectrum of thin carbon foil.	27
2.4	Momentum diagram of the scattering event.	30
2.5	Angle between momentum transfer vector and the normal to the incoming electrons as a function of scattering angle.	32
2.6	Angular probability distribution of momentum transfer.	33
2.7	Angular probability distribution for given $E$ and $k_e$ .	34
2.8	Angular emission probability distribution.	35
2.9	Construction of momentum of emitted electron.	37
2.10	Construction of momentum of emitted electron, $\alpha_{acc} < 90^\circ$ .	38
2.11	Required initial upward momentum as a function of energy loss.	38
2.12	Angular emission probability distribution from solid.	39
2.13	Mean free path for inelastic scattering.	41
2.14	Ratio between electron excitation and photoabsorption cross section.	44
2.15	Comparison of spectral brightness and flux density data.	45
3.1	Parameters of the illumination.	50
3.2	Radial current density distribution	54
3.3	Electron excitation cross section as function of acceleration voltage.	56
3.4	Signal strength as function of acceleration voltage.	57
3.5	Best possible EELS resolution as function of acceptance angle.	63
3.6	Acceptance angle as function of acceleration voltage	64
3.7	Schematic transfer optics between parallelizer and $180^\circ$ analyzer.	68
3.8	Transit time spread as a function of opening angle.	72
3.9	Required magnification of transfer optics for optimum energy resolution.	75
3.10	Required pass energy for optimum energy resolution.	76
3.11	Obtainable energy resolution at 100 % transmission.	77



## List of Figures

3.12	Required potential at central radius of $180^\circ$ analyzer.	78
3.13	Number of energy channels times transmission as a function of initial energy.	79
3.14	Obtainable transmission for fixed pass energy and energy resolution.	80
3.15	Lower bound for angular transmission due to parallelizer action	81
3.16	Transmitted intensity for cosine distribution.	82
3.17	Actual transmission for cosine distribution.	82
3.18	Schematic slit-scintillator-photomultiplier detector.	86
3.19	Principle of a position-sensitive detector.	88
3.20	Principle of a detector with individual timing electronics.	90
3.21	Principle of a detector with combined timing electronics.	90
3.22	Schematics for doing both regular and coincidence spectroscopy.	91
3.23	Schematic time-delay spectrum.	96
3.24	Signal-to-noise ratio for fixed dwell time.	97
3.25	Signal-to-noise ratio for fixed dose and dose density.	98
3.26	Signal-to-noise ratio for single atom detection.	99
3.27	Energy differential cross sections for $K$ - and $L$ -shell edges.	100
3.28	Influence of energy resolution on signal-to-noise ratio.	101
5.1	Microscope column used for coincidence measurements.	117
5.2	Low-energy-range secondary electron spectrum.	119
5.3	Semilogarithmic plot of the secondary-electron spectrum.	119
5.4	Schematic coincidence setup.	120
5.5	MCA time difference spectrum.	121
5.6	Large energy range coincident and normal energy-loss spectra.	122
5.7	Ratio of coincident and normal energy-loss spectrum.	124
5.8	Low-energy range coincident and normal energy-loss spectrum.	125
5.9	Low-energy range ratio spectrum.	125
5.10	Series of energy-loss coincidence spectra.	127
5.11	Positions of the energy offset and Gaussian peak in the 2-D coincidence spectrum.	128

## Preface

This thesis presents a survey of the possibilities of coincidence spectroscopy techniques in a scanning transmission electron microscope (STEM). The survey is focussed on coincidences of electrons detected by electron energy-loss spectroscopy (EELS) and by emitted-electron spectroscopy. It is shown how coincidence spectroscopy can be realized in the STEM and first coincidence results are reported. Coincidence techniques are not trivial and require careful consideration of many complicating aspects. The discussion of physical interaction processes and instrumental requirements in this thesis may serve as a basis for such considerations.

The work described here was started in 1987 in the Delft Research Group for Particle Optics. It forms part of the so-called 'High resolution Auger project', a research program of the Foundation for Fundamental Research on Matter (FOM), which was initiated by Pieter Kruit. The parallelizer objective lens,<sup>1,2</sup> which enables through-the-lens detection of emitted electrons, forms the basis for both secondary-electron and Auger-electron analysis systems. In a scanning electron microscope (SEM) Luc Dubbeldam used secondary-electron analysis as a method for voltage-contrast detection on integrated circuits.<sup>3</sup> The integration of an Auger-electron analysis system into an existing STEM, was part of Arno Bleeker's work. This prototype STEM was used to test the optical principles, but lacked clean specimen conditions. He therefore concentrated on the design of an ultrahigh vacuum (UHV) microscope for Auger analysis.<sup>4</sup> The non-UHV prototype became available for the coincidence experiments described here.

By adding an EELS system and coincidence electronics, we hoped to achieve a proof of principle for the coincidence technique. Further measurements were planned to be done on the new UHV microscope. Unfortunately we were forced to abandon the ideas for UHV experiments due to delays in construction.

A STEM is a complex instrument with many knobs and buttons required for the control of current supplies for lenses, deflectors etcetera. The modifications that have been made to the microscope have changed many of these controls. Even 'normal' operation of the modified instrument requires a lot of additional manipulations. Also many new controls were added for adjusting the imaging conditions in the additional parts. Partly because we did not fully realize all experimental requirements, and also because of some instrumental setbacks, it took quite some time to realize coincidence conditions. From the moment a small number of true coincidences were observed, the microscope and analyzer settings, electronics and software could be gradually improved to achieve reproducible results.

Although the instrument was not equipped with ultrahigh vacuum and lacked the ability of nanometer probes, some interesting experiments have been done, which are reported in this thesis. The analysis of instrumental aspects for coincidence spectroscopy, given in this thesis, may serve as a basis for experiments which could not be performed in the prototype instrument.

## Organization of the Thesis

Spectroscopy techniques in the STEM and the idea of coincidence methods are introduced in the first chapter. A historical overview summarizes former work on coincidence spectroscopy, as far as it can be of interest for application in a STEM. Several possible applications are discussed, partly based on this former work, some specific for the situation in a high resolution STEM.

Chapter 2 gives information on the physical processes and theories that are important for the selection of interesting phenomena and interpretation of coincidence spectra. A description of chances involved in these processes (cross sections) will enable a comparison with photo electron spectroscopy.

The settings of the microscope, the analyzers and the coincidence electronics can strongly influence the quality of the spectra and the information that can be extracted from them. These instrumental aspects will be discussed in Chapter 3.

Following this, in Chapter 4 a description will be given of the experimental coincidence setup as it was built in the laboratory in Delft. This setup was used for obtaining the results discussed in Chapter 5. The text of Chapter 5 was published in Phys. Rev. B, under the title: 'Detection of energy-selected secondary electrons in coincidence with energy-loss events in thin carbon foils', by Folbert J. Pijper and Pieter Kruit. The conclusions of the survey and an outlook toward future developments of coincidence spectroscopy in the STEM form the closing chapter of this thesis.

## References

- <sup>1</sup> P. Kruit and F. H. Read, *Magnetic field paralleliser for  $2\pi$  electron-spectrometer and electron-image magnifier*, J. Phys. E **16**, 313 (1983).
- <sup>2</sup> P. Kruit, *Magnetic Through-the-lens Detection in Electron Microscopy and Spectroscopy, Part 1*, Vol. 12 of *Advances in Optical and Electron Microscopy*, p. 93. (Academic Press Limited, London, 1991).
- <sup>3</sup> L. Dubbeldam. *A voltage contrast detector with double channel energy analyzer in a scanning electron microscope*. PhD thesis, Delft University of Technology, November 1989.
- <sup>4</sup> A. J. Bleeker. *Optical and mechanical design for 1 nm resolution Auger spectroscopy in an Electron Microscope*. PhD thesis, Delft University of Technology, June 1991.

## Acknowledgements

The realization of this thesis would not have been accomplished without the continuing support of many people around me.

First of all I want to thank my promotor Pieter Kruit who kept stimulating me in my research, especially during the preparation of the thesis. My colleagues Arno Bleeker and Luc Dubbeldam I would like to thank for the close cooperation in the Auger project. I thank Robert Endert and Pybe Faber who contributed to this research in their work for their Master's degree. Pybe also should be thanked for a lot of discussions during the final stages of preparing the thesis. A lot of technical support was provided by André van Latenstein van Voorst. With their Master's work, Rudolf van Aken, Anne Pals Bleeksma and Anton de Jager also contributed to the Auger project.

For many fruitful discussions and teabreaks I thank my colleagues, Jim Barth, Pim Heerens, Erico Koets, Karel van der Mast, Jacques Nonhebel, Jan Peter Adrijaanse, Arjan Buist, Joan Koffeman, Bram Koster, Era Mulder, Jan Simons, Leon Seijbel, Rik Slingerland, Luc Vijgen, and Tom van Zutphen. Bram Huis I thank for support with small projects in the workshop, Peter van der Reijken for all the repairs I could do on my bike, and Mijnheer Staneke for all the clean towels.

Boemi Lencová, Erik van Straten, Astrid Verweij, and Mattijn Zaalberg I especially thank for the funny side of working in the research group. Of course also the students Joep Brouwers, Frits Gehring, Sander Gubbens, Mario Hoek, Taco Hoekstra, Patrick de Jager, Cécille de Pierre, Hans de Ruyter, Egbert Schrotten, Michiel van der Stam, Erik van der Steen, Anneke Vemer, Jan Vermeer, Leo van Vliet, Jeroen Vroemen, Elsbeth van Wely, Geurt Wisselink, Erwin van Zwet, and all other colleagues contributed to this pleasant atmosphere.

My colleagues at Rijnhuizen are thanked for the continued interest they expressed in the progress of this thesis.

My 'Centraal Wonen' inmates Marian Brounné, \*eric Hordijk, Piet and Thekla van Lingen, Toine Poelmans, Monique Toonen, Jessika and Margo van der Valk are thanked for not making too much fuss when I was late again for dinner.

My brother Roeland-Jan and both my parents I thank for all the mental support they provided in the past years.

Most of all I would like to thank my dearest friend Janneke Blijdorp, who stood beside me as long as I know her.

August 1993

Folbert J. Pijper

# 1. Introduction

This thesis describes the possibilities which arise in electron microscopy when existing analytical techniques are combined by means of coincidence techniques. In electron microscopy more and more effort is being put in the development of analytical techniques, to improve the elemental and chemical characterization of small structures. Likewise, in surface-sensitive analytical instrumentation a trend toward better spatial resolution is observed. Obviously these techniques are aiming at the same final goal: *High spatial-resolution surface-sensitive elemental and chemical analysis*. Recent progress in electron microscopy design has brought this goal within reach. A secondary- and Auger-electron analyzer with high collection efficiency can now be incorporated into a high-resolution scanning transmission electron microscope (STEM). The combined use of this analyzer signal with the electron energy-loss analyzer signal, adds a new dimension to electron microscopic analysis, provided it is done in a coincidence set-up. Coincidence techniques employ the fact that if two electrons are detected at the same time in different detectors, they most likely originate from a single interaction event of a primary electron with the specimen. Individual scattering events can then be studied simultaneously with two analytical techniques. This thesis emphasizes the importance of some possible applications, with a general account of the physical and experimental parameters. The first experimental results which are obtained with a prototype set-up are shown as examples of interesting applications.

## 1.1. Spectroscopy in the STEM

The impact of fast electrons on the sample in a STEM can cause many excitation and ionization processes; see, e.g., Sect. 2.1. These processes, or the subsequent de-excitation processes, can be studied in several ways. Existing analytical techniques that are often used in STEMs are diffraction, energy- and wavelength-dispersive x-ray analysis (EDX and WDX) and electron energy-loss spectroscopy (EELS). This range of techniques is now extended with emitted-electron spectroscopy. Fig. 1.1 shows (schematically) the STEM that is used in this research, which is equipped with some of these analytical techniques. The EDX detector (not shown) can be added on one of the ports at the specimen level.

Diffraction can give information on lattice parameters. Only in an indirect way this can tell something about the elemental constitution. For diffraction the

## 1. Introduction

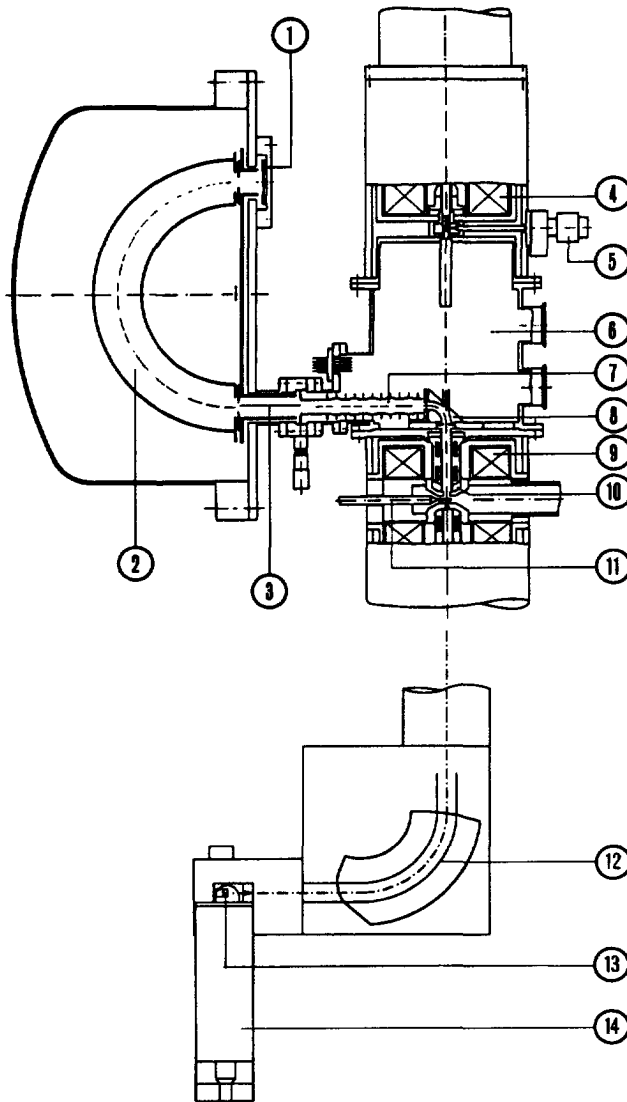


Fig. 1.1: Schematic cross section through the STEM column used for the coincidence measurements. The electron gun (not shown) is situated on top of the microscope column (top right). Numbers 1-3, 6-8 and 10 are required for the emitted-electron detection, numbers 12-14 are part of the energy-loss detector. (1) Micro-channel-plate detector, (2) 180° analyzer, (3) beam defining slits, (4) second condenser lens, (5) condenser diaphragm, (6) microscope extension, (7) electrostatic lenses, (8) 90° deflector, (9) objective lens, (10) parallelizer coils, (11) specimen holder, (12) EELS spectrometer, (13) scintillator, and (14) photomultiplier.

primary electron beam should not be focussed on the sample, so that very high spatial resolution is not possible. X-ray analysis uses the deexcitation process of x-ray emission, the competitor of Auger-electron emission. Only at higher energies (above 10 keV) the cross section for x-ray emission is larger than for the Auger process. Because of the large distance x-ray photons can travel before being absorbed, the spatial resolution of x-ray analysis is limited by the spreading of the incoming electrons. For the same reason x-ray analysis is not very surface sensitive. Furthermore, the limited acceptance angle of the detector leads to small collection efficiency, especially for wavelength-dispersive systems. Energy-dispersive detectors do not offer high energy resolution and this leads to overlapping spectral features.

In the following emitted-electron energy measurement and energy-loss measurement will be discussed. The coincidence technique discussed in this thesis, is based on an appropriate combination of both.

### 1.1.1. Emitted-Electron Detection in the STEM

Fast electron impact causes the emission of electrons from a sample. Energy analysis of these emitted electrons can yield information about the sample. How good this can be done depends on primary electron beam intensity and spotsize, as well as on collection efficiency of the emitted electrons. For both primary and emitted electrons, lenses should be placed as closely as possible to the sample. Without integration of these lenses, a compromise between probe characteristics and collection efficiency should be made. With the recent development of a magnetic bottle type through-the-lens analysis system this limitation has been overcome so that small probes and high collection efficiency for emitted electrons can be combined.

Emitted electrons are generally classified according to their production mechanism. *Direct knock-out electrons* are originally bound to the atoms and molecules of the sample. They are knocked out by the impact of the fast electron. *Auger electrons* are those electrons that are created when vacant positions in inner shells (created by the impact of the fast electron) are reoccupied by electrons from higher bands. The energy released in this process is transferred to the Auger electron, which can then escape. An alternative for Auger electron emission is x-ray emission, which becomes favorable at higher transition energies. *Cascade electrons* are slow electrons (between 0–50 eV), that are created in a cascade process, started by a direct knock out or Auger electron. The cascade electrons release on average more than one (slower) electron on their way through the sample. It is these electrons which are generally called *secondary electrons*. *Plasmon decay electrons* form another possible contribution for electron emission. A plasmon (a collective electron oscillation) is excited by the passing of the fast electron and decays by creation of electron-hole pairs.

The new possibility to equip a STEM with a very surface sensitive secondary and/or Auger electron analysis system is discussed in detail by Bleeker.<sup>1</sup> Since the modifications implied by this development are not too drastic, other analytical

techniques can still be used simultaneously.

### 1.1.2. Electron Energy-Loss Spectroscopy

Of the existing analytical techniques, EELS offers the best spatial resolution, given by the electron beam probe size. EELS also has a large collection efficiency due to the predominantly forward scattering cross section. The energy-loss measurement can only be performed on electrons that have been transmitted through a thin sample. The main disadvantage of EELS is that it gives broad spectral features on a large background, which complicates interpretation. Of course any excitation or ionization process should be accompanied by a primary-electron energy loss. Therefore EELS is especially suitable for coincidence techniques, in combination with other spectroscopies.

## 1.2. Coincidence Techniques

Using the information from two available analytical techniques can yield more information than just two spectra. Each spectrum gives statistical information on only one scattering product. The information that is not available in the combination of the two spectra is how these scattering products relate to each other. This information can only be extracted if all individual occurrences are registered separately. This brings us to the use of coincidence techniques.

In many experiments, coincidence techniques have been used to exclude specific background contributions. Coincidence techniques are well known in nuclear physics, e.g., to register the simultaneous creation of two or more elementary particles. Also in molecular physics or chemistry coincidence techniques are known, e.g., to study the Auger decay of selected excitations.

The STEM *coincidence techniques* select those events (occurring in the specimen) that yield an electron in both detectors. A *coincidence spectrum* is built up by counting the occurrences of the simultaneous detection of two electrons in the two respective detectors as a function of the setting of one or both detectors.

Ideally, simultaneous detection could be based on detection of the two electrons in an infinitely small time interval. In practice so-called time jitter exists, so that the criterion for simultaneous detection must be based on a finite time interval. It then becomes possible that two electrons from unrelated events cause the registration of a coincidence. Such a coincidence is called a *false coincidence*, as opposed to the desired *true coincidences*. Therefore, to be able to make a good distinction between true and false coincidence signals, a reduction of primary beam current is necessary. This implies that, to become a useful technique, coincidence spectroscopy requires two analytical techniques with high collection efficiency. The best choices are the EELS and the now available secondary/Auger electron analyzers.

With the energy-loss analyzer the amount of energy transferred by the collision is selected. With the secondary-electron analyzer the kinetic energy of the emitted



electron is determined. The difference between the two gives information on the energy band structure of the target sample.

### 1.3. Historical Overview

One of the most important requirements for coincidence methods is the possibility to register the arrival of single particles. Without this a mixing of information of different events will make coincidence techniques useless. Furthermore the registration of these single particles must be performed fast compared with the time in between arrivals of the subsequent particles. This means that only with the availability of faster detectors the countrates in coincidence experiments reach practical (statistically interesting) values. The first single-particle detectors were used in coincidence experiments in the field of elementary particle physics.

An example of one of the early coincidence experiments is a  $(p, 2p)$  experiment by Chamberlain and Segré<sup>2</sup> which served to determine the distribution of proton momenta in lithium nuclei. The term  $(p, 2p)$  signifies an experiment with one incoming proton (in their case of 340 MeV) and two outgoing protons that are detected in coincidence as a function of (scattering- or emission-) angle. No proton energies were determined.

The first coincidence experiments which involve one incoming and two outgoing electrons, and accordingly named  $(e, 2e)$  spectroscopy, were performed to get information on electronic wavefunctions of atoms or molecules. For a full wavefunction mapping one needs to know the energies of the scattered and ejected electron plus the momenta or, equivalently, the angles of both electrons. With the energy of the incoming electron known, a reconstruction can be made of the original (pre-collision) momentum of the knocked out electron. By scanning one of the parameters an energy-resolved electron-momentum distribution can be found.

Experiments meant to provide data on momentum distributions are most often binary  $(e, 2e)$  experiments. The term binary results from the fact that for high momentum transfers one approaches the situation of 'binary' scattering off a free electron. The ejection of the electron will be confined to the direction of the momentum transfer with some distribution around this direction due to its initial momentum distribution.

Coincidence  $(e, 2e)$  experiments can be performed on gases as well as on solids. In gases, where no dense material is present around the position where the collision takes place, no loss of signal arises. In a solid the limited escape depths or, equivalently, a finite mean free path can cause a large loss of secondary or transmitted electrons. Furthermore, interpretation can become more complicated due to multiple scattering effects.

#### 1.3.1. $(e, 2e)$ Experiments on Gases

One of the first coincidence experiments yielding the angular correlation of the scattered and ejected electrons was performed by Ehrhardt *et al.*,<sup>3</sup> with slow

## 1. Introduction

(50 and 114 eV) electrons incident on a beam of helium atoms. In this reference a time resolution of 10 nsec is obtained.

Van der Wiel<sup>4</sup> introduced a small-angle scattering experiment with 10 keV electrons on light noble gases. The dipole approximation, which becomes valid at such small angles, allows a comparison with photoionization and -absorption data. The distribution of ejected electrons becomes identical with that of photoelectrons ejected by radiation with linear polarization along the momentum-transfer direction. Furthermore, new data can be expected in energy regions that are accessible only by synchrotron radiation sources. A suggestion was made that a scattering experiment with fast electrons might be preferable to the use of a synchrotron. Such a near-dipole ( $e, 2e$ ) experiment was performed on neon<sup>5</sup> to give a photoelectron angular distribution for the 2p electrons, measured in the 4–35 eV region above threshold using 3.5 keV electrons. The data agreed well with existing theory.

Studies on N<sub>2</sub> and CO molecules in which the scattered electron was detected in coincidence with positive ions, provided information on the decay processes following  $K$ -shell excitation and ionization.<sup>6</sup>

Haak *et al.*<sup>7</sup> performed a core-level near-dipole ( $e, 2e$ ) experiment to study the Auger decay processes resulting after electron-impact excitation or ionization. The measurement setup was based on a very large cylindrical mirror analyzer originally built for x-ray photoelectron spectroscopy by Citrin *et al.*<sup>8</sup> Differences between spectra obtained in coincidence with energy losses representing excitation (no ejection of the core electron) and ionization (the core electron leaves the atom or molecule) gave new and unexpected information on intensities of satellites occurring in core-level photoemission spectra; see Ungier and Thomas.<sup>9</sup>

Similar experiments where the carbon or oxygen 1s electron of CO is excited to a molecular ( $2\pi$ ) orbital, resulted in so-called autoionization Auger spectra.<sup>10</sup> Different spectral features were recognized, where the excited electron was participating in the decay or just remained spectator (cf. Section 1.4.2).

### 1.3.2. ( $e, 2e$ ) Experiments on Solids

Amaldi *et al.*<sup>11</sup> were the first who succeeded in performing a binary coincidence experiment on a thin carbon foil with incoming electrons of 14 600 eV. The two outgoing electrons had equal energies of half this amount and were detected under 45° angles. The obtained energy resolution was 150 eV, which enabled the resolution of the carbon  $K$ -edge for different values of initial momentum. Time resolution reported with two channeltron detectors was 4.3 nsec.

A first detailed mapping of a wavefunction of the  $K$ -shell of carbon was obtained by Camilloni *et al.*<sup>12</sup> using 9 keV electrons. The energy resolution of 45 eV in this experiment was not enough to distinguish the 2p and 2s states in the  $L$ -shell.

A similar study was performed by Krasil'nikova *et al.*<sup>13</sup> and revealed the shape of the momentum distribution function for the carbon as well as the oxygen  $K$ -shell in collodion films, using 10–15 keV electrons. For these experiments an energy resolution of 140 eV is reported.

Later these studies were extended to aluminum films,<sup>14,15</sup> where with an improved energy resolution of  $\approx 8$  eV a series of momentum distributions could be made for different energy states of the target electrons.

The first ( $e, 2e$ ) experiment that gave sufficient resolution to observe structure in the valence band was performed by Ritter, Dennison, and Jones.<sup>16</sup> Using 20 keV electrons, two separate bands with different momentum distributions were distinguished. This could give clues to the occurrence of different bonding types between the carbon atoms in the film.

The first detailed core-level information was revealed by a technique, called Auger-photoelectron coincidence spectroscopy or APECS. In a photoionization experiment Haak and co-workers<sup>7,17,18</sup> detected Auger electrons in coincidence with photo electrons. It was used to study Cu  $L_{23}M_{45}M_{45}$  Auger transitions on a copper surface. Extra surface sensitivity is realized because both electrons have to escape from the surface. With about 4-eV energy resolution adequate separation of the  $L_2$  and  $L_3$  photoelectrons was obtained. Spectra obtained with this technique were clearly showing that only certain selected spectral features remain, which made interpretation easier and helped in identifying peaks in direct Auger spectra, even with the much lower counting rates. Time resolution reported for this experiment was about 16 nsec.

Recently, very low primary beam energy (5–100 eV) coincidence spectroscopy experiments have been reported by Kirschner *et al.*<sup>19</sup> They observed single electron-electron scattering between the primary electron and a valence-band electron in a back-reflection setup, and were able to give semi-quantitative estimates on the probability of such events.

### 1.3.3. Coincidence Techniques in the Electron Microscope

The first one who employed coincidence techniques in an electron microscope was Voreades.<sup>20</sup> In a UHV scanning electron microscope he detected energy-loss electrons in coincidence with all secondary electrons. The primary energy was about 20–25 keV. No energy analysis on the secondary-electron detector was available. His work was directed toward the question of secondary-electron production mechanisms. Main conclusion of this work was that the predominant production of secondary electrons is a result of energy losses of about 20 eV and that this happens with an efficiency of about 5%. To decide whether this meant that secondary electrons were produced as a result of plasmon decay, as suggested by Gornyi,<sup>21,22</sup> or due to interband transitions, as suggested by Willis *et al.*,<sup>23</sup> Voreades concludes that the loss spectrum should be recorded with higher energy resolution and that secondary-electron energy analysis is required. In fact this type of experiment is reported in Chapter 5 of this thesis.<sup>24</sup>

Voreades further estimated the (average) escape depth of the secondary electrons to be approximately 3 nm. Apart from the loss of kinetic energy information on the secondary electrons, there is no angular information available (due to the detection method employed).

## 1. Introduction

The first research using coincidence techniques in the electron microscope that was directed at improving the detection limits of EELS and EDX was carried out by Kruit, Shuman and Somlyo.<sup>25</sup> In a STEM equipped with EELS and EDX detectors, coincidences between x-rays and energy-loss events were established. A low background in the coincident x-ray spectrum was found. Due to the relatively slow EDX detector high countrates could not be achieved, resulting in spectra with rather poor statistics. Results show that with a timing filter amplifier and constant fraction discriminator for the x-ray pulses a time resolution of about 100 nsec is possible.

When no timing filter amplifier was used, for example by Nicolls *et al.*<sup>26</sup> the time resolution was limited to about 300 nsec, which implied low countrates and poor statistics.

Wittry<sup>27</sup> suggested the use of coincidence techniques to improve the detection limits of electron spectroscopy in STEM.<sup>28</sup> In particular the use of Auger electrons in coincidence with the energy-loss electrons is suggested for specimens consisting of a few monolayers of light material ( $Z \lesssim 30$ ) on top of a carbon substrate. For such a specimen, he concludes, even with a retarding field analyzer an improvement in detection limits is theoretically possible.

In an exploration of the detection limits of Auger electron spectroscopy Cazaux<sup>29</sup> also considered the coincidence detection of Auger electrons with the energy-loss electrons. He claimed that the sensitivity of detecting small concentrations could be increased by two orders of magnitude by using very weak beam intensities and long acquisition times. Also the minimum number of detectable atoms should decrease in spatially resolved measurements. In his conclusions, despite (at that time) the impassable combination of nanometer probes and efficient Auger analysis, he foresees "that chemical identification of a single atom will be possible by Auger analysis in the next few years".

In Delft the coincidence spectroscopy project is being extended toward ultra-high vacuum conditions, nanometer sized probes and parallel detection.<sup>30</sup> Growing interest in coincidence spectroscopy can be observed by related work by Müllejans and coworkers (see, e.g., Müllejans<sup>31</sup> and references therein) and by Scheinfein *et al.*<sup>32</sup> Cazaux<sup>33</sup> recently applied coincidence experiments between Auger and energy-loss electrons in a slightly modified Auger electron spectroscopy (AES) instrument, using a cylindrical mirror analyzer with split detector. Related work is done in Budapest (Hungary) by Gergely,<sup>34</sup> who is working on Auger and core-level ionization loss coincidence spectroscopy in reflection mode, with separate analyzers for the two electrons. Coincidence techniques are used to perform electron momentum spectroscopy by McCarthy and Weigold.<sup>35</sup> This type of spectroscopy differs from the technique discussed here in the sense that spatial resolution is exchanged for angular resolution. Despite the resemblances, the experimental requirements lead to quite different designs.

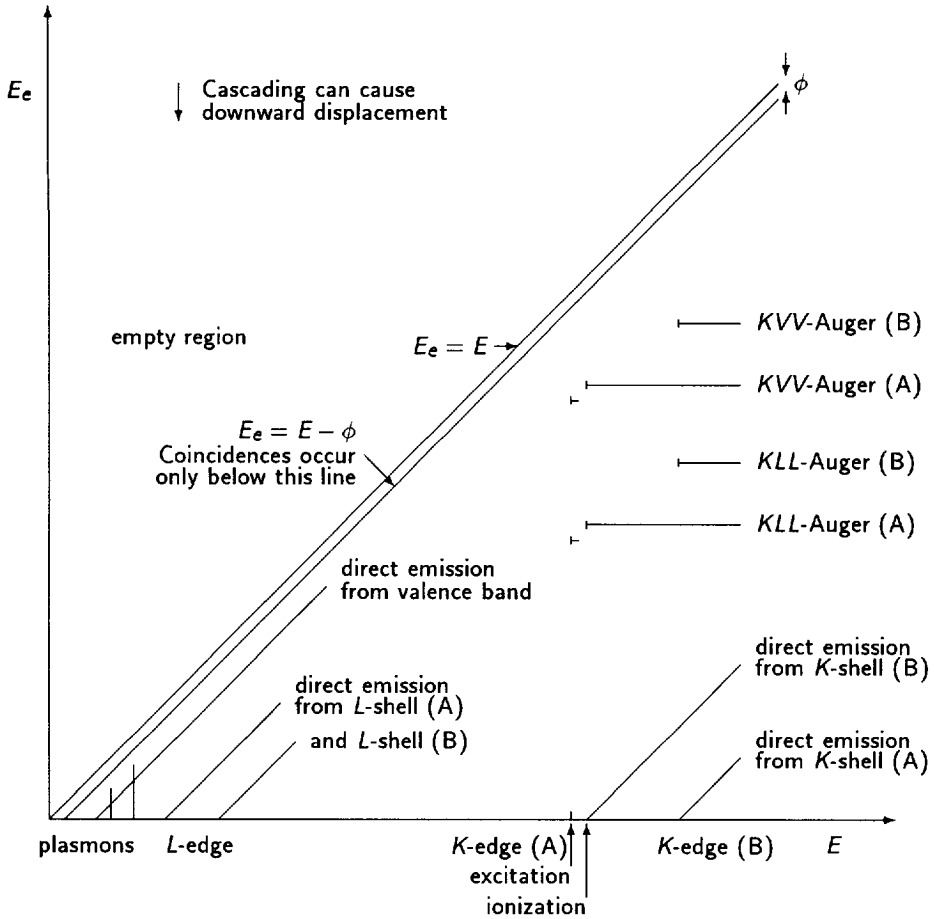


Fig. 1.2: Schematic 2-D secondary-EELS coincidence spectrum, for specimen with two elements, A and B, with B the heavier species. Horizontal scale represents energy transfer (energy loss of transmitted electron), vertical scale represents kinetic energy of emitted electron.

## 1.4. Possible Applications

Coincidence spectroscopy can be applied to a large range of energy losses and kinetic energies of the emitted electron. Figure 1.2 gives a schematic representation of the 2-dimensional spectrum, which is extended across the energy-loss scale and the kinetic-energy scale of the emitted electrons. In principle both horizontal and vertical scale could extend up to the kinetic energy of the incoming electrons.

## 1. Introduction

There is however no reason to go beyond half this value since in practice both electrons cannot be distinguished. The fastest one is called the energy-loss electron. If the incoming electron loses more than half its energy, effectively both electrons exchange roles. In the past ( $e, 2e$ ) experiments have been performed in the region close to half the original kinetic energy,<sup>11,12,14,35-38</sup> mainly for reasons of simultaneous determination of scattering momenta, but here we will concentrate on energy losses and consequently kinetic energies up to a few keV. In the following, some of the features of Fig. 1.2 will be discussed.

### 1.4.1. Virtual-Photo Electron Spectroscopy

The amount of energy put into the electron-impact collision can be regarded as a virtual photon, hence the name *virtual-photo electron spectroscopy*. Because of the possibility to tune the energy loss, it is comparable to photo-electron spectroscopy performed with tunable synchrotron radiation. The energy transfer available (from several eVs to about 2 keV) covers a range that is also covered by different synchrotron radiation sources. Main advantage of the coincidence technique is the high spatial resolution that is given by the size of the electron probe, which is orders of magnitude smaller than obtainable with x-rays.

In the past the coincidence technique has been called “the poor man’s synchrotron”. In the light of the price of synchrotrons this may be valid, but unfortunately coincidence spectroscopy in a STEM cannot be achieved without difficulties or costs either.

The virtual-photo electron spectroscopy technique can be associated with diagonal lines with positive slope in Fig. 1.2. Diagonal lines that start at the inner shell edges signify a constant value of  $E - E_e$ , where  $E$  is the energy loss and  $E_e$  the energy of the emitted electron. These lines therefore represent a constant binding energy level  $E_b$ , see Eq. (2.4). This is the binding energy level of the electron that has been released. The emitted electrons are directly knocked out of the inner shell and have gained a kinetic energy equal to the difference between the minimum required loss for ionization from this inner shell and the actual loss of the incoming electron. If further (cascade) losses have occurred, some of the kinetic energy will be taken away from the emitted electron and a coincidence may appear somewhat below the diagonal line. The emitted electrons on the line are the so-called virtual-photo electrons that appear for ‘virtual photon’ energies of the inner shell binding energy plus a little. The processes discussed in section 2.2 are all features on diagonal lines.

A virtual-photo electron spectrum is obtained by scanning in the direction perpendicular to lines of constant binding energy. An increase in energy loss is accompanied by a decrease in kinetic energy setting, so that the virtual-photon energy  $E + E_e$  is constant. Also possible is an integration (in part of the 2-D spectrum) along lines of constant binding energy, which emphasizes features of constant binding energy and tends to smear out the horizontal features that represent Auger processes. To obtain an equivalent effect in photo electron spectroscopy one

needs to add suitably shifted spectra obtained by using different photon energies.

### 1.4.2. Coincident Auger Spectroscopy

A normal Auger or kinetic-energy spectrum is the vertical spectrum that remains after an integration over all possible energy losses in the 2-dimensional spectrum of Fig. 1.2. A coincident Auger spectrum represents a single vertical line at the horizontal position of the selected energy loss.

#### Background Reduction

Background reduction in Auger spectroscopy could be an important application of coincidence spectroscopy. It is performed by taking a kinetic-energy spectrum while selecting only those secondary/Auger electrons that are accompanied by energy-loss events that are large enough to create an inner-shell hole of interest. In principle only a lower limit has to be imposed on the energy loss, so that all events left of a vertical line through the *K*-edge in Fig. 1.2 are discarded and therefore don't show up in the background below the *KVV* and *KLL* Auger peaks.

Since with more surplus energy above the *K*-edge the cross section for *K*-edge ionization drops again and the chance of selecting other inner shell edges (from different atoms) may start playing a role, it is profitable also to limit the energy-loss region on the high side, thereby selecting only coincidence events from a vertical strip in Fig. 1.2. If this strip contains only one inner-shell edge than a quite clean Auger spectrum is to be expected with the background under the peaks only determined by cascade losses from the peak(s) above it (and of course zero background above the virtual-photo electron peak).

Figure 1.3 shows what is expected when a coincidence Auger spectrum is taken of a material consisting of two elements A and B, with B the heavier element. For Fig. 1.3a the EELS window is set for the *K*-edge of element A, up to some value lower than the *K*-edge of element B. The Auger features of element B cannot appear in this spectrum. Figure 1.3b shows the result when the EELS window is set for the *K*-edge of element B. Of course in the energy-loss spectrum the background under the *K*-edge of element B is partly due to ionizations of the *K*-edge of element A, so that in the coincidence spectrum some residual peaks of element A can occur. The direct (virtual-photo) electron emission peaks at the right end of the coincidence spectra form a continuous background in the regular (non-coincident) spectrum as shown in Fig. 1.3c. The expected improvement of peak to background ratio in coincidence Auger spectra over regular (electron induced) Auger spectra is comparable to the difference between x ray and electron induced Auger and EDX spectra.

#### Toward Single Atom Detection

With a sufficiently reduced background Auger peaks are identified more easily. In principle quantitative information can be deduced, which is an advantage over standard Auger spectroscopy. Since the Auger information comes from a few top

## 1. Introduction

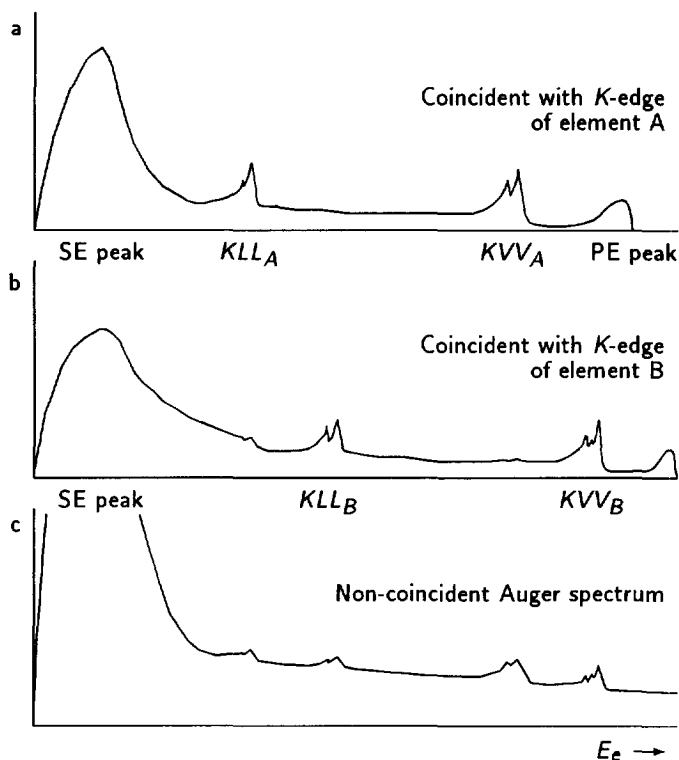


Fig. 1.3: Schematic Auger spectra, (a) in coincidence with  $K$ -edge losses of element A, (b) in coincidence with  $K$ -edge losses of heavier element B and (c) the accompanying non-coincident Auger spectrum.

layers and the lateral dimensions can be as small as the primary electron probe, only a very small volume is excited. A single atom represents a relatively large fraction in such a 'nano-volume' of the analyzed material.

### Identifying Spectator, Participant and 'Ionized' Auger Features

A further selection can be made with a very narrow EELS window set near to the inner-shell edge. The inner-shell electron is then excited to a weakly bound level, where it either 'watches' the Auger emission take place or takes part in the Auger process itself (as the emitted or the 'back-falling' electron). The 'watching' electron performs the role of *spectator*. Due to its presence no complete Coulomb field redistribution takes place, since the amount of electrons inside the atom or molecule has not changed.

If the electron that is excited to the weakly bound level takes part in the Auger process, as a *participant*, even more specific information on the process is



available. The energy loss determines the exact energy difference with respect to the inner-shell level. We will suppose for simplicity that there is only one such inner-shell level and that the excited electron falls back to this inner-shell level, under emission of the Auger electron. The resulting Auger spectrum will then be a quite straightforward mapping of the outer-shell structure, since the amount of energy transferred to the Auger electron is exactly known. In the spectator case, the level from which the one electron falls back is not exactly known (somewhere in the outer shell). Since also the level from which the other electron is emitted is unknown, the kinetic-energy spectrum will be some kind of self-convolution (obeying selection rules) of the outer shell.

After both spectator and participant Auger electron emission the atom or molecule becomes singly charged and these are called auto-ionizing processes. Examples of this selection (in gases) are given by Ungier and Thomas.<sup>10</sup>

If on the other hand the EELS window excludes the near-edge excitation, the atom becomes singly charged in the virtual photo emission step and doubly charged in the Auger process. Due to the absence of one electron just before the Auger emission, a Coulomb field redistribution takes place which shifts the energy levels by some amount. Compared to the non-ionized Auger process this leads to different Auger peak positions, and the ability to split these peaks by coincidence techniques can simplify the interpretation of the spectra.

A similar distinction of Auger peaks is possible when selecting specific inner-shell sub-shells with the EELS detector. For example  $L_1M_xM_y$  and  $L_{2,3}M_xM_y$  peaks can then be distinguished.

### Improving Spatial Resolution in Secondary-Electron Imaging

In high resolution STEM the position dependent secondary-electron signal is used to form an image. Even with ultra fine electron probes (on the order of a few tenths of nanometers) the resolution of the secondary-electron images seems to follow the probe size. Since most secondary electrons have energies of only a few eVs, effects of delocalization were expected to limit the obtainable resolution. Understanding the contrast formation mechanism by means of studying the process of secondary-electron production might give answers to these questions.

Low energy losses can occur at relatively large impact parameters, which means that the resulting decay process can take place from atoms that are not in the area originally hit by primary electrons. Collective excitations (plasmons) form the majority of low loss processes. For example, surface plasmon losses are known (both from theory<sup>39,40</sup> and experiment<sup>41,42</sup>) to limit spatial resolution to the order of 10 nm. Large energy losses on the other hand have smaller impact parameters and thus are better localized. By selecting only those secondary electrons that are accompanied by high-energy loss events a higher degree of localization is to be expected.

Another possibility for improved localization is given by considering secondary electrons which follow large-angle scattering. This could be done by using an off-

## 1. Introduction

axis aperture, or an on-axis 'hollow-cone' aperture, so that large impact-parameter processes (soft collisions) are excluded.

In scanning electron microscopy (SEM) operation, using secondary-electron intensity to form an image, one generally distinguishes secondary electrons from different contributions.<sup>43</sup> Type I, signifies the secondary electrons created by the primary electrons, type II the ones created by back-scattered fast electrons inside the specimen, and type III the ones also released by back-scattered electrons, but from different parts of the specimen surroundings. With the coincidence technique one obviously discards type II and III from the secondary electron spectra, which improves contrast.

### 1.4.3. Coincident Energy-Loss Spectroscopy

A coincident energy-loss spectrum represents a single horizontal line at the vertical position of the selected kinetic energy in the 2-dimensional spectrum (Fig. 1.2). The normal energy-loss spectrum can be seen as the horizontal spectrum that remains after an integration over all possible secondary electron energies in the 2-dimensional spectrum. One should realize however that such integration yields an EELS spectrum which represents the top layers only. Besides this, not all energy-loss processes yield the same amount of coincidence counts in the 2-dimensional spectrum. The excitation of an inner-shell electron to a weakly bound position followed by x-ray emission does not yield a count in coincidence. The same excitation but followed by Auger emission yields a single count. Ionization followed by x-ray emission yields one too. Non-radiative ionization yields both a directly-emitted electron as well as an Auger electron, or two counts. For the moment we will assume there is no instrumental difficulty in detecting more than one electron at a time in the secondary electron detector (in the coincidence set-up). The *fluorescence ratio* or the fraction of processes that leads to x-ray emission is quite low for energies below a few keV, see Fig. 1.4. This means that the shape of the integrated energy spectrum will not be too different from plain energy-loss spectra, apart from the surface sensitivity.

### Surface Sensitivity

Since the escape depth is quite small at almost all kinetic energies of the emitted electrons, coincidence spectroscopy becomes surface sensitive, no matter what energy window is chosen. Of course, if ultimate surface sensitivity is desired, the secondary electrons with the shortest escape depth should be selected for the coincidence. According to Seah and Dench<sup>46</sup> (see Fig. 2.13) in most materials the minimum escape depth is found around 30 or 40 eV and reaches values below 1 nm. By selecting a range of different kinetic energies (with different escape depth) for the coincidence technique, some kind of depth profiling might be considered.

However, one should realize that due to all non-vertical features in Fig. 1.2 even energy-loss spectra of bulk samples will change in shape.

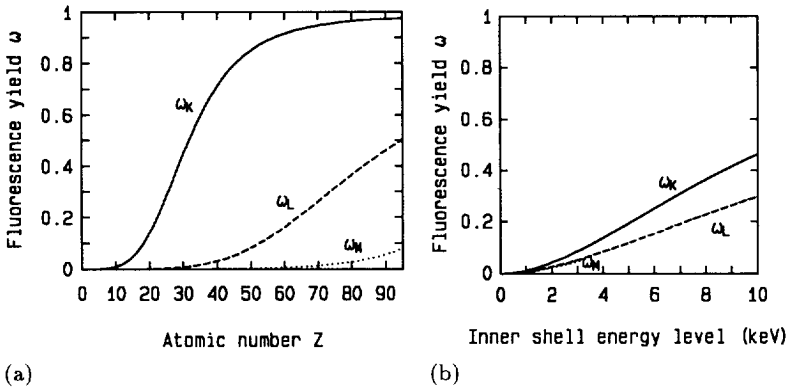


Fig. 1.4: (a) Fluorescence yield  $\omega_K$ ,  $\omega_{L_{III}}$  and  $\omega_{M_{IV}}$  as a function of atomic number  $Z$ , and (b) as a function of inner-shell binding energy (adapted from Bambynek *et al.*<sup>44</sup> and Lorimer<sup>45</sup>).

### Background Reduction

As for Auger spectroscopy there is a possibility to reduce the background under inner-shell edges in the EELS spectrum. Since this background is formed by the possibility to excite weaker bound inner-shell electrons, valence band electrons or collective oscillations (of the same or of different elements), they will not coincide with Auger electrons that have been emitted as a result of the inner-shell excitation under study. The relative large backgrounds in EELS are expected to be suppressed drastically by the coincidence technique. If small signals can be distinguished more easily, again an improvement in detection limits is to be expected. Completely parallel to the coincident Auger spectroscopy technique, analyzing nanovolumes for trace elements is not unthinkable. At the end of Chapter 3 computations are made, which show the improvement in signal-to-noise ratio and the conditions under which single atoms can be identified.

Taking a (horizontal) energy-loss spectrum in coincidence with a kinetic-energy window, set to accept one or more appropriate Auger peaks, is therefore expected to give a good background reduction. The reduction in signal can be computed from the fluorescence ratio and the relative intensities of the Auger peaks.

For higher-energy losses, where x-ray emission becomes more prominent, the effect of background reduction was shown experimentally by Kruit and Shuman.<sup>25</sup> In their experiment, the regular energy-loss spectrum of the Ca  $K$ -edge showed only a  $\approx 10\%$  increase with respect to the background. An energy-loss spectrum collected in coincidence with Ca  $K_\alpha$  and  $K_\beta$  x-rays showed an almost complete removal of background under the Ca  $K$ -edge.

Figure 1.5 shows what is expected for a coincidence energy-loss spectrum of a material consisting of two elements A and B, with B the heavier element. For

1. Introduction

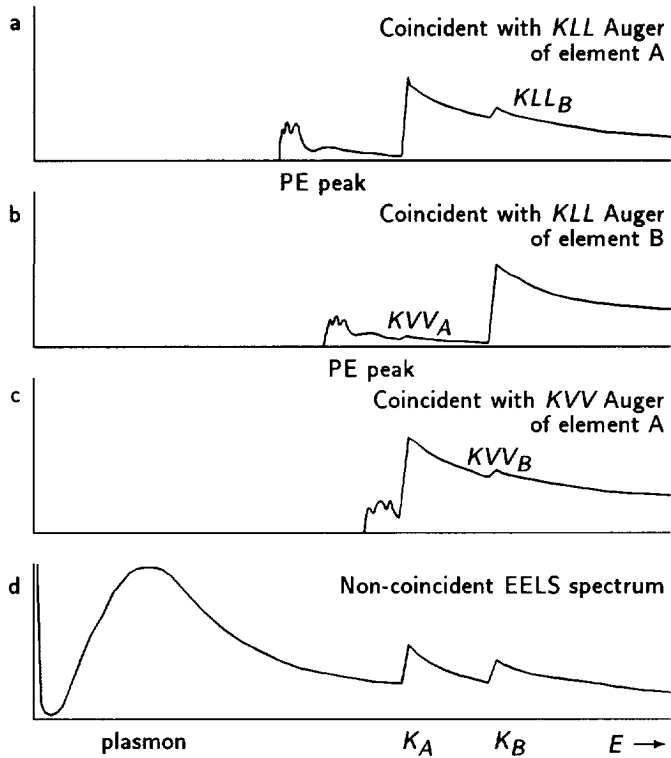


Fig. 1.5: Schematic energy loss spectra, (a) in coincidence with the  $KLL$  Auger peak of element A, (b) in coincidence with the  $KLL$  Auger peak of heavier element B, (c) in coincidence with the  $KVV$  Auger peak of element A and (d) the accompanying non-coincident energy-loss spectrum.

Fig. 1.5a the kinetic energy window is set on the  $KLL$  Auger feature of element A. A small remainder of the  $K$ -edge of element B results from the  $KLL$  Auger electrons of that element that have lost some energy while escaping. Figure 1.5b shows the result when the kinetic energy window is set on the  $KLL$  Auger peak of element B. Here again some remainder of the  $K$ -edge of element A is seen due to the cascade losses on the  $KVV$  Auger electrons of this element. Figure 1.5c shows a similar result when the kinetic energy window is set on the  $KVV$  Auger peak of element A. Here again some remainder of the  $K$ -edge of element B is seen due to the cascade losses on the  $KVV$  Auger electrons of this element. The main difference with Fig. 1.5a is the fact that the direct emission or photo electron peak appears much closer to the  $K$ -edge so that the background looks much higher. The direct emission peaks at the left end of the coincidence spectra form a continuous background in the regular (non-coincident) spectrum as shown in Fig. 1.5d. At

low energies plasmon losses are dominant.

#### 1.4.4. Absolute Detection Efficiencies

An important question in quantitative analysis is the requirement of absolute cross section data. With certain experimental limitations coincidence methods can provide absolute cross sections for some selected processes. If for example, the emission of a certain Auger electron is registered, it is known to have been preceded by a specific inner-shell loss. The amount of inner-shell loss electrons, in coincidence with the Auger electrons, compared to the total amount of Auger electrons measures the detection efficiency of the specific inner-shell loss measurement.

In a similar way, with known fluorescence ratio, the detection efficiency of the Auger electron measurement can be determined from the ratio of coincidence counts and the total inner-shell loss counts. If acceptance angles and detection efficiencies are known, absolute cross section data can be constructed.

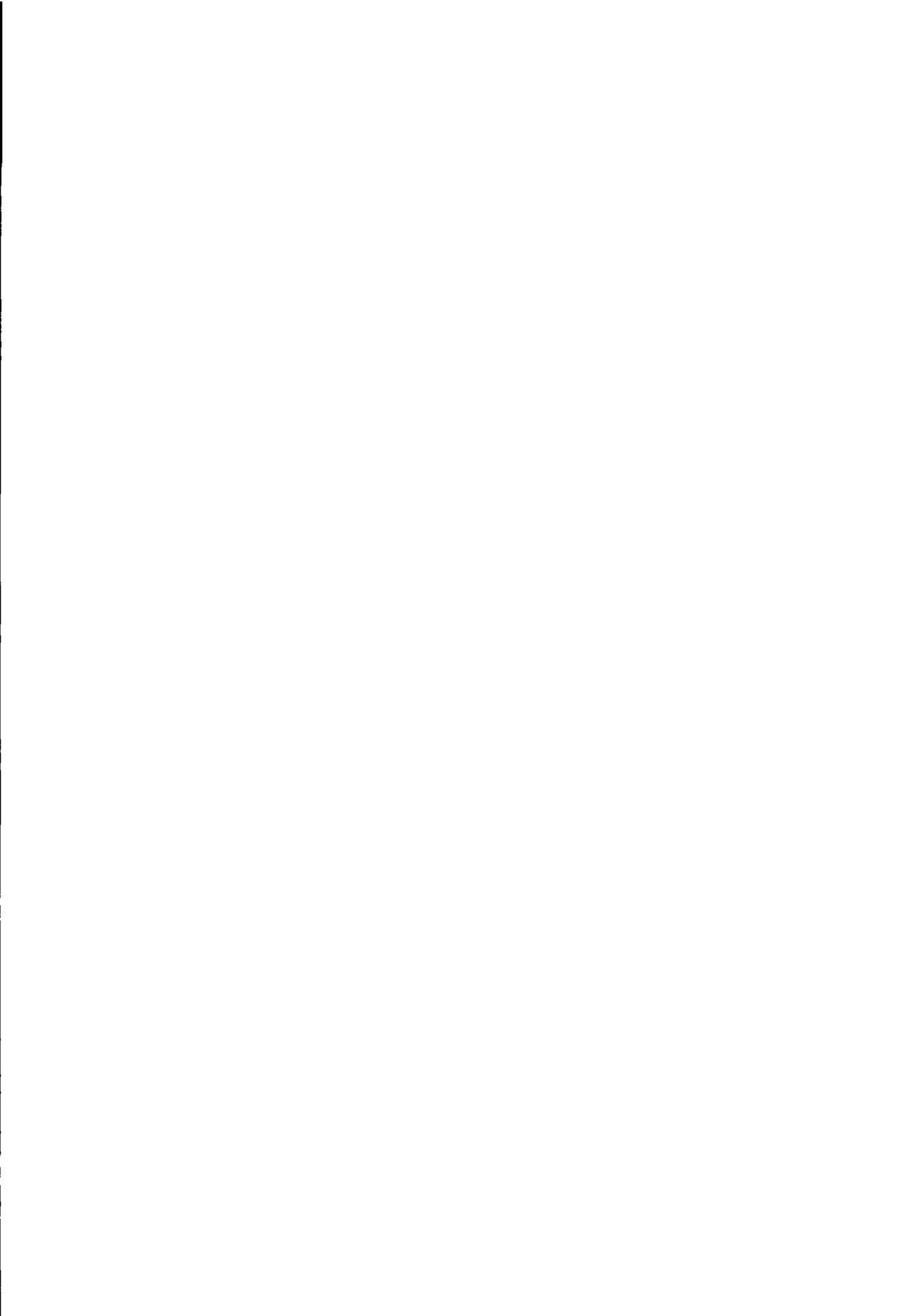
### 1.5. References

- <sup>1</sup> A. J. Bleeker. *Optical and mechanical design for 1 nm resolution Auger spectroscopy in an Electron Microscope*. PhD thesis, Delft University of Technology, June 1991.
- <sup>2</sup> O. Chamberlain and E. Segré, *Proton-proton collisions within lithium nuclei*, Phys. Rev. **87**, 81 (1952).
- <sup>3</sup> H. Ehrhardt, M. Schulz, T. Tekaas and K. Willmann, *Ionization of helium: Angular correlations of the scattered and ejected electrons*, Phys. Rev. Letters **22**, 89 (1969).
- <sup>4</sup> M. J. van der Wiel, *Small-angle scattering of 10 keV electrons in He, Ne, and Ar*, Physica **49**, 411 (1970).
- <sup>5</sup> M. J. van der Wiel and C. E. Brion, *Energy dependence of the photoelectron angular distribution parameter for Ne 2p electrons, measured in an electron-electron coincidence experiment*, J. Electron Spectrosc. Relat. Phenom. **1**, 439 (1972/73).
- <sup>6</sup> M. J. van der Wiel, Th. M. El-Sherbini and C. E. Brion, *K-shell excitation of nitrogen and carbon monoxide by electron impact*, Chem. Phys. Lett. **7**, 161 (1970).
- <sup>7</sup> H. W. Haak, G. A. Sawatzky, L. Ungier, J. K. Gimzewski and T. D. Thomas, *Core-level electron-electron coincidence spectroscopy*, Rev. Sci. Instrum. **55**, 696 (1984).
- <sup>8</sup> P. H. Citrin, R. W. Shaw, Jr. and T. D. Thomas. *Cylindrical electrostatic analyzer for photoelectron spectroscopy*. In *Electron Spectroscopy*, D. A. Shirley (Ed.), p. 105. North-Holland, Amsterdam, 1972.
- <sup>9</sup> L. Ungier and T. D. Thomas, *Resonance-enhanced shakeup in near-threshold core excitation of CO and N<sub>2</sub>*, Phys. Rev. Lett. **53**, 435 (1984).
- <sup>10</sup> L. Ungier and T. D. Thomas, *Near threshold excitation of KVV Auger spectra in carbon monoxide using electron-electron coincidence spectroscopy*, J. Chem. Phys. **82**, 3146 (1985).
- <sup>11</sup> U. Amaldi, Jr., A. Egidi, R. Marconero and G. Pizzella, *Use of a two channeltron coincidence in a new line of research in atomic physics*, Rev. Sci. Instrum. **40**, 1001 (1969).

## 1. Introduction

- <sup>12</sup> R. Camilloni, A. Giardini Guidoni, R. Tiribelli and G. Stefani, *Coincidence measurements of quasifree scattering of 9-keV electrons on K and L shells of carbon*, Phys. Rev. Lett. **29**, 618 (1972).
- <sup>13</sup> N. A. Krasil'nikova, V. G. Levin and N. M. Persiantseva, *Measurements of the momentum distributions of K electrons of light atoms*, Sov. Phys.-JETP **42**, 796 (1976).
- <sup>14</sup> N. A. Krasil'nikova and N. M. Persiantseva, *Measurements of the angular correlation functions in the (e, 2e) reaction on aluminum films*, Phys. Lett. **69A**, 287 (1978).
- <sup>15</sup> N. M. Persiantseva, N. A. Krasil'nikova and V. G. Neudachin, *Investigation of the collective properties of a degenerate electron gas in aluminum by the (e, 2e) method*, Sov. Phys.-JETP **49**, 530 (1979).
- <sup>16</sup> A. L. Ritter, J. R. Dennison and R. Jones, *Spectral momentum density of amorphous carbon from (e, 2e) spectroscopy*, Phys. Rev. Lett. **53**, 2054 (1984).
- <sup>17</sup> H. W. Haak, G. A. Sawatzky and T. D. Thomas, *Auger-photoelectron coincidence measurements in copper*, Phys. Rev. Lett. **41**, 1825 (1978).
- <sup>18</sup> H. W. Haak, *Auger-Photoelectron Coincidence Spectroscopy: a study of correlation effects in solids*. PhD thesis, University of Groningen, Netherlands, February 1983.
- <sup>19</sup> J. Kirschner, O. M. Artamonov and A. N. Terekhov, *Two-electron coincidence spectroscopy of scattering events at surfaces*, Phys. Rev. Lett. **69**, 1711 (1992).
- <sup>20</sup> D. Voreades, *Secondary electron emission from thin carbon films*, Surf. Sci. **60**, 325 (1976).
- <sup>21</sup> N. B. Gornyi, *Plasmon photoelectric and secondary electron emission*, Fiz. Tverd. Tela **8**, 1939 (1966), [*Sov. Phys. Solid State* **8**, 1535 (1966)].
- <sup>22</sup> N. B. Gornyi, L. M. Rakhovich and S. F. Skirko, *Plasma losses of electron energy and secondary electrons of discrete energies in aluminum*, Soviet Phys. J. **10**, 15 (1967).
- <sup>23</sup> R. F. Willis, B. Fitton and G. S. Painter, *Secondary-electron emission spectroscopy and the observation of high-energy excited states in graphite: Theory and experiment*, Phys. Rev. B **9**, 1926 (1974).
- <sup>24</sup> F. J. Pijper and P. Kruit, *Detection of energy-selected secondary electrons in coincidence with energy-loss events in thin carbon foils*, Phys. Rev. B **44**, 9192 (1991).
- <sup>25</sup> P. Kruit, H. Shuman and A. P. Somlyo, *Detection of x-rays and electron energy loss events in time coincidence*, Ultramicroscopy **13**, 205 (1984).
- <sup>26</sup> A. W. Nicholls, I. P. Jones and M. H. Loretto, *Coincidence counting techniques in analytical electron microscopy*, in *Institute of Physics Conference Series No. 78: Chapter 7, Paper presented at EMAG '85, Newcastle upon Tyne*, p. 205, Bristol, England, September 1985. IOP, Adam Hilger Ltd.
- <sup>27</sup> D. B. Wittry, *Spectroscopy in microscopy and microanalysis: The search for an ultimate analytical technique*, Proc. 7th European Congress on Electron Microscopy 1980 **3**, 14 (1980).
- <sup>28</sup> D. B. Wittry, *Use of coincidence techniques to improve the detection limits of electron spectroscopy in STEM*, Ultramicroscopy **1**, 297 (1976).
- <sup>29</sup> J. Cazaux, *Detection limits in Auger electron spectroscopy*, Surf. Sci. **140**, 85 (1984).
- <sup>30</sup> P. Kruit, W. Th. Wenckebach and C. W. E. van Eijk, *(Coincidence) electron spectroscopy with nanometer scale resolution*, unpublished project proposal, 1991.
- <sup>31</sup> H. Müllejjans, *Secondary Electron Emission in Coincidence with Primary Energy Losses*. PhD dissertation, University of Cambridge, Churchill College, 1992.
- <sup>32</sup> M. R. Scheinfein, J. Drucker and J. K. Weiss, *Secondary-electron production pathways determined by coincidence electron spectroscopy*, Phys. Rev. B **47**, 4068 (1993).

- <sup>33</sup> J. Cazaux, O. Jbara and K. H. Kim, *Some unconventional experiments cross correlating the techniques in surface analysis*, Surf. Sci. **247**, 360 (1991).
- <sup>34</sup> G. Gergely, *Proposal for a possible experimental arrangement of Auger- and core level ionization loss coincidence spectroscopy in reflection mode*, Acta Physica Hungarica **70**, 47 (1991).
- <sup>35</sup> I. E. McCarthy and E. Weigold, *Electron momentum spectroscopy of atoms and molecules*, Rep. Prog. Phys. **54**, 789 (1991).
- <sup>36</sup> Chao Gao, A. L. Ritter, J. R. Dennison and N. A. W. Holzwarth, *Spectral momentum density of graphite from (e, 2e) spectroscopy: Comparison with first-principles calculation*, Phys. Rev. B **37**, 3914 (1988).
- <sup>37</sup> P. Hayes, M. A. Bennett, J. Flexmann and J. F. Williams, *Symmetric transmission electron momentum (e, 2e) spectroscopy of an aluminum-aluminum oxide thin foil*, Phys. Rev. B **38**, 13371 (1988).
- <sup>38</sup> P. Hayes, J. F. Williams and J. Flexmann, *Transmission (e, 2e) coincidence measurements of thin evaporated carbon, graphite, and aluminum-aluminum oxide thin foils*, Phys. Rev. B **43**, 1928 (1991).
- <sup>39</sup> H. Kohl, *Image formation by inelastically scattered electrons: Image of a surface plasmon*, Ultramicroscopy **11**, 53 (1983).
- <sup>40</sup> H. Kohl and H. Rose, *Theory of image formation by inelastically scattered electrons in the electron microscope*, Adv. in Electronics and Electron Physics **65**, 173 (1985).
- <sup>41</sup> P. E. Batson and M. M. J. Treacy, *Low energy-loss structure of small aluminum particles*, in *Ann. Proc. Electron Microsc. Soc. Am.*, Baton Rouge, Louisiana, 1980, edited by G. W. Bailey, p. 126, EMSA. (Claitor's Publishing, 1980).
- <sup>42</sup> M. Achèche, C. Colliex and P. Trebbia, *Characterization of small metallic clusters by electron energy loss spectroscopy*, Scanning Electron Microscopy **1**, 25 (1986).
- <sup>43</sup> L. Reimer, *Scanning Electron Microscopy, Physics of Image Formation and Microanalysis*, Vol. 45 of *Springer Series in Optical Sciences*. (Springer-Verlag, 1985).
- <sup>44</sup> W. Bambynek, B. Crasemann, R. W. Fink, H.-U. Freund, H. Mark, C. D. Swift, R. E. Price and P. Venugopala Rao, *X-ray fluorescence yields, Auger, and Coster-Kronig transition probabilities*, Rev. Mod. Phys. **44**, 716 (1972).
- <sup>45</sup> G. W. Lorimer, *Quantitative x-ray microanalysis of thin specimens*, in *Quantitative electron microscopy, Proc. 25th Scottish Univ. Summer School in Physics*, edited by J. N. Chapman and A. J. Craven, p. 305, Scottish Univ. Summer School in Physics. (SUSSP Publications, Edinburgh, 1984).
- <sup>46</sup> M. P. Seah and W. A. Dench, *Quantitative electron spectroscopy of surfaces: A standard data base for electron inelastic mean free paths in solids*, Surf. Interface Anal. **1**, 2 (1979).





## 2. Physics of Coincidence Spectroscopy

Electron impact phenomena on solids have been studied with several analytical techniques. They can be important for obtaining physical as well as chemical information from the material under study. A theoretical description of the simultaneous detection of an energy-loss electron and an emitted electron is based on a combination of EELS and secondary electron emission theory. EELS theory describes what happens with the fast primary electron and the direct excitation event, but is not particularly concerned with the subsequent decay or scattering processes that define a possible electron emission process. Secondary electron emission theory describes what happens after the original excitation event in terms of electron transport and escape possibilities, but it is not very specific about the exact amount of energy that is lost by the primary electron.

Building on both theories, the detection of energy-selected secondary electrons in coincidence with energy-selected energy-loss events can be described in terms of the scattering cross sections, the decay channels, the electron transport problem and the escape probabilities. Instrumental aspects like the quality of the electron optics and the efficiency of detection will be discussed in Chapter 3.

Coincidence spectroscopy is interesting from the physical point of view, in the sense that it provides a way of unraveling spectral features, relating them more directly to some specific interactions. The technique can bring enhanced surface sensitivity to some spectroscopic fields. The close resemblance of one of the applications, namely virtual-photo electron spectroscopy, with XPS based on synchrotron radiation sources justifies a comparison between these techniques.

In this chapter, a short description of processes that can occur on electron impact will be given first. Then a scattering event which yields an energy-loss electron as well as a knock-out electron will be discussed, both in terms of energy and momentum. This results in angular emission probability functions of emitted electrons that are coincident with energy selected loss events. A slight preference for forward emission is shown. Following that, the effects of subsequent scatterings of the emitted electron on its way to the surface are shortly discussed. A comparison with photo absorption shows how well the coincidence technique compares with some state of the art synchrotron radiation sources.

## 2.1. Possible Processes at Electron Impact

The impact of a fast electron on a solid can supply energy to excite the system to higher energy levels. A distinction is made between (quasi-) elastic and inelastic scattering events. (Quasi-) *elastic scattering* of a fast electron by the electrostatic field of atomic nuclei involves only small energy transfer ( $\lesssim 20$  eV, in head-on collisions) due to the large mass difference. Elastic scattering gives rise to diffraction effects and is sensitive to atomic vibrations (phonons), which are strongly temperature dependent. With a standard energy-loss spectrometer quasi-elastic losses cannot be resolved. This kind of scattering will therefore not be considered here.

*Inelastic scattering* involves interaction of the fast electron with the inner- and outer-shell electrons. Kinetic energy is not conserved in inelastic scattering; momentum is, however, a conserved quantity. Because of equal mass of incoming and target electron significant energy transfer occurs. Inelastic scattering can involve a single electron or a collective response of many electrons.

### 2.1.1. Single-Electron Interaction

The *excitation* of a deeply bound electron state (an *inner shell*) to a less bound unoccupied state or the *ionization* to a completely free state, leaves the atom, molecule or singly-charged ion in an excited state. In the *deexcitation* process the vacant electron position or hole will be filled by electrons from the less bound states. This can happen either under emission of an x-ray photon with an energy equal to the difference in energy of the two levels (Fig. 2.1a), or by emission of an *Auger electron* (Fig. 2.1b and c). The kinetic energy of the Auger electron is approximately equal to  $E_{b_1} - E_{b_2} - E_{b_3}$ , where  $E_b$  are the binding energy levels (measured from the vacuum level  $E_{\text{vac}}$ ) of the hole and the two other participating electrons (the electron that fills the hole and the Auger electron). A more accurate approach needs to take into account the Coulomb field redistribution that occurs after the first (virtual-photo) electron has been emitted.

Alternatively, the fast electron can excite an *outer-shell* electron and this leaves a hole which can be filled by electrons from still higher energy levels under emission of visible light, called *cathodoluminescence* (Fig. 2.1d).

The deexcitation generally follows the excitation on a very short timescale. For example electronic autoionization, the process in which a neutral excited state undergoes a transition to an ion and a kinetic electron, occurs on a timescale of  $10^{-15}$ – $10^{-11}$  seconds.<sup>1</sup> In practice the directly-emitted electron from an ionization process is followed ‘immediately’ by an Auger electron, and both electrons cannot be distinguished in the time domain. Radiative transition from the same state is somewhat slower ( $10^{-9}$ – $10^{-7}$  seconds), but such processes are not included in electron-electron coincidence experiments.

Throughout the rest of this chapter we will concentrate on the directly-emitted and the recoil electron. The treatment of Auger electrons in an electron coincidence technique shows close resemblances. However, Auger spectra generally show sharp lines, which means that Auger electrons have a well-defined energy. The

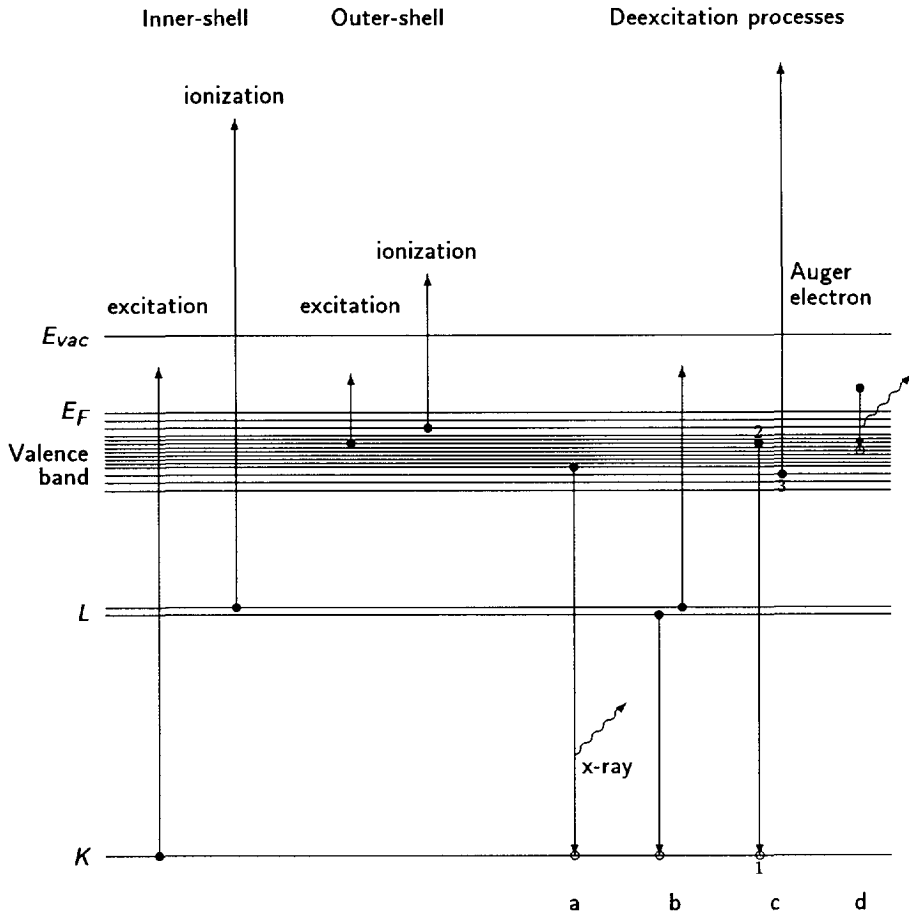


Fig. 2.1: Band-level diagram of electron impact processes, showing inner-shell excitation and ionization, outer-shell excitation and ionization and several deexcitation processes: (a) x-ray emission, Auger emission leading to (b) a singly- or (c) a doubly-charged ion and (d) cathodoluminescence. Non-participating electrons are not shown.

excited state from which the Auger emission originates is well-defined, and this can be interpreted as a diminished influence of the passing fast electron or of the directly-emitted electron. The Auger emission process can therefore be seen as an independent process, which shows no directional preferences. If we consider the emission from the surface rather than from single atoms, escape processes have to be considered, in exactly the same way as for the directly-emitted electron.

## 2. Physics of Coincidence Spectroscopy

### 2.1.2. Collective Interaction

Besides excitation of single particles, scattering processes occur in which a collective response of the electrons takes place. The fast electron starts an oscillation of valence-electron density, usually known as a (bulk) *plasmon*, which forms a longitudinal traveling wave. The plasmon can be seen as a pseudo-particle with an energy  $E_p$  which lies in the range of 5–30 eV.  $E_p$  is given by

$$E_p = \hbar\omega_p, \quad (2.1)$$

where  $\omega_p$  is the angular frequency of the plasma oscillation, in the quasifree electron or jellium approximation given by

$$\omega_p = \sqrt{\frac{ne^2}{\epsilon_0 m}}, \quad (2.2)$$

with  $n$  the number of free electrons per unit volume,  $e$  the electron charge,  $\epsilon_0$  the permittivity in vacuum and  $m$  the (effective) electron mass.

Plasmon oscillations can be heavily damped (depending on the band structure of the material) and consequently have short lifetimes. If a plasmon has sufficient momentum it may decay into electron-hole pairs via interband transitions.<sup>2-4</sup> Depending on material properties this can lead to emission of an electron.

On the surface of the specimen, and at interfaces, oscillation frequencies differ from those in the bulk. Surface plasmons, longitudinal waves of charge density which travel along the solid/vacuum interface, involve a lower excitation energy. For an ideal metal/vacuum interface, surface plasmons are excited at an energy  $E_s = E_p/\sqrt{2}$ . Surface plasmon excitation becomes relatively important in a thin specimen. If surface plasmons decay in a similar way as bulk plasmons,<sup>3</sup> their energy will be transferred to electrons at the solid/vacuum interface, from which escape is relatively easy. It can therefore be expected that surface plasmons are more pronounced in the coincidence spectrum.

### 2.1.3. Delocalization

The ultimate resolution in emitted-electron spectroscopy is not only determined by the probe size of the incident electron beam, but also by the degree of (de)localization of the emission processes. For (de)localization the electrons can be treated either as particles or as waves.

When the electron is treated as a particle, an impact parameter  $b$  can be defined, which determines the distance from the emission process to the trajectory of the fast electron. The impact parameter can only be determined with a precision which is limited by Heisenberg's uncertainty principle  $\Delta p_b \Delta b \geq \hbar/2$ , where  $p_b$  is the momentum along the direction of  $b$ .

The precision with which  $p_b$  can be determined is given by  $p_f \Theta$ , where  $p_f$  is the momentum of the fast electron after the scattering event. The value of  $\Theta$  is either

given by the angular distribution of the scattering processes, or by an aperture which can put an upper limit to this distribution. As an approximation one can use a characteristic or most probable angle  $\theta_E$  (discussed in section 2.2) as measure for the angular distribution. This gives  $\Delta b \geq \lambda/4\pi\theta_E \approx 54 \text{ nm}/E$  (for 100-keV electrons), where  $E$  is the energy loss (in eV) and  $\lambda$  the fast-electron wavelength.

For high energy losses it is more appropriate to look at delocalization in terms of diffraction at the collection-angle defining aperture, using the electron wave character. Diffraction causes the scattering region to appear like an Airy disk of width  $0.6\lambda/\Theta$ . This width is again a direct measure for the delocalization.

A more complete description of the delocalization effect, valid over a large range of energy losses, was given by Kohl and Rose.<sup>5</sup> They have computed radial intensity distributions for several values of energy loss and illumination and collection (half) angles (respectively denoted by  $\alpha$  and  $\Theta$ ). Especially at low losses the simple approximations described above seem to overestimate the delocalization. From their computations it follows that at an illumination angle of 8.8 mrad (see 3.1) and a collection angle of 50 mrad (see 3.2), at 100-keV primary-electron energy, the FWHM values of the radial intensity distribution stay very close to the (probe-forming) diffraction limit of  $0.6\lambda/\alpha \approx 0.25 \text{ nm}$ , for 30–3000-eV energy loss. The expected degradation of the localization at low energy losses does not appear in the FWHM value, but rather in an extension of the tail of the radial distribution. The tail contribution forms a low resolution background, whereas the central peak can still give high spatial-resolution information.

## 2.2. Single-Electron Scattering

We will consider an inelastic scattering process in which a fast electron knocks out an atomic electron, which escapes without scattering. Both the ongoing fast electron and the emitted electron are detected in a coincidence experiment. The amount of energy lost by the fast electron is depending strongly on the scattering angle. The relation between scattering angle and energy loss has been studied in EELS theory for the determination of probabilities for scattering toward the EELS detector. The actual scattering angle is not measured explicitly in standard EELS, but since only scattering inside a given solid angle will contribute, it must be taken into account.

The complete process can be described in terms of initial and final energy and momentum of the fast electron ( $E_i, \hbar\mathbf{k}_i$  and  $E_f, \hbar\mathbf{k}_f$ ), the energy and momentum of the emitted electron ( $E_e, \hbar\mathbf{k}_e$ ), the (binding) energy and momentum of the target electron ( $E_b, \hbar\mathbf{q}_0$ ) and the workfunction  $\phi$ . The opposite of the target electron momentum ( $-\hbar\mathbf{q}_0$ ) can alternatively be regarded as the recoil momentum of the residual system.

First a treatment of the scattering is given in terms of energy, disregarding momentum. Following that, the effect of momenta on coincidence spectroscopy will be discussed.

## 2. Physics of Coincidence Spectroscopy

### 2.2.1. Energy Conservation

A consideration of the band structure of solids is required for the understanding of coincidence spectra. Schematic energy levels and bands that one encounters in a non-metallic solid are shown in Fig. 2.2. Here  $E_{vac}$  represents the vacuum level,  $E_F$

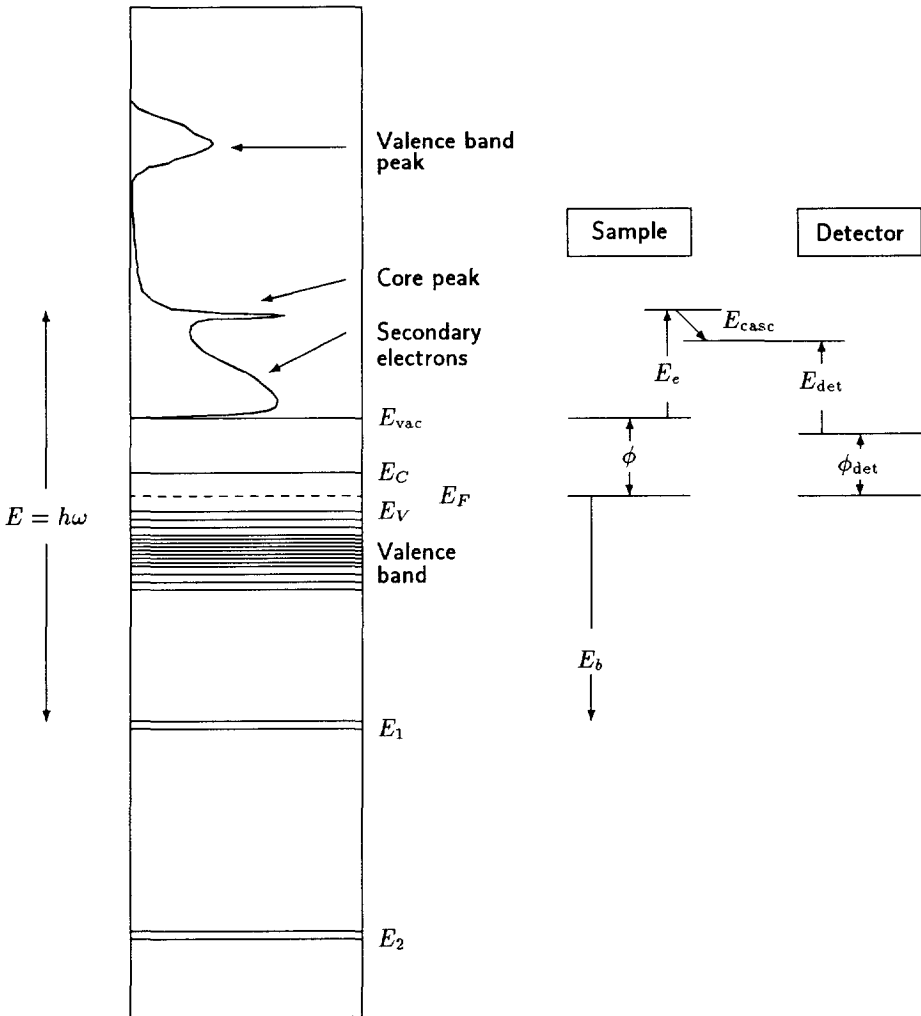


Fig. 2.2: Schematic band structure of a solid with expected emission spectrum.

the Fermi level,  $E_C$  the bottom edge of the conduction band,  $E_V$  the top edge of the valence band and  $E_1$  and  $E_2$  a set of core levels. In order that an electron may escape from the solid, it is essential that the energy lost by the primary electron is at least equal to the difference between the energy of the target-electron state

and  $E_{\text{vac}}$ . In a metal, the minimum energy necessary for ionization of the most loosely bound electron is the difference between  $E_{\text{vac}}$  and the energy of the Fermi level  $E_F$ . This is the work function  $\phi$ . In a non-metal the Fermi level lies in a band gap and an extra energy of  $E_F - E_V$  is required for ionization. When electrons are leaving a non conducting material the sample acquires a positive charge and therefore decelerates the electrons, thereby shifting the complete spectrum by an amount  $\phi_{\text{ch}}$ , equal to the amount of sample charging. This problem is known from photo electron spectroscopy and is only mentioned for completeness.

With EELS one determines the energy loss  $E$  given by:

$$E = E_i - E_f = E_b + E_e + \phi, \quad (2.3)$$

without discrimination on momenta. The binding energy  $E_b$  of the target is measured from the Fermi level. Often  $\phi$  can be regarded as constant over a given part of the specimen, but unfortunately in EELS  $E_e$  is unknown. Features which represent a given value of  $E_b$  therefore appear as edges rather than as peaks in the EELS spectrum, see e.g., Fig. 2.3.

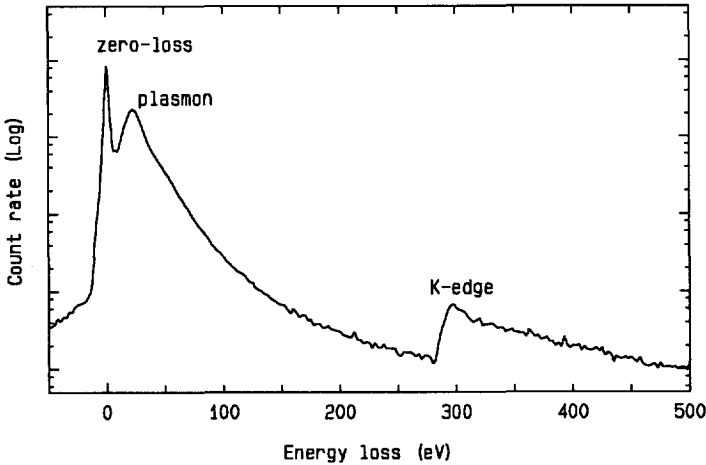


Fig. 2.3: Example EELS spectrum of thin carbon foil showing zero-loss peak, plasmon peak and K-edge.

In coincidence measurements a major improvement can be made by the measurement of  $E_e$ , which enables the estimation of the binding energy from:

$$E_b = E - E_e - \phi. \quad (2.4)$$

This works especially well for gases, where subsequent losses for the emitted electrons do not occur. In practice the original kinetic energy  $E_e$  of the emitted electron is measured in a detector as  $E_{\text{det}} = E_e - (\phi_{\text{det}} - \phi)$ , in which the second term is a

## 2. Physics of Coincidence Spectroscopy

(constant) correction for differences in work function between sample and detector. Sharp peaks in EELS-Auger coincidence spectra by Ungier and Thomas<sup>6</sup> are remarkable examples of this principle.

A small but important drawback which should be noted is that the emission spectrum does not perfectly match the density of initial states, since the emission is only possible to unoccupied final (bulk and surface) state energy levels. Energy gaps in the region close to the vacuum level can therefore disable the emission to these levels, so that the emission spectrum does not reflect the density of initial states. Near the vacuum level bandgaps can be numerous, but with increasing final state energy a continuum of final states becomes available, so that a true reflection of initial states turns out to be possible.

Inside a solid, the electron that is released by the fast electron, will have difficulties escaping into the vacuum. Depending on the depth of the original scattering process and the initial scattering direction, subsequent scattering processes can occur, each with possible energy losses. The total process, starting directly after the generation and up to the escape to the vacuum, is normally associated with a so-called *cascade process*; see, e.g., Wolff.<sup>7</sup> The energy losses  $E_{\text{casc}}$  which occur in the cascade are mainly due to scattering with valence electrons and/or plasmons.

The emitted electrons that are elastically scattered with lattice vibrations or phonons will suffer negligible (meV) changes in energy, but their directions will change. In electron-electron scattering the emitted electron excites target electrons to create electron-hole pairs. For example in a non-metal the minimum energy involved in the electron-hole pair creation will be equal to the band gap  $E_C - E_V$ .

Valence electrons can also be excited in collective oscillations, volume and surface plasmons, with energy  $E_p$  and  $E_s$ . This effect also occurs for the fast primary electrons and gives the most prominent feature in the low energy part of the EELS spectrum, see Fig. 2.3. Emitted electrons which have enough energy to excite plasmons will, apart from creating electron-hole pairs, lose amounts of energy equal to  $E_p$  or  $E_s$ . By repeatedly losing energy the emitted electrons may finally escape from the surface as low-energy electrons, and it is these so-called *secondary electrons* that constitute the background in the emission spectrum.

If the emitted electron loses energy by scattering on its way to the surface, the emitted electron energy  $E_e$  (as it is used in Eq. (2.4)) should be replaced by  $E_{\text{det}} + E_{\text{casc}} + (\phi_{\text{det}} - \phi)$ , the sum of the measured kinetic energy in the detector and the cascade loss energy, with again the correction for workfunction differences. This shows that this coincidence technique will be limited by the uncertain cascade losses, where this uncertainty is of a completely different character than in normal EELS. Of course the coincidence technique will only be an improvement over regular EELS with respect to determining  $E_b$ , if the uncertainty in the cascade losses is less than the uncertainty given by all possible final states for the emitted electron. It is well known that this is the case, since what is done by the elimination of the uncertain value of  $E_e$  is in fact the same as is done in photo electron spectroscopy, where monochromatic photons are used for the excitation. The energy loss of the



fast electron now represents the photon energy:

$$E = \hbar\omega. \quad (2.5)$$

The expected quality of coincidence electron emission spectra, or the amount of ‘smearing’ of the spectra due to  $E_{\text{casc}}$ , is therefore strongly comparable to photoelectron spectra. This means for example that the surface sensitivity of the coincidence technique seems equal to that in photoelectron spectroscopy, although we have not yet included differences in depth-dependent creation and directional effects, the latter due to differences in momentum transfer. In the following section, where momentum effects will be included, it will be shown that apart from sharing some features, coincidence emission spectroscopy also shows differences with photoelectron spectroscopy.

### 2.2.2. Momentum Conservation

The same scattering event can be described in terms of momentum. Conservation of momentum requires that the sum of the initial momentum of the primary electron and the original momentum of the target electron is equal to the sum of the final momentum of the energy-loss electron and the momentum of the emitted electron, or

$$\hbar\mathbf{k}_i + \hbar\mathbf{q}_0 = \hbar\mathbf{k}_f + \hbar\mathbf{k}_e. \quad (2.6)$$

The momentum transferred by the fast electron to the solid  $\hbar\mathbf{q} = \hbar\mathbf{k}_i - \hbar\mathbf{k}_f$ , is a measure for the impact of the collision. For free target electrons the endpoint of vector  $\mathbf{q}_0$  should lie within the Fermi volume and since (almost) all states within this volume are filled, the endpoint of vector  $\mathbf{k}_e$  should lie outside this volume. Above that, in a single crystal the periodicity of the lattice can supply (or absorb) a momentum  $\hbar\mathbf{g}$ , where  $\mathbf{g}$  is a reciprocal lattice vector; see, e.g., Kittel.<sup>8</sup> Because of phonon absorption in *nondirect* transitions  $\mathbf{q}_0$  effectively changes, so that Eq. (2.6) only holds for *direct* transitions. Especially in a solid these conditions therefore form a complicated set of boundary conditions to this momentum transfer problem.

A subfield of physics<sup>9</sup> is devoted to the reconstruction of  $\mathbf{q}_0$  from

$$\hbar\mathbf{q}_0 = \hbar\mathbf{k}_f - \hbar\mathbf{k}_i + \hbar\mathbf{k}_e = \hbar\mathbf{k}_e - \hbar\mathbf{q} \quad (2.7)$$

to find the distribution of target electron momenta. By employing certain experimental symmetry conditions the two components  $\mathbf{q}_{0\parallel}$  and  $\mathbf{q}_{0\perp}$ , parallel and perpendicular to the incoming electron trajectory, can be found independently (respectively in a coplanar and non-coplanar setup). With high primary energies, on the order of 100 keV, it will be difficult to realize the same symmetry conditions.

Below we will discuss the relation of momentum transfer and its components with energy loss  $E$  and scattering angle  $\theta$ , see Fig. 2.4. To simplify notation of momenta we will usually omit the factor  $\hbar$ .

## 2. Physics of Coincidence Spectroscopy

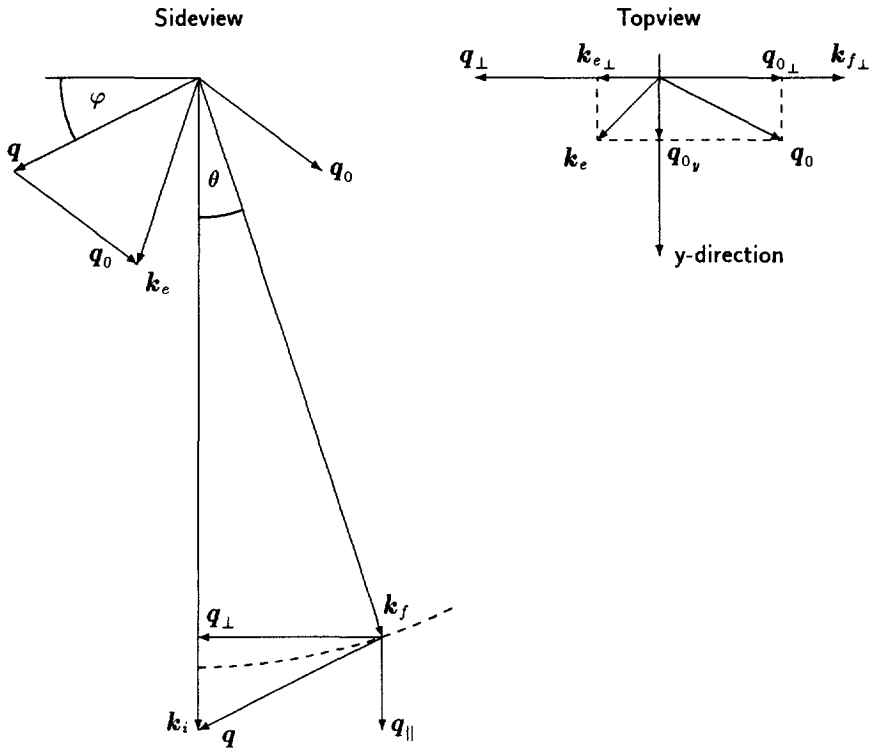


Fig. 2.4: Momentum diagram of the scattering event.

For the component of the momentum transfer in the direction of the incoming electron, we find (using relativistic kinematics)

$$q_{\parallel} = k_i(1 - \sqrt{f} \cos \theta) \quad (2.8)$$

where  $k_i$  is the magnitude of initial momentum  $\mathbf{k}_i$ , given by

$$k_i = \frac{\beta E_i}{c\hbar} \quad (2.9)$$

and

$$f = 1 - 2 \frac{E}{E_i} \frac{1}{\beta^2} + \frac{E^2}{E_i^2} \frac{1}{\beta^2} \quad (2.10)$$

with  $\beta = v/c = (1 - 1/\gamma^2)^{1/2}$ , with  $v$  the velocity of the incoming electron,  $c$  the velocity of light and  $\gamma = 1 + eV_i/m_0c^2$  the ratio of the relativistic mass  $m$  of the incoming electron and its restmass  $m_0$  with  $V_i$  the acceleration voltage of the incoming electron.  $E_i$  is the total energy of the incoming electron which includes both

the kinetic energy  $eV$ ; and the energy of an electron at rest  $m_0c^2 = 511.06 \text{ keV}$ . For practical cases ( $E < 2 \text{ keV}$ , working with 80-keV or more-energetic electrons) the second term of Eq. (2.10) is usually negligible and  $f$  will be only slightly smaller than 1. Introducing the characteristic scattering angle<sup>2</sup>  $\theta_E \equiv E/(E_i\beta^2)$  gives

$$f = 1 - 2\theta_E + \beta^2\theta_E^2. \quad (2.11)$$

For small scattering angles  $\theta$  this leads to the approximate form of Eq. (2.8):

$$q_{\parallel} \approx k_i\theta_E \quad \text{for } \theta \downarrow 0. \quad (2.12)$$

The component of  $q$  perpendicular to the incoming electron is given by

$$q_{\perp} = k_i\sqrt{f} \sin \theta \approx k_i\theta \quad \text{for } \theta \downarrow 0. \quad (2.13)$$

With the  $xz$ -plane defined to hold both  $\mathbf{k}_i$  and  $\mathbf{k}_f$  the third component of  $\mathbf{q}$ ,  $q_y = 0$ . This also implies that  $k_{e_y} = q_{0_y}$ . The size of the total momentum transfer is given by

$$q = k_i\sqrt{1 + f - 2\sqrt{f} \cos \theta} \approx k_i\sqrt{\theta^2 + \theta_E^2} \quad \text{for } \theta \downarrow 0. \quad (2.14)$$

The angle  $\varphi$  that  $\mathbf{q}$  makes with the plane perpendicular to the incoming electron is given by

$$\varphi = \arctan \left( \frac{1 - \sqrt{f}}{\sqrt{f} \sin \theta} + \tan \frac{\theta}{2} \right) \approx \frac{\pi}{2} - \frac{\theta}{\theta_E} \quad \text{for } \theta \downarrow 0. \quad (2.15)$$

This shows that  $\varphi$  starts at  $\pi/2$  for very small values of  $\theta$  (first term) and after a sharp drop, almost to zero,  $\varphi$  rises linearly toward  $\pi/2$ , going approximately like  $\varphi = \theta/2$ . Figure 2.5 shows the behavior of  $\varphi$  as a function of  $\theta$ ; both  $\theta$  and  $\varphi$  are shown on a logarithmic scale. The minimum is reached when  $\mathbf{q}$  forms the tangent to the arc described by  $\mathbf{k}_f$  at

$$\theta_{\min} = \varphi_{\min} = \arccos \sqrt{f} \approx \sqrt{2\theta_E}. \quad (2.16)$$

For example, for 80-keV electrons ( $\beta = 0.502$ ,  $k_i = 1504 \text{ nm}^{-1}$ ) and an energy loss of  $E = 385 \text{ eV}$  this gives  $\theta_E = 2.6 \text{ mrad}$  and  $\varphi_{\min} = 71.9 \text{ mrad} = 4.12^\circ$ , very nearly perpendicular to the incoming electron. This means that  $\varphi$  can range from almost zero to  $\pi/2$ . If however  $\theta$  is limited to scattering angles below  $\theta_{\min}$ , the minimum value of  $\varphi$  should be adjusted according to Eq. (2.15) or Fig. 2.5. To investigate if there is any preferential direction of emission one should include the probability of scattering over a given angle  $\theta$ .

## 2. Physics of Coincidence Spectroscopy

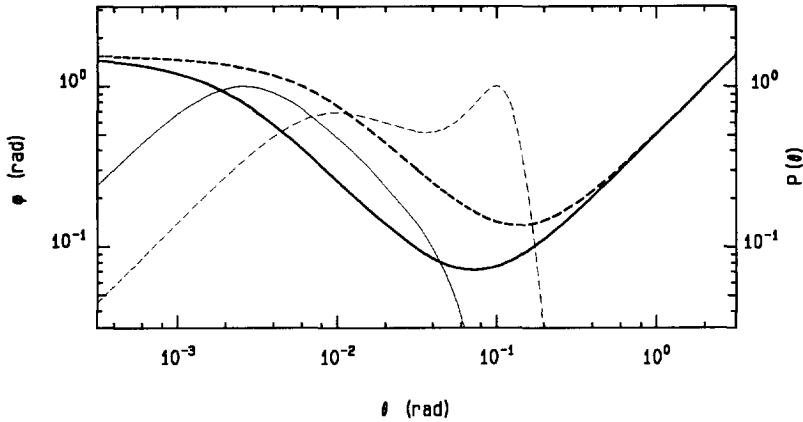


Fig. 2.5: Angle  $\varphi$  between  $\mathbf{q}$  and the normal to  $\mathbf{k}_i$  as a function of scattering angle  $\theta$ , for 80-keV electrons incident on carbon that have lost an energy of 385 eV (thick solid line), or 1385 eV (thick dashed line). The probability  $P(\theta)$  for electrons to be scattered into that angle for 385 eV loss (thin solid line) and 1385 eV loss (thin dashed line) are normalized to 1 at their maxima.

### Angular Emission Distribution for Free Atoms

The probability of scattering is treated in terms of *cross sections*. The cross section for scattering depends on the energy being lost and the solid angle that is considered. The double-differential cross section  $d^2\sigma/d\Omega dE$  represents the probability of an incident electron being scattered (per unit solid angle  $\Omega$  and per unit energy loss) by a given atom or molecule. For  $\theta \ll 1$  rad and  $E \ll E_i$  a good approximation of the double-differential cross section is given by (Egerton,<sup>2</sup> Eq. (3.29))

$$\frac{d^2\sigma}{d\Omega dE} \approx \frac{4\gamma^2 R}{Ek_i^2} \left( \frac{1}{\theta^2 + \theta_E^2} \right) \frac{df}{dE}(q, E), \quad (2.17)$$

where  $R = (m_0 e^4 / 2) / (4\pi\epsilon_0 \hbar)^2 = 13.6$  eV is the Rydberg energy and  $df/dE$  is the generalized oscillator strength (GOS) per unit excitation energy. The GOS is a quantity which describes the response of an atom when a given energy and momentum are supplied from an external source (e.g., by collision of a fast electron or by a photon). Below the (inner-shell) ionization threshold  $E_k$  the GOS is zero by definition, above the threshold it can be approximated using formulae described by Egerton,<sup>2</sup> which are based on a hydrogenic model.

By replacing  $d\Omega$  with  $2\pi \sin(\theta) d\theta$  we find the probability for scattering into an angle  $\theta$ , which is also depicted in Fig. 2.5:

$$\frac{d^2\sigma}{d\theta dE} \approx \frac{4\gamma^2 R}{Ek_i^2} \left( \frac{2\pi \sin(\theta)}{\theta^2 + \theta_E^2} \right) \frac{df}{dE}(q, E). \quad (2.18)$$

The forward scattering ( $\theta = 0$ ) vanishes. Up to about 20 mrad the shape of the probability distribution is determined by  $\theta/(\theta^2 + \theta_E^2)$  so that a maximum of the distribution is found at  $\theta = \theta_E$ . For small energy losses the GOS is concentrated at low scattering angles. At large energy loss the GOS shows an increased intensity at higher scattering angles, known as the Bethe ridge.<sup>2</sup> The Bethe ridge represents small impact parameter collisions with inner-shell electrons, where the electrostatic field of the nucleus has little influence. The maximum of the Bethe ridge appears at  $\theta \approx \sqrt{2\theta_E}$  and thus almost coincides with the value of  $\theta_{\min}$ .

It is not directly clear from both graphs in Fig. 2.5 what the resulting probability distribution for momentum transfer in the direction of  $\mathbf{q}$  will be. Therefore Fig. 2.6a shows an angular probability distribution of the momentum transfer vec-

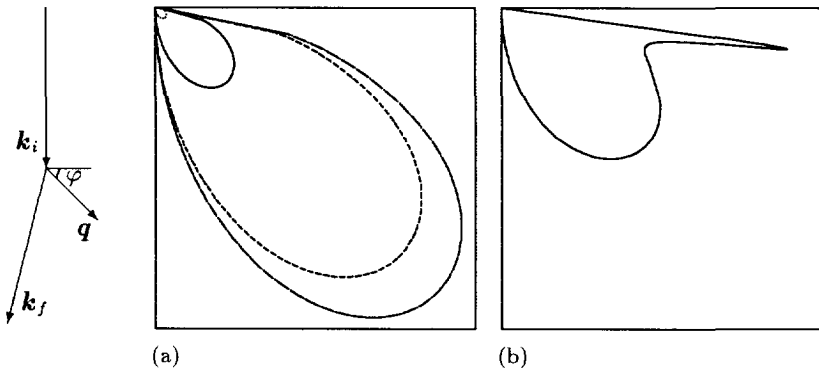


Fig. 2.6: Angular probability distribution of momentum transfer vector  $\mathbf{q}$ , for carbon  $K$ -shell ionization. The GOS is based on the hydrogenic model. Vertical direction indicates a momentum transfer along the incoming electron direction. In (a) graphs are depicted for 286-eV (dash-dotted), 295-eV (dashed), 385-eV (solid) and 585-eV (dotted) energy loss of 80-keV primary electrons, for scattering up to  $\theta = 10$  mrad. In (b) the angular distribution shows a peaked probability of momentum transfer vector  $\mathbf{q}$  for 1385-eV energy loss, without limitation on  $\theta$ . The scale of graph (b) is 833 times larger than for graph (a).

tor  $\mathbf{q}$ , for various values of energy loss. A limitation on the scattering angle of  $\theta < 10$  mrad represents a possible EELS acceptance angle. By this limitation on  $\theta$ , the direction of  $\mathbf{q}$  is also restricted to higher values of  $\varphi$ . Without this limitation, the graphs closely resemble a  $\sin(2\varphi)$  distribution. Such a distribution is normally called a cosine distribution, based on its shape in a (2-D) circular cross section of a (3-D) sphere on a surface. The cosine ( $\cos(\varphi)$ ), when multiplied with the sine (proportional to the area of rings with constant  $\varphi$ ) yields a  $\sin(2\varphi)$  (1-D) distribution.<sup>10</sup> The limitation on  $\theta$  causes the sudden drop of the probability for  $\varphi$  below a given value, thereby giving a deviation from the  $\sin(2\varphi)$  distribution. By accepting much larger values of  $\theta$  a somewhat different angular probability

## 2. Physics of Coincidence Spectroscopy

distribution can occur if Eq. (2.18) peaks at considerably higher scattering angles, due to the Bethe ridge. Such a situation is shown in Fig. 2.6b for an energy loss of 1385 eV, again for 80-keV primary electrons. Due to a decreased GOS, this figure required different scaling with respect to Fig. 2.6a. Therefore in practice this peaking will be rather difficult to observe.

Unfortunately these distribution functions are for momentum transfer vector  $\mathbf{q}$  rather than for the emitted electron momentum  $\mathbf{k}_e$ . In fact we can say that in the derivation of the double-differential cross section and the generalized oscillator strength all possible final states for the emitted electron were allowed. To find the angular distribution of the emitted electron one should consider quantum-mechanical collision theory. Maslen and Rossouw<sup>11</sup> have performed these computations for given  $E$  and  $k_e$ . A reproduction of their results is shown in Fig. 2.7. These figures show a (2-D) cross section through the (3-D) distribution, which

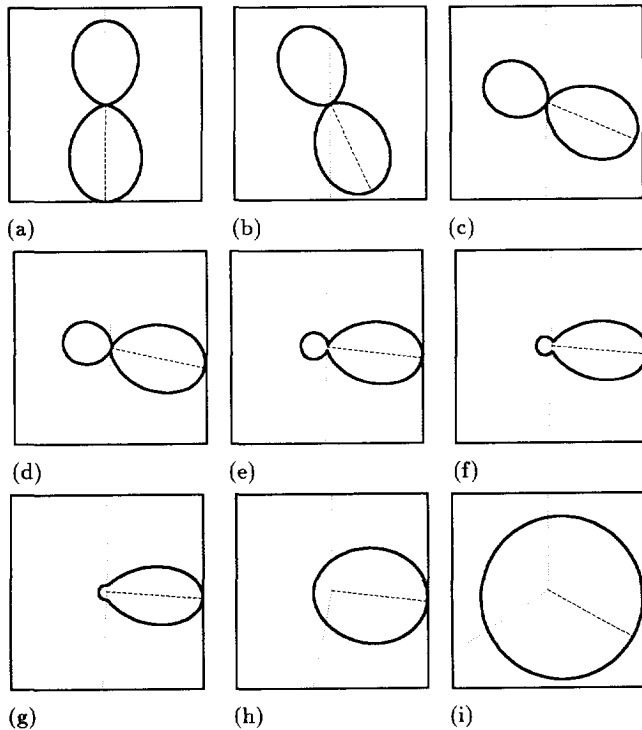


Fig. 2.7: Angular probability distribution of electron emission for given  $E$  and  $k_e$ . The path of the fast electron is shown as a dotted line, and the direction of  $\mathbf{q}$  as a dashed line. A reproduction of Maslen and Rossouw's figure,<sup>11</sup> for  $E = 385$  eV and  $k_e = 51.2 \text{ nm}^{-1}$  for 100-keV primary electrons. The following values of  $\theta$  apply: (a) 0, (b) 0.001, (c) 0.005, (d) 0.01, (e) 0.02, (f) 0.03, (g) 0.05, (h) 0.2, (i) 1.0 rad.

shows rotational symmetry around the direction of  $\mathbf{q}$ . At low angle scattering the distribution shows a p-orbital nature, which reflects the optical dipole transition. At higher angle scattering the p-type symmetry is distorted and in the limit of large  $q$  the distribution becomes spherically symmetric. All graphs have been suitably scaled and are not related in magnitude. The probability for large angle scattering is very small.

To obtain a practical emission distribution for an experiment with a given EELS acceptance angle, a suitable integration over all possible (3-D) distributions should be made. For a 50 mrad acceptance angle this is done (by numerical integration) in Fig. 2.8. The (1-D) integrated angular distribution function of Fig. 2.8a shows

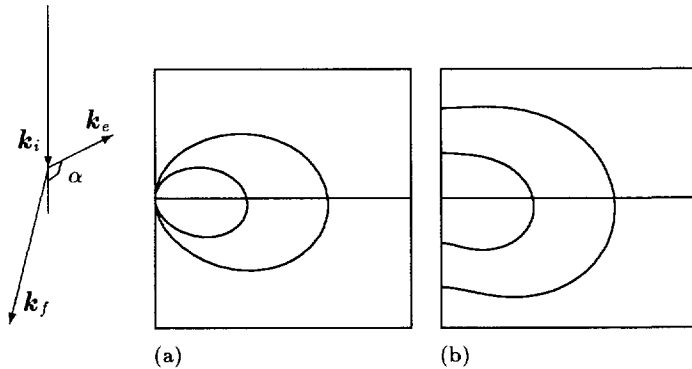


Fig. 2.8: Angular emission probability distribution for free carbon atoms in a coincidence experiment with 50 mrad EELS acceptance angle, (a)  $dI/d\alpha$  and (b)  $dI/d\Omega_\alpha$ , with  $\alpha$  the angle of  $k_e$  with  $k_i$ . Primary electron energy is 100 keV, energy loss is 318 eV for the large graph and 388 eV for the smaller graph. Top half represents backward scattering, bottom half represents forward scattering.

the preferential emission at right angles with  $k_i$ , with a slight preference for the forward direction. Fig. 2.8b shows a (2-D) cross section of the angular probability distribution. Maximum emission occurs for an (absolute) angle  $\alpha$  with the incoming electron momentum  $k_i$  of  $87.5^\circ$  and  $84.5^\circ$ , for 318 eV and 388 eV respectively. In the forward and backward direction almost the same amount of emission occurs. This figure represents scattering at free carbon atoms and does not reflect the situation where electrons are created inside a solid. Escape from the solid to the vacuum introduces workfunction effects, and these should be included for this study.

### Angular Emission Distribution for a Solid

For untilted specimens in the STEM the primary electrons enter the sample perpendicular to the surface. This means that electrons which have been emitted at right angles (or less) to the primary electron momentum, or parallel to the surface

plane, will not be able to escape to the vacuum without scattering (assuming a smooth surface). Only those electrons that are emitted with a vector component toward the surface, which is large enough to overcome the workfunction, have a chance of escaping from the surface unscattered. For the moment we will disregard the quantum-mechanical collision theory and just consider the demands on  $\mathbf{q}_0$  for free electrons. The workfunction  $\phi$  corresponds to a momentum transfer perpendicular to the surface of magnitude  $\pm\sqrt{2m_0\phi}/\hbar$ , the sign depending if it is the top or bottom solid/vacuum interface, see Fig. 2.9.

The emitted electrons can escape unscattered from the top surface when the initial momentum of the target electron along the incoming electron  $q_{0\parallel} < -\sqrt{2m_0\phi}/\hbar - k_i(1-\sqrt{f}\cos\theta)$  and from the bottom surface when  $q_{0\parallel} > \sqrt{2m_0\phi}/\hbar - k_i(1-\sqrt{f}\cos\theta)$ . Total reflection at the solid/vacuum interface occurs if  $\mathbf{q} + \mathbf{q}_0$  points toward the vacuum, but does not exceed the workfunction barrier (dotted lines in Figs. 2.9, see Figs. 2.9c and 2.9f). For example, for a workfunction  $\phi$  of 4 eV and small scattering angle  $\theta$  ( $< \theta_{min}$ ) and similar conditions as described above, this yields that  $q_{0\parallel}$  must be below  $-14.1 \text{ nm}^{-1}$  for the top surface or above  $6.3 \text{ nm}^{-1}$  for the bottom surface.

In Fig. 2.11 the required momentum  $q_{0\parallel}$  is shown as a function of energy loss  $E$  for several values of scattering angle  $\theta$ . One should realize that on the graphs, the component of  $\mathbf{k}_e$  parallel to the incoming beam is exactly zero, so that the electron is emitted under  $90^\circ$  with the normal to the surface. Electrons emitted under large angles are the most difficult to collect, see section 3.3. If only electrons with angles with the normal can be accepted that are smaller than  $\alpha_{acc}$ , the curves for the top surface will be lowered and for the bottom surface will be raised by an amount  $(q_{0\perp} + k_i\sqrt{f}\sin\theta)/\tan\alpha_{acc}$ , in both cases yielding less coincidences, see Fig 2.10. The last term rises dramatically with scattering angle  $\theta$  for small acceptance angles, and can hardly be met by demands on  $q_{0\parallel}$  alone. For example for 80-keV electrons scattered over only 10 mrad, in the limit of low energy losses ( $f \approx 1$ ) this term is already  $15 \text{ nm}^{-1}$ , for a  $45^\circ$  acceptance angle. If on the other hand we regard this term as a demand on  $q_{0\perp}$  the magnitude seems reasonable (is on the same order as the demand on  $q_{0\parallel}$ ) and then it is also independent of the actual acceptance angle. For smaller acceptance angles and bigger scattering angles than in this numerical example the demands on both components of  $\mathbf{q}_0$  become quite strong and only a very small fraction of the events will yield a detectable emitted electron. It is therefore quite important to work with high acceptance angles for the emitted electrons in coincidence spectroscopy.

Previous coincidence measurements<sup>12</sup> at carbon *K*-shell excitation energies have shown that (for that case)  $\mathbf{q}_0$  has a quite wide bell-shaped momentum distribution, centered around zero, which falls off to half the maximum height at (roughly estimated)  $\pm 40 \text{ nm}^{-1}$ . For carbon *L*-shell excitation this half height is reached at about  $\pm 15 \text{ nm}^{-1}$ , a value where some of the graphs for top surface escape give evidence of a loss of signal.

If we incorporate the workfunction effects on the angular distribution model



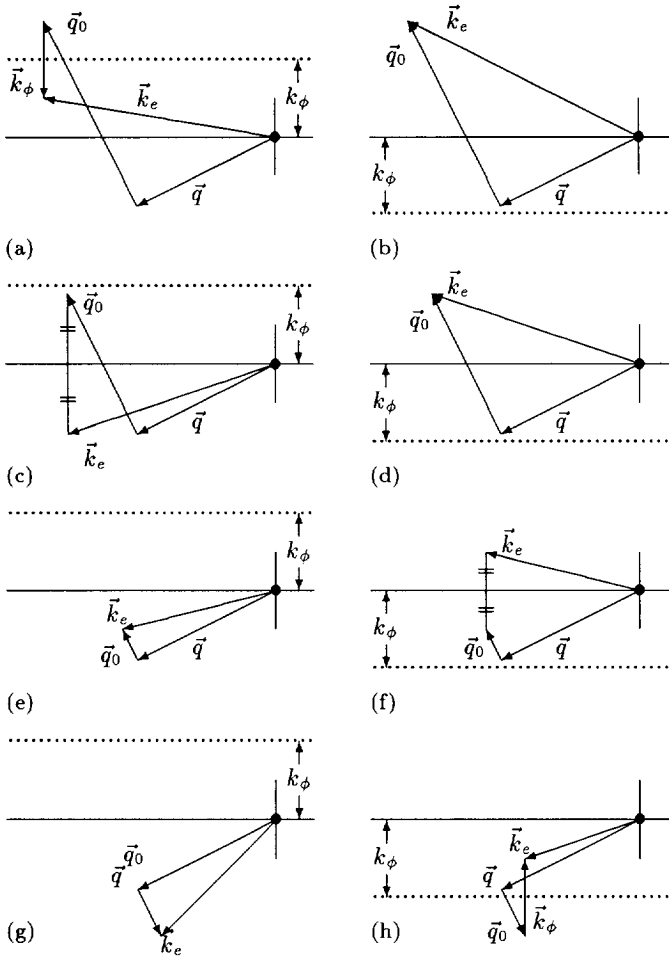


Fig. 2.9: Construction of momentum  $\vec{k}_e$  of the emitted electron. The left figures represent the situation at the top surface, the right figures the bottom surface. Only in (a) and (h) escape from the surface is possible. In (c) and (f) total reflection at the solid/vacuum interface occurs.

which is based on the quantum-mechanical collision theory, we can find the counterpart of Fig 2.8 for a solid. Figure 2.12 shows the angular emission probability distribution for the top and bottom surfaces of a solid, assuming a primary electron entering the solid perpendicular to the (top) surface. In the computations for the figure the solid/vacuum interface has been treated as if it causes total reflection when the momentum component toward the vacuum is not large enough to overcome the workfunction threshold. Since on an atomic scale the surface will not be

## 2. Physics of Coincidence Spectroscopy

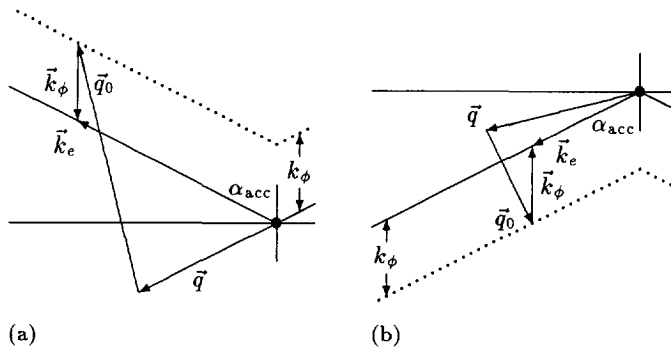


Fig. 2.10: Construction of momentum  $k_e$  of the emitted electron, for an acceptance angle  $\alpha_{acc} < 90^\circ$ . (a) represents the situation at the top surface, (b) at the bottom surface. The sum of  $q + q_0$  should reach beyond the dotted line to enable emission inside the acceptance angle.

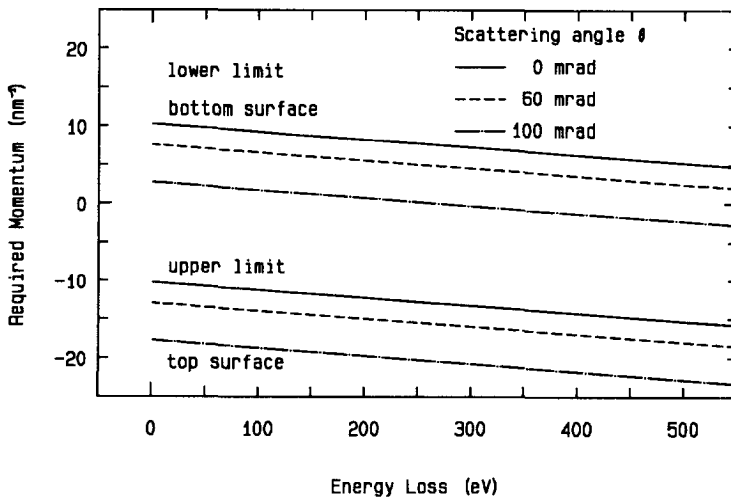


Fig. 2.11: Required momentum  $q_{0\parallel}$  as a function of energy loss  $E$  for several values of scattering angle  $\theta$  for electrons of energy  $E_0 = 80$  keV and an acceptance angle of  $90^\circ$ .

perfectly smooth, this reflection will only give an indication of the actual emission distribution. Perhaps it should be stressed that this distribution does not incorporate any subsequent scattering after the initial scattering event. If such subsequent scattering is unlikely ( $\lambda_{el} \ll t$ , with  $t$  the thickness of the sample), or if it is mainly inelastic ( $\lambda_{inel} \ll \lambda_{el}$ , see section 2.3) so that energy losses of the emitted electron associated with this scattering can be excluded from the coincident measurement,

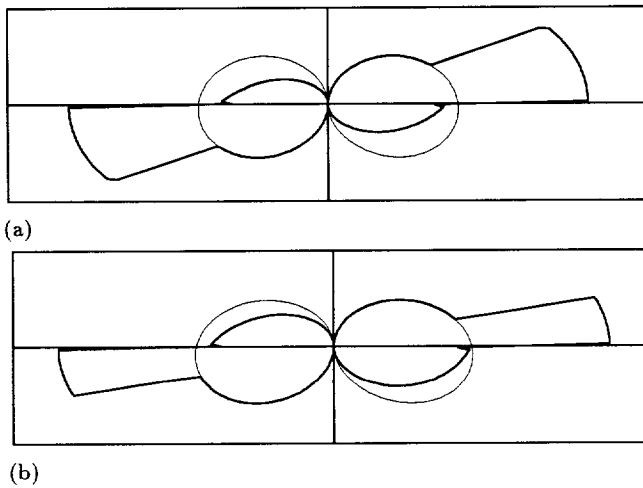


Fig. 2.12: Angular emission probability distribution for carbon film in a coincidence experiment with 50 mrad EELS acceptance angle. Primary electron energy is 100 keV, energy loss in (a) is 318 eV and in (b) 388 eV. A 4-eV workfunction is assumed. For comparison, the results without a workfunction effect are also shown (thin lines). The left part of the figure represents a collision near the top surface of the film, while the right part represents a collision near the bottom surface: upper left backward emission from top surface, lower left forward emission into the sample, lower right forward emission from bottom surface and upper right backward emission into sample.

the figure gives an adequate description of the expected angular distribution. For example, for 100-keV electrons which transfer 318 eV to carbon  $K$ -shell electrons (close to the top surface), about 28.5% of these electrons escape from the top surface. From the bottom surface 31.1% of the electrons escape. For an energy loss of 388 eV the workfunction threshold is less important and these percentages are 35.1 and 40.5% respectively.

### Selection of Momentum Transfer in the STEM

In order to perform measurements as a function of momentum transfer one can select a limited range of values of  $\theta$  in the microscope. The precision with which the momentum transfer is measured is then (for  $\theta > \theta_E$ ):  $\Delta(\hbar q) = \hbar k_i \Delta\theta$  or  $\Delta q = (2\pi/\lambda_i) \Delta\theta$  where  $\lambda_i$  is the incident electron wavelength. When aiming for the highest spatial resolution (with highest current density), for example, a combined diffraction and spherical aberration limited 1 nm spot with a lens which has a coefficient of spherical aberration  $C_s = 2.4$  mm, an illumination half-angle of about 9 mrad has to be used, see section 3.1. This illumination angle will be convoluted with the acceptance angle of the spectrometer to give a value of at least

$\Delta\theta = 18$  mrad, which yields an inaccuracy in determining the momentum transfer of  $\Delta q = 26.5 \text{ nm}^{-1}$  (for 80-keV electrons). For inner-shell electron excitation large momenta of the target electrons can occur so that such momentum precision might be of some practical use. For valence electrons values of  $q_0$  are found in the range of 0 to  $40 \text{ nm}^{-1}$ ,<sup>13</sup> which indicates that at this resolution no effective discrimination against momentum is possible.

At the cost of a reduced probe current one can use smaller opening angles and thus gain in momentum precision, but at some point one loses spatial resolution due to the diffraction contribution. With the diameter of the diffraction contribution to the spot size  $d_{\text{diff}} \approx \lambda_i/(2\theta)$  this yields that  $\Delta q \approx \pi/d_{\text{diff}}$ . In the limiting case where  $d_{\text{diff}} = d_{\text{tot}}$  (at zero probe current)  $\Delta q = 3 \text{ nm}^{-1}$ . At these values, however, the second term (with  $\theta_E$ ) in the approximate form of Eq. (2.14) is dominant at low scattering angles  $\theta$ , so that  $dq/d\theta$  and the momentum precision approach zero.

### 2.3. Transport to and Escape from the Surface

After the initial scattering event the electron(s) knocked out of the target system have to reach the surface. Above a treatment was given for unscattered escape, basically for an isolated target atom near a flat potential barrier (simulating the workfunction). In a real solid it is also possible that subsequent scattering takes place. Elastic scattering, without appreciable energy loss, causes diffusion of the angular emission profile of the emitted electron. If this happens several times before the escape the angular profile is expected to become isotropic. Compared to the original forward orientation of the emitted electrons this can be an improvement since more electrons escape from the top surface without further (cascade) losses.

A more serious problem is inelastic scattering since this is accompanied by non-negligible energy losses to the individual electrons, giving rise to the term  $E_{\text{casc}}$  (see Fig. 2.2). Also 'new' electrons may be released in such collisions, having a kinetic energy anywhere from zero up to the original kinetic energy of the electron that released them. (Inside the solid the kinetic energy should be interpreted as being defined with respect to the Fermi level.) This causes changes in the secondary electron energy distribution in such a sense that original structures in this distribution (directly after the fast electron impact) get smeared out toward lower energies. If this process is repeated several times in a so-called cascade, a relatively large amount of electrons will have energies close to zero. On escaping from the surface the workfunction suppresses the low energy part of this distribution (between  $E_{\text{vac}}$  and  $E_F$ ). The remaining part of the low energy electrons that appear as the main contribution to the electron energy distribution are generally referred to as *secondary electrons*.

A measure for both types of scattering is given by the average distance traveled between two of those scattering events, the so-called *mean free path*  $\lambda$ , which can be defined for each type of scattering. The mean free path is inversely proportional to the atomic density  $n_a$  and to the scattering cross section  $\sigma$ , which is a direct

measure of the intensity of scattering from each atom in any direction and for any energy loss. For example for inner-shell scattering of fast electrons, the cross section  $\sigma$  can be computed by suitable integration of Eq. (2.17). The mean free path for inelastic scattering ( $\lambda_{\text{inel}}$ ) depends both on material properties and on energy. For energies up to about 30 eV  $\lambda_{\text{inel}}$  decreases with energy down to values below 1 nm and for higher energies  $\lambda_{\text{inel}}$  starts to rise again with energy;<sup>14</sup> see Fig 2.13. For

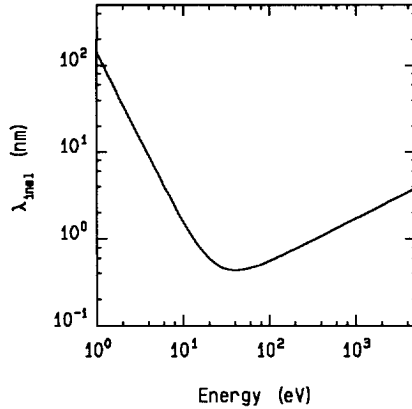


Fig. 2.13: Mean free path for inelastic scattering of an electron, as a function of its energy above Fermi level (from Seah and Dench<sup>14</sup>). The curve represents a least-squares fit to experimental data, measured for a variety of elements.

metals the mean free path for elastic scattering ( $\lambda_{\text{el}}$ ) is approximately equal to  $\lambda_{\text{inel}}$  above energies of 20 eV, and is slightly smaller than  $\lambda_{\text{inel}}$  for lower energies.<sup>15,16</sup> For other materials  $\lambda_{\text{el}}$  will show a similar behavior. With specimen thicknesses  $t$  on the order of 10 nm or more, and a mean free path of 0.5–2 nm for kinetic energies of 5–2000 eV, this means that unscattered escape from the bulk of the specimen is unlikely. The angular emission probability will therefore tend to become more isotropic.

As mentioned before, the escape from the surface is accompanied by a loss in vertical momentum as described by the workfunction ( $\sqrt{2m_0\phi}$ ). The component of momentum along the surface is not affected. Of course this only holds for smooth surfaces. Depending on the degree of surface roughness the energy and angular distributions can be somewhat changed.<sup>17</sup>

Another measure for the amount of scattering and therefore for the degree of surface sensitivity of the technique is the *escape depth*. It's value describes the average depth from where electrons can reach the surface. It is directly related to the mean free path, but includes the fact that for larger angles of emission a larger path in the solid must be traversed before actual escape is possible. If the workfunction is disregarded the thickness of the layer from which the electrons can escape is  $\lambda \cos \vartheta$ , where  $\vartheta$  is the angle with the normal to the surface. A

single (averaged) value for the escape depth can only be given for a known angular emission distribution. As a rule of thumb the escape depth can be taken equal to the mean free path.

## 2.4. Comparison with Photo Absorption

We will now compare electron excitation to photon excitation, based on energy and momentum, as well as on excitation probabilities.

### 2.4.1. Comparison of Energy and Momentum Transfer

In terms of energy, the analogy with photo electron spectroscopy is suitably expressed by Eq. (2.5) in the equivalence of energy loss and photon energy.

The comparison in terms of momentum is not that straightforward. A photon of energy  $E_{\text{ph}} = \hbar\omega$  has an associated momentum  $\mathbf{p}_{\text{ph}} = \hbar\mathbf{k}_{\text{ph}}$ , directed along the propagation direction of the photon, with the size of the wavevector given by  $k_{\text{ph}} = \omega/c$ . For low-energy photons  $\omega/c$  can often be neglected relative to typical electron momenta (e.g.  $k_{\text{ph}} \approx 2 \text{ nm}^{-1}$  for a 385-eV photon).

Since the photon is absorbed in the excitation process, the momentum transfer vector  $\mathbf{q}$  is equal to  $\mathbf{k}_{\text{ph}}$ , and  $\mathbf{k}_e = \mathbf{q}_0 + \mathbf{k}_{\text{ph}}$ . Emitted electrons can escape unscattered from the top surface when  $q_{0\parallel} < -\sqrt{2m_0\phi}/\hbar - \omega/c$  and from the bottom surface when  $q_{0\parallel} > \sqrt{2m_0\phi}/\hbar - \omega/c$ . Introduction of a collection half angle  $\alpha_{\text{acc}} < 90^\circ$  gives equal additional demands on momentum as for electron excitation. For a photon of 385 eV and  $90^\circ$  collection angle we find that  $q_{0\parallel}$  must be below  $-12.2 \text{ nm}^{-1}$  for the top surface and above  $8.3 \text{ nm}^{-1}$  for the bottom surface. The required momentum for photon excitation as a function of photon energy shows a straight declining line, just like for electron excitation. For small  $\theta$ , using Eq. (2.12) as well as  $E_i = \gamma m_0 c^2$  and  $p_i = \gamma m_0 v = \hbar k_i$ , one can find that for electron excitation the slope in a graph of  $p_{0\parallel}$  against  $E$  is steeper by a factor  $1/\beta$  (cf. Fig. 2.11). This shows that for the top surface real photo electron spectroscopy as compared to coincidence electron spectroscopy can yield a slightly larger fraction of unscattered and emitted electrons. From the bottom surface coincidence electron spectroscopy yields more unscattered electrons. From this point of view coincidence electron spectroscopy from the top surface is more surface sensitive.

Another interesting observation can be made in this context. As in normal EELS, the transitions that appear predominantly in the coincidence spectrum are those for which the dipole-selection rules apply, as in x-ray absorption. For relatively small scattering angles  $\theta$ , the momentum transfer is primarily forwardly directed and approaches the value given by Eq. (2.12) ( $\hbar k_i \theta_E$ ) which can be rewritten to  $\hbar\omega/v = E/v$ . The momentum transfer upon photon absorption of the same energy  $E$  is  $\hbar q_{\text{ph}} = E/c$ . The ratio of momentum transfer in the two cases is therefore  $c/v$  and is less than two for incident energies above 80 keV. Therefore the optical selection rule  $\Delta l = \pm 1$  applies approximately to the coincidence

measurements at low scattering angles. In theoretical treatments of electron scattering the dipole approximation is often made. However at 80 keV incident energy, scattering angles on the order of  $\theta_E$  and larger can already give rise to non-dipole transitions, so-called optically forbidden transitions. To some extent this can cause more complicated spectra, which on the other hand opens the way to additional physical information.

### 2.4.2. Comparison of Excitation Probability

To compare electron-impact excitation with photon-impact excitation, it is convenient to work with cross sections. The photoabsorption cross section  $\sigma_p(E)$ , which represents the probability that an incident photon of energy  $E$  is absorbed by a given atom or molecule, is defined as  $\sigma_p = \mu/n$  where  $n$  is the number of atoms or molecules per unit volume. The photoabsorption coefficient  $\mu$  is defined through the relationship  $I = I_0 e^{-\mu t}$ . Here  $I_0$  represents the intensity of the photon flux incident on a piece of material of thickness  $t$  and  $I$  is the intensity of the transmitted flux.

For electrons one can use the double-differential cross section  $d^2\sigma/d\Omega dE$  of Eq. (2.17). Integration over the acceptance angle of the energy-loss spectrometer yields the energy-differential cross section. Further integration over the range of energy losses covered in the spectrum gives the total cross section. These cross sections (for  $K$  and  $L$  shell excitations) can be computed using adaptations of the SIGMAK2 and SIGMAL2 programs provided by Egerton.<sup>2</sup>

At low scattering angles and relatively low energy loss, the generalized oscillator strength per unit energy  $df/dE$  is almost constant (independent of  $q$  and  $\theta$ ) and can be approximated by  $df_k(0, E)/dE$ . Together with  $(df/dE)_{bg}$  the "background" contribution from outer shells of lower binding energy they form the optical oscillator strength per unit energy  $df(0, E)/dE$ , which is proportional to the photoabsorption cross section  $\sigma_p$  (Egerton,<sup>2</sup> Eq. (3.115)):

$$\frac{df(0, E)}{dE} = \frac{df_k(0, E)}{dE} + \left(\frac{df}{dE}\right)_{bg} = \frac{\sigma_p}{C}, \quad (2.19)$$

where  $C = 1.097 \times 10^{-20} \text{ m}^2 \text{ eV}$ .

Since jump ratios (the ratio between intensity just after and just before the edge) are on the order of 10 (in pure materials), the error made by discarding the background term in Eq. (2.19) is on the order of 10%. Integration over the actual range of collection angles from 0 to  $\theta_{max}$  yields an energy-differential cross section

$$\frac{d\sigma(E)}{dE} = \frac{4\pi\gamma^2 R\sigma_p}{Ek^2 C} \ln \left[ 1 + \left( \frac{E_i\beta^2\theta_{max}}{E} \right)^2 \right]. \quad (2.20)$$

The ratio between the energy-differential electron-scattering cross section and photoabsorption cross section, which follows directly from this equation, is shown

## 2. Physics of Coincidence Spectroscopy

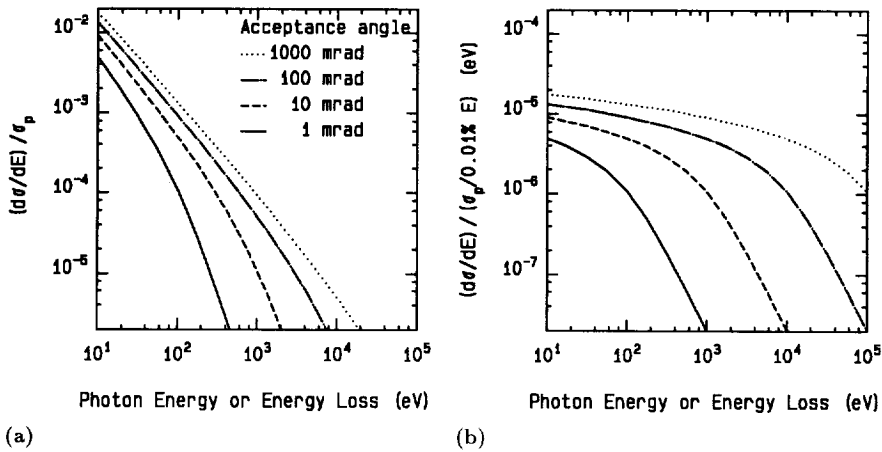


Fig. 2.14: (a) Ratio between energy-differential electron excitation  $d\sigma(E)/dE$  (for 100-keV electrons) and photoabsorption cross section  $\sigma_p$ , and (b) this same ratio multiplied with a bandwidth of 0.01% of the photon energy.

in Fig. 2.14a. We see that the photoabsorption cross section is orders of magnitude greater than the electron energy-loss cross section. To get a comparable number of inner-shell excitation events one needs more incident electrons than photons. This does not mean that photon impact spectra will always be preferable; see, e.g., Isaacson and Utlaut.<sup>18</sup> The energy bandwidth of the photon sources is normally a small percentage of the photon energy, set by the monochromator grating. In Fig. 2.14b the ratio has therefore been multiplied by a variable bandwidth of 0.01% of the photon energy. The comparison is then much less varying over the energy range, while differences due to angular acceptance are more clearly visible. Roughly speaking one needs  $10^5$  to  $10^6$  electrons to simulate one photon.

Photon sources such as synchrotrons are most often characterized by a spectral brightness, which is defined as a photon flux per second, through a surface, within a solid angle per 0.1 or 0.01% bandwidth. The comparable number for electron excitation should then be a flux of electrons per second, through a surface, within a solid angle, multiplied by the bandwidth corrected ratio of Fig. 2.14b. As will be shown in section 3.1, the electron flux can be taken as  $6 \times 10^{18} \text{ s}^{-1} \text{ mm}^{-2} \text{ mrad}^{-2}$  (based on a current of 0.183 nA in a 1 nm diameter spot with a half opening angle of 8.8 mrad). In Fig. 2.15a several spectral brightness data for photon radiation sources have been compared with the electron impact equivalent. In case the coincidence experiment can be performed with a parallel EELS detector, the equivalent photon flux is in principle increased by a factor on the order of the number of parallel channels. The decrease in acceptance angle which is accompanied with the different modes of operation for the parallel detection, will however reduce this



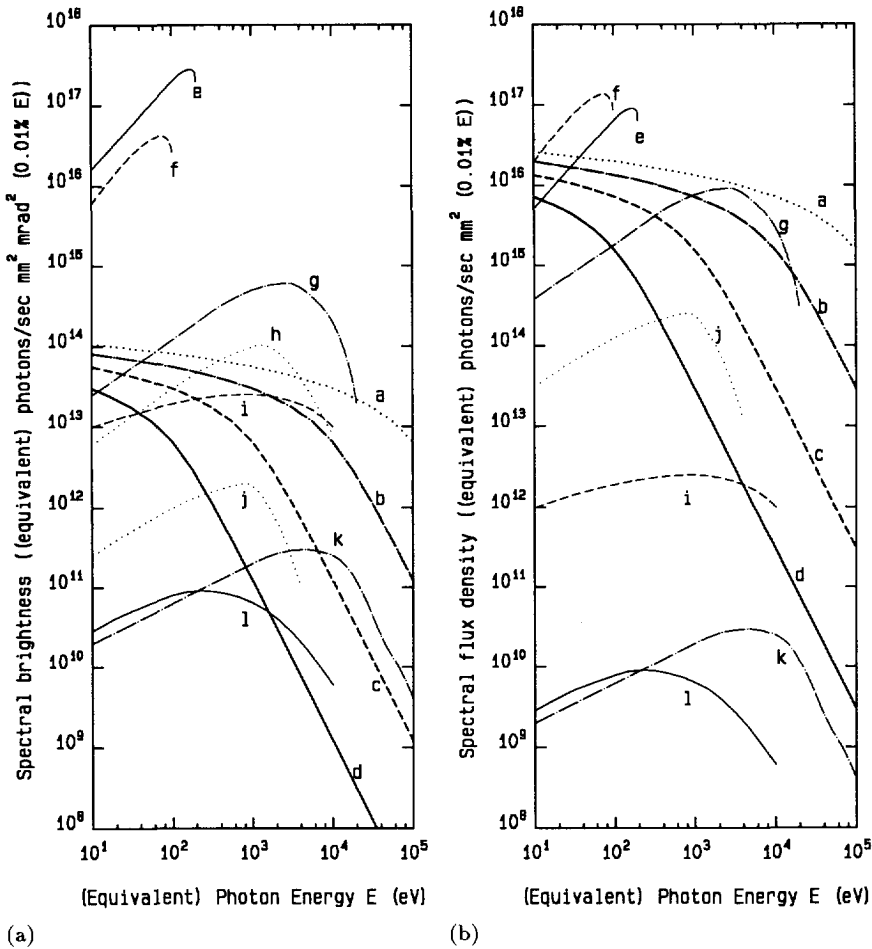


Fig. 2.15: Comparison of (a) spectral brightness and (b) flux density data of photon radiation sources (e-l) and the equivalent data for electron impact in a STEM (a-d). The data in (b) have been obtained by a multiplication of the data in (a) by the solid angle. Curves a-d represent the electron impact case, respectively for 1000, 100, 10 and 1 mrad acceptance angle. Curves e-h are for the Advanced Light Source,<sup>19</sup> respectively for undulator u9, u20, a wiggler and a bend. Curve i is for the NSLS instrument,<sup>18</sup> j for BESSY,<sup>20</sup> k for DORIS<sup>18</sup> and l for SPEAR.<sup>18</sup> For the BESSY data a 20 mrad opening angle from a zone plate was taken, which has been multiplied by a conservative 10% efficiency, due to the zone plate itself and for the better monochromatization which is required for the zone plate to provide good focusing.

effect to a large extent, see Chapter 3.

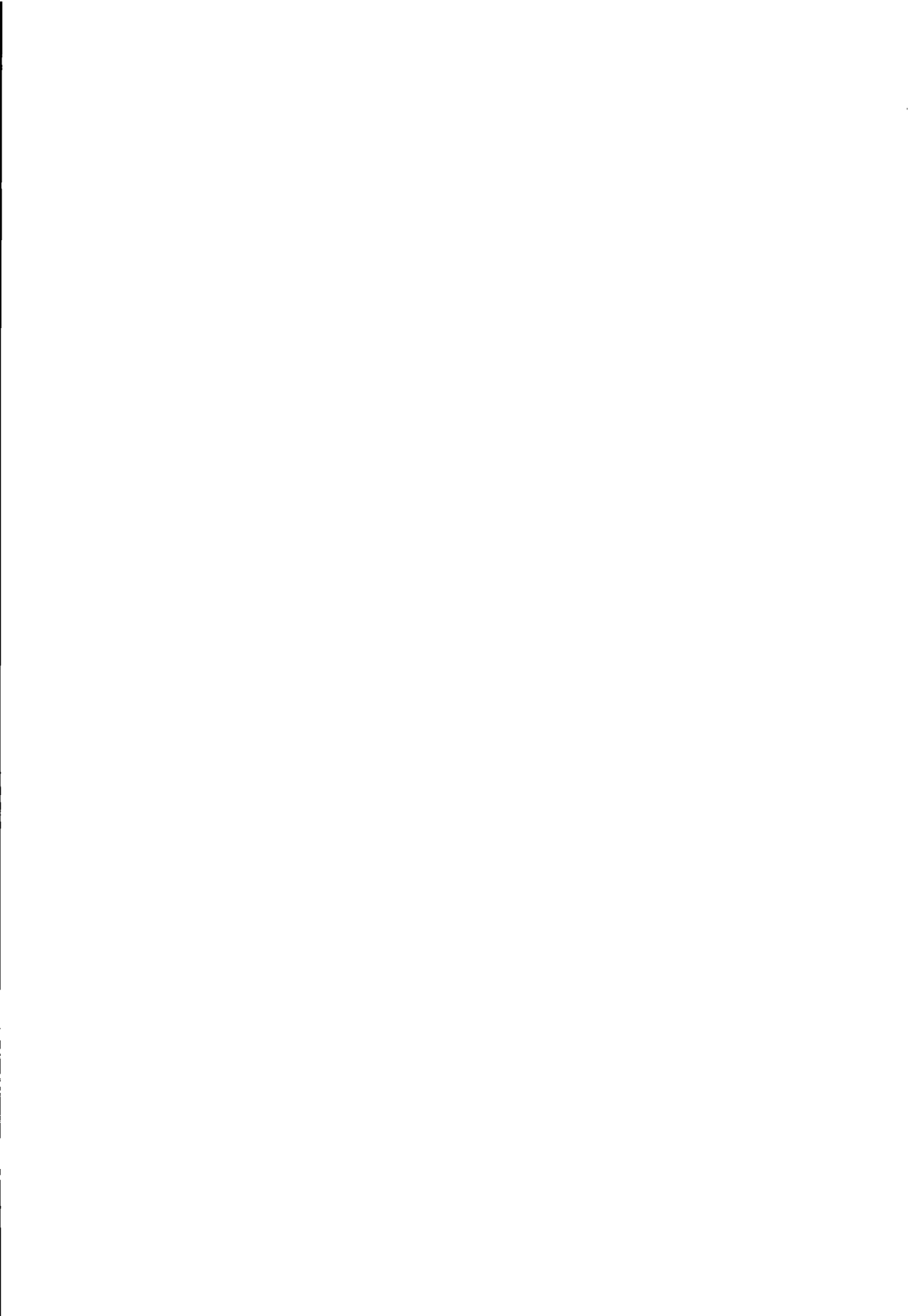
To study the equivalent spectral photon flux through a surface, the data of Fig. 2.15a have been multiplied by an appropriate solid angle for each source in Fig. 2.15b. For electron impact the solid angle is given by the probe angle at the specimen plane. For synchrotron sources the maximum collection angle from the undulator, wiggler or bend is taken, assuming that it is possible to focus this radiation with unit magnification in an equal solid angle. Focusing with less than unit magnification, for example by means of zone plates, increases the solid angle, but is on the other hand accompanied by other losses. The efficiency of monochromatization of the synchrotron-radiation sources is not yet included in this figure. It is expected to be on the order of 10 %, depending on the required energy resolution. Ideal for this comparison would be monochromatization to the same energy resolution as is obtainable with EELS. Conclusion of Fig. 2.15b is that if the total (equivalent) photon flux on a sample is the most important factor (for example when searching for ultra-small fractions of a given element) the electron-impact case can be a good alternative to synchrotron radiation sources.

A point which is not yet specifically mentioned here is the difference in spatial resolution. For the electron-impact case an obvious measure is the 1 nm diameter probesize. The synchrotron radiation sources have source sizes (and with unit magnification also probe sizes) on the order of several tens of micrometers. Developments in reducing probesizes of x-ray systems have not reached their limit yet, but it is expected that any progress on this point is accompanied by some loss of intensity, either due to absorption or diffraction in the focusing elements or in the monochromator. Although some synchrotron sources have comparable or somewhat higher flux densities, taking spatial resolution into consideration definitely favors the electron-impact situation.

## 2.5. References

- <sup>1</sup> P. K. Ghosh, *Introduction to Photoelectron Spectroscopy*, Vol. 67 of *Chemical Analysis*, p. 13. (Wiley, New York, 1983).
- <sup>2</sup> R. F. Egerton, *Electron Energy-Loss Spectroscopy in the Electron Microscope*. (Plenum Press, New York, 1986).
- <sup>3</sup> M. S. Chung and T. E. Everhart, *Role of plasmon decay in secondary electron emission in the nearly-free-electron metals. Application to aluminum*, Phys. Rev. B **15**, 4699 (1977).
- <sup>4</sup> J. Devooght, J. -C. Dehaes, A. Dubus, M. Cailler and J. -P. Ganachaud, *Theoretical Description of Secondary Electron Emission Induced by Electron or Ion Beams Impinging on Solids*, Vol. 122 of *Springer Tracts in Modern Physics*, p. 67, in *Particle Induced Electron Emission I*, edited by G. Höhler. (Springer-Verlag, Berlin, 1991).
- <sup>5</sup> H. Kohl and H. Rose, *Theory of image formation by inelastically scattered electrons in the electron microscope*, Adv. in Electronics and Electron Physics **65**, 173 (1985).
- <sup>6</sup> L. Ungier and T. D. Thomas, *Near threshold excitation of KVV Auger spectra in carbon monoxide using electron-electron coincidence spectroscopy*, J. Chem. Phys.

- 82, 3146 (1985).
- <sup>7</sup> P. A. Wolff, *Theory of secondary electron cascade in metals*, Phys. Rev. **95**, 56 (1954).
  - <sup>8</sup> C. Kittel, *Introduction to Solid State Physics*. (Wiley, New York, 1976).
  - <sup>9</sup> I. E. McCarthy and E. Weigold, *Wavefunction mapping in collision experiments*, Rep. Prog. Phys. **51**, 299 (1988).
  - <sup>10</sup> L. Dubbeldam. *A voltage contrast detector with double channel energy analyzer in a scanning electron microscope*. PhD thesis, Delft University of Technology, November 1989.
  - <sup>11</sup> V. W. Maslen and C. J. Rossouw, *The inelastic scattering matrix element and its application to electron energy loss spectroscopy*, Philosophical Magazine A **47**, 119 (1983).
  - <sup>12</sup> R. Camilloni, A. Giardini Guidoni, R. Tiribelli and G. Stefani, *Coincidence measurements of quasifree scattering of 9-keV electrons on K and L shells of carbon*, Phys. Rev. Lett. **29**, 618 (1972).
  - <sup>13</sup> P. Hayes, J. F. Williams and J. Flexmann, *Transmission (e, 2e) coincidence measurements of thin evaporated carbon, graphite, and aluminum-aluminum oxide thin foils*, Phys. Rev. B **43**, 1928 (1991).
  - <sup>14</sup> M. P. Seah and W. A. Dench, *Quantative electron spectroscopy of surfaces: A standard data base for electron inelastic mean free paths in solids*, Surf. Interface Anal. **1**, 2 (1979).
  - <sup>15</sup> H. Kanter, *Slow-electron mean free paths in aluminum, silver, and gold*, Phys. Rev. B **1**, 522 (1970).
  - <sup>16</sup> M. Rösler and W. Brauer, *Theory of Electron Emission from Nearly-Free-Electron Metals by Proton and Electron Bombardment*, Vol. 122 of *Springer Tracts in Modern Physics*, p. 1, in *Particle Induced Electron Emission I*, edited by G. Höhler. (Springer-Verlag, Berlin, 1991).
  - <sup>17</sup> H. Raether, *Surface Plasmons on Smooth and Rough Surfaces and on Gratings*, Vol. 111 of *Springer Tracts in Modern Physics*. (Springer-Verlag, Berlin, 1988).
  - <sup>18</sup> M. Isaacson and M. Utlaut, *A comparison of electron and photon beams for determining micro-chemical environment*, Optik **50**, 213 (1978).
  - <sup>19</sup> Lawrence Berkeley Laboratory, *Conceptual design for the 1–2 GeV synchrotron radiation source*, Light Source Report **1** (1986).
  - <sup>20</sup> N. M. Ceglio, *Revolution in x-ray optics*, J. of X-ray science and technol. **1**, 7 (1989).



### 3. Instrumental Aspects of the Coincidence Experiment

Coincidence experiments can be done in many different ways. Parameters which characterize such experiments will be discussed in this chapter. Choices must be made to keep some of the parameters free and others fixed. In this work the focus lies on coincidence spectroscopy for elemental and chemical analysis at high spatial resolution, based on measurements of transmitted and emitted electrons. Instrumental demands will be discussed for this type of experiments.

As in any analytical technique, adequate signal strength is important to make the analysis useful. This signal strength must be compared with background or noise levels. Signal strength is determined by the amount of coincidence events that are initiated and the efficiency (for both detectors) with which these events are registered. Spectral resolution also plays a role in signal strength. Background and noise levels are in a similar way determined by other (non-coincident) events.

The reason to choose a transmission electron microscope as a basis for coincidence experiments was the possibility to combine spatial resolution with high detection efficiencies. The first requirement for adequate signal strength in our type of spectroscopy is the generation of sufficient coincidence events in a small area. This is equivalent to focusing a large amount of electrons to a small spot on the sample. Such focusing is only possible with short focal length lenses with small coefficients for chromatic and spherical aberrations. Above that, to get small spot-sizes, the 'illuminating' electrons should have high energy, small energy spread and come from a bright source. Present day STEMs are built to have optimum performance in combining these features.

The second requirement for sufficient signal strength is good detection efficiency for transmitted and emitted electrons at adequate energy resolution. For transmitted electrons, the EELS on STEM systems has proven to be capable of large acceptance angles. At high acceleration voltages the scattering is limited to relatively small angles, which can lead to high detection efficiency and useful energy resolution. For emitted electrons, the magnetic parallelizer approach yields a very high detection efficiency if combined with a 90° beam separator, a lens system and a concentric hemispherical analyzer. Again this magnetic parallelizer approach works best when used in combination with incident electrons of high energy. The detectors behind these systems must be able to detect individual electrons with high efficiency, if possible in many parallel channels.

### 3. Instrumental Aspects of the Coincidence Experiment

A third requirement is the ability to tune the instrument to get optimum ratios of signal to background and noise. The STEM is most suited for this tuning due to the large number of optical elements in the illumination section as well as in the detection sections for both the energy loss electrons and the emitted electrons. Other aspects which influence how well true coincidences can be distinguished from uncorrelated events are given by timing accuracy and signal processing in the coincidence electronics. Together with sample parameters these coincidence parameters determine the required settings of the instrument and the limits of the technique.

To cover above mentioned requirements, this chapter is divided into sections on probe formation (3.1), energy loss measurement (3.2), emitted electron measurement (3.3), electron detection (3.4) and coincidence parameters (3.5).

#### 3.1. Probe Formation

Several aspects of coincidence spectroscopy in the STEM depend strongly on the properties of the probe forming or 'illumination' system. The primary beam is characterized by several parameters: the acceleration voltage  $V_i$  or equivalently the energy  $E_i$ , the acceleration voltage spread  $dV$  or the energy spread  $\Delta E$ , the primary beam current in the probe  $I_{\text{probe}}$ , the illumination half-opening angle  $\alpha$  and the spotsize  $d$ ; see Fig. 3.1. Unfortunately the parameters cannot be controlled

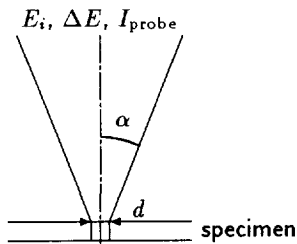


Fig. 3.1: Parameters of the illumination.

independently. They are strongly related via the available brightness of the electron source. First the relation between these parameters will be discussed, followed by the effects each of them exerts on the quality of the coincidence technique. A short discussion of non-rotationally symmetric aberrations and possible instabilities of the probe will conclude this section of the probe forming optics.

##### 3.1.1. Relation between Probe Forming Parameters

The purpose of the probe forming optics in a STEM is to image the electron source on the sample. In order to obtain high spatial resolution, the illumination

system of a STEM contains several lenses. Due to inherent aberrations of axially symmetric lens systems, the image of the electron source cannot be infinitely small. To estimate the amount of current that can be realized in a probe of a certain size one can use several approaches. In one approach the different aberrations are treated as being completely independent. In the squared summation method it is assumed that on top of this simplification the resulting distributions due to each aberration have a Gaussian character. A physically more correct approach, especially for small probe sizes, is based on a wave-optical treatment. Both methods will be discussed below.

### Squared Summation Approach

Standard procedure to determine the probe size as a function of probe current is to treat all different contributions as being roughly of Gaussian character, so that the total diameter  $d_{\text{tot}}$  of a spot can be computed from:

$$d_{\text{tot}}^2 = d_{\text{geo}}^2 + d_{\text{sph}}^2 + d_{\text{chr}}^2 + d_{\text{diffr}}^2. \quad (3.1)$$

The size of the geometrical image of the gun  $d_{\text{geo}}$  is given by

$$d_{\text{geo}} = M d_{\text{gun}}, \quad (3.2)$$

where  $d_{\text{gun}}$  is the diameter of the gun and  $M$  is the magnification from gun to specimen. The spherical aberration disc  $d_{\text{sph}}$  is given by

$$d_{\text{sph}} = \frac{1}{2} C_s(M) \alpha^3, \quad (3.3)$$

with  $\alpha$  the half opening angle of the beam on the specimen side and  $C_s(M)$  the coefficient of spherical aberration of the illumination system, which depends on magnification. The chromatic aberration disc  $d_{\text{chr}}$  is given by

$$d_{\text{chr}} = C_c \frac{dV}{V_i} \alpha, \quad (3.4)$$

with  $C_c$  the chromatic aberration coefficient of the illumination system,  $dV$  the energy spread (in eV) and  $V_i$  the acceleration voltage of the electrons. The diffraction disc  $d_{\text{diffr}}$  is given by

$$d_{\text{diffr}} \approx \frac{\lambda}{2\alpha}, \quad (3.5)$$

with  $\lambda$  the electron wavelength, which can be computed from

$$\lambda = \frac{h}{\sqrt{2m_0e} \sqrt{V_i^*}}, \quad (3.6)$$

where  $h$  is Planck's constant,  $m_0$  is the electron rest mass,  $e$  is the elementary charge, and  $V_i^*$  is the relativistically corrected acceleration voltage, given by

$$V_i^* = V_i \left( 1 + \frac{e}{2m_0c^2} V_i \right). \quad (3.7)$$

### 3. Instrumental Aspects of the Coincidence Experiment

The maximum current  $I_{\text{probe}}$  in this probe is given by

$$I_{\text{probe}} = \frac{1}{4} \pi^2 \alpha^2 d_{\text{geo}}^2 B_r V_i, \quad (3.8)$$

where  $B_r$  is the reduced brightness of the source, a measure for the current that can be extracted from a gun which is independent of the actually applied acceleration voltage.  $B_r$  is expressed as a current which passes a given surface within a solid angle, divided by the acceleration voltage at that surface.

Optimization of a probe forming system is done by maximizing the current in a given total probesize by choosing the appropriate opening angle. A change in opening angle is accompanied by a change of magnification. When both chromatic aberration and diffraction can be disregarded (something which should be checked against Eq. (3.1)) and if  $C_s(M)$  may be replaced with a constant  $C_s$ , the optimization results in

$$I_{\text{probe}} = \frac{3}{16} \pi^2 d_{\text{tot}}^{8/3} C_s^{-2/3} B_r V_i, \quad (3.9)$$

which is found with a half opening angle  $\alpha$  given by

$$\alpha = \sqrt[3]{\frac{d_{\text{tot}}}{C_s}}. \quad (3.10)$$

The approximation that  $C_s(M)$  is constant is only valid in cases where the spherical aberration is dominated by a single lens. For illumination systems which require large demagnifications, the spherical aberration coefficient of the objective lens ( $C_{s_{\text{obj}}}$ ) is usually determining  $C_s$ . For field emitters, which can have very small values of  $d_{\text{gun}}$ , the magnification from gun to specimen may approach unity. Therefore the spherical aberration of the gun lens ( $C_{s_{\text{gun}}}$ ) starts to play a role. A small change in magnification  $M$  may result in a large change of  $C_s(M)$  via  $C_s(M) = C_{s_{\text{obj}}} + M^4 (V_i/V_{\text{gun}})^{3/2} C_{s_{\text{gun}}}$ , with  $V_{\text{gun}}$  the acceleration voltage at the gun lens. It is possible to use this expression in a numerical optimization; see, e.g., Delong *et al.*<sup>1</sup>

However, if the emitter is spherically limited, (i.e.  $d_{\text{gun}} \ll 1/2 C_{s_{\text{gun}}} \alpha_{\text{gun}}^3$ ) an alternative approach is to define an effective brightness  $B_{r_{\text{eff}}}$ :

$$B_{r_{\text{eff}}} = \frac{I_{\text{probe}}}{\frac{\pi^2}{4} \left(\frac{1}{2} C_{s_{\text{gun}}} \alpha_{\text{gun}}^3\right)^2 \alpha_{\text{gun}}^2 V_{\text{gun}}}, \quad (3.11)$$

where  $\alpha_{\text{gun}}$  can be expressed in terms of the angular intensity  $I_{\Omega_{\text{gun}}}$ :

$$I_{\Omega_{\text{gun}}} = \frac{I_{\text{probe}}}{\pi \alpha_{\text{gun}}^2}. \quad (3.12)$$

Substituting this in Eq. (3.11) yields:

$$B_{r_{\text{eff}}} = \frac{16 \pi^2 I_{\Omega_{\text{gun}}}^4}{C_{s_{\text{gun}}}^2 V_{\text{gun}} I_{\text{probe}}^3}. \quad (3.13)$$



Combining Eqs. (3.11) and (3.12) and substituting Eqs. (3.1) and (3.3) leads to an expression of  $I_{\text{probe}}$  in terms of  $\alpha$  which should be optimized. For the spherically limited emitter the probe current is maximized if it satisfies

$$I_{\text{probe}} = \frac{3^{1/4} \pi}{C_s^{1/6} C_{s_{\text{gun}}}^{1/2}} \left( \frac{V_i}{V_{\text{gun}}} \right)^{1/4} I_{\Omega_{\text{gun}}} d_{\text{tot}}^{2/3}, \quad (3.14)$$

while  $\alpha$  again satisfies Eq. (3.10).

Comparing the two optimizations shows that for the spherically limited field emitter, the probe current increases slower with probe diameter ( $d_{\text{tot}}^{2/3}$ ) than for larger thermionic emitters ( $d_{\text{tot}}^{8/3}$ ). This shows that for large probe sizes it is sometimes more profitable to use a thermionic emitter, despite lower brightness values. In case field emitter guns are used for large probe sizes, a careful design of the gun lens is critical.<sup>1</sup> Probes of nanometer dimensions, even for field emission guns which have  $d_{\text{gun}}$  on the order of 10–40 nm, require a demagnification of the gun. Therefore for field emitters the optimization of Eq. (3.14) is valid only at probes of 10–40 nm or larger. For nanometer probes the first optimization (Eq. (3.9)) is more appropriate, again provided diffraction and chromatic effects can be disregarded.

### Wave-Optical Approach

For a field emitter, which has a high brightness, the diffraction may not be disregarded and a wave optical treatment seems more suitable. The wave optical treatment considers all possible trajectories for an electron to travel from the source to the specimen plane. For each emission point of the source, one can integrate the path differences that are experienced over the entire aperture. If expressed in units of the electron wavelength, this yields the wave amplitude in the probe plane. The probability with which the electron of a given wavelength or energy hits a certain point in the probe plane is given by the intensity of these waves. For a monochromatic point source this yields a rotationally symmetric current density distribution; see, e.g. Mory:<sup>2</sup>

$$j_{\text{mono}}(r) = \left| \frac{2\pi}{\lambda} \sqrt{\pi r_0^2 B_r V_i} \int_0^{\alpha_0} e^{i\frac{\pi}{\lambda}(\frac{1}{2}C_s \alpha^4 + \Delta z \alpha^2)} J_0 \left( \frac{2\pi r \alpha}{\lambda} \right) \alpha d\alpha \right|^2, \quad (3.15)$$

where  $\alpha_0$  is the maximum aperture angle,  $r_0$  the demagnified source radius (63% of intensity value),  $\Delta z$  the defocus with respect to the Gaussian image plane and  $J_0(x)$  the zero order Bessel function which results from integration over the azimuthal angle. For example, in the Gaussian image plane, when disregarding spherical aberration, this results in the well known Airy function; see, e.g. Reimer.<sup>3</sup>

To obtain a polychromatic current density distribution one has to add the contributions of electrons of different energy. Since these electrons do not have any phase relation to each other, the intensities (not the amplitudes, cf. Weiss *et al.*<sup>4</sup>) for different energies should be summed, weighted to their occurrence, i.e.

### 3. Instrumental Aspects of the Coincidence Experiment

the energy distribution:<sup>2,3,5,6</sup>

$$j_{\text{poly}}(\mathbf{r}) = \int_{-\infty}^{\infty} j_{\text{mono}}(r, dV) N(dV) d(dV), \quad (3.16)$$

where  $dV$  enters  $j_{\text{mono}}$  via defocus value  $\Delta z = C_c dV/V_i$ .

Different emission points of the source result in a shifted distribution in the probe plane, so that the spatial extent of the source can be incorporated by means of a (two-dimensional) convolution of above found distribution with the intensity distribution  $j_0$  of the source, which can be approximated by a Gaussian:

$$j_{\text{probe}}(\mathbf{r}) = j_{\text{poly}}(\mathbf{r}) \otimes j_0(\mathbf{r}). \quad (3.17)$$

With a practical brightness  $B_r$  of  $1.5 \times 10^7 \text{ Am}^{-2}\Omega^{-1}\text{V}^{-1}$  (Mul *et al.*<sup>7</sup> and Mul<sup>8</sup>), spherical and chromatical aberration coefficients of respectively 2.4 and 6.0 mm for operation at 100 kV (see Bleeker<sup>9</sup>) and optimization toward the 63% fraction of the current in a probe of 1 nm diameter, this yields the current density distribution that is shown in Fig. 3.2. The optimization consists of an iterative

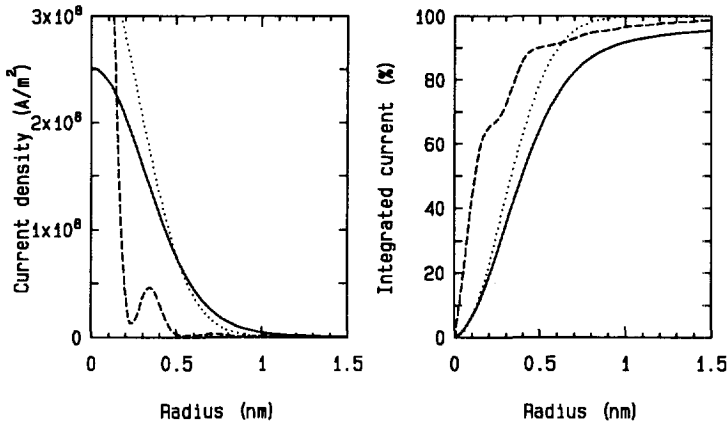


Fig. 3.2: Radial current density distribution and integrated current inside the probe, for a 100 keV field emission gun with a brightness of  $1.5 \times 10^7 \text{ Am}^{-2}\Omega^{-1}\text{V}^{-1}$ , an objective lens with a coefficient of spherical aberration of 2.4 mm and optimized for maximum current, with 63% of this current in a probe of 0.5 nm radius (solid curves). This optimum is reached for an opening angle of 8.8 mrad and a defocus of 185 nm. The magnification of the source should be such that the geometric source image is 0.4 nm (again radius of 63% value of an assumed Gaussian intensity distribution). Also shown are the diffraction limit, including spherical aberration (dashed curves), and the geometric source limit (dotted curves), both with the same total current.

procedure in which both  $r_0$ ,  $\alpha$ , and  $\Delta z$  are varied (based on work performed by

Vroemen<sup>6</sup>). For the found current density distribution the maximum opening angle is 8.8 mrad and the demagnified gun image has a radius of 0.4 nm. A Gaussian energy distribution with a FWHM of 0.6 eV (Mul<sup>8</sup>) is assumed for the computation of the chromatic effect, but it turns out that chromatic aberration for this case is practically of no importance. The optimum distribution is found at a defocus of 185 nm, or  $0.55C_s\alpha^2$ , where  $C_s\alpha^2$  is the extreme defocus in the geometric approximation. According to the wave-optical method the probe contains a current of 0.183 nA. With the squared summation method (Eq. (3.9)) one would find a current of 0.155 nA for the same total probe diameter value. The difference is only on the order of 15 %, but the squared summation method does not predict the relatively large tails which are shown by Fig. 3.2.

### 3.1.2. Acceleration Voltage

The acceleration voltage  $V_i$  or primary beam energy  $E_i$  is an important parameter in the beam specimen interaction. From Eqs. (2.17) and (2.20) one learns that the main influence of the primary beam energy on the scattering cross section is given by  $\gamma^2/k_i^2 \propto 1/\beta^2$ , which in the non-relativistic limit indicates inverse proportionality with  $V_i$ . The other effect of  $V_i$  on the energy differential cross section is based on the narrowing of the scattering distribution, shown by the characteristic scattering angle  $\theta_E = E/(E_i\beta^2)$ . The approximation at low scattering angles of Eq. (2.20) indicates a  $\ln(1+(\theta_{\max}/\theta_E)^2)$  behavior. The combined effect can be seen in Fig. 3.3a, where the energy differential cross section for carbon and aluminum  $K$ -shell excitation is divided by the photo absorption cross section. Taking this ratio brings the curves for the two species closer together and further allows direct comparison with Fig. 2.14a. The acceptance angle has a rather important influence on the shape of the graphs. Fig. 3.3b shows the effect when the  $(q, E)$ -dependence of the generalized oscillator strength is also included.

With respect to specimen thickness the acceleration voltage is also an important parameter. The faster an electron travels, the less chance per unit length it has to undergo scattering on the atoms in the specimen. This is equivalent to the decrease in cross section shown above, in this case irrespective of scattering angle, and thus corresponding to large acceptance angle computation. Besides for inelastic scattering this behavior is also present for elastic scattering. The mean free path lengths  $\lambda_{\text{inel}}$  and  $\lambda_{\text{el}}$  associated with these scattering processes, increase with acceleration voltage.

The most important effect of a larger mean free path is a decreasing probability of multiple scattering. Multiple scattering leads to total energy losses that are the sum of several different losses. Assuming that for small relative energy losses the cross sections in subsequent scattering processes all yield the same spectral form, the resulting spectrum will be a self-convoluted form of a single scattering spectrum. So for a fixed specimen thickness this means that the energy-loss and related spectra will have an easier interpretation for higher acceleration voltages. On the other hand for energy-loss spectroscopy with a certain acceptable amount

### 3. Instrumental Aspects of the Coincidence Experiment

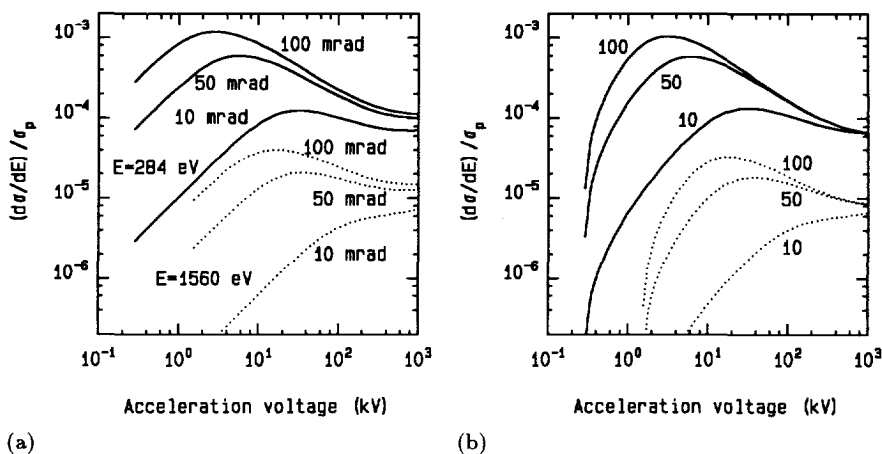


Fig. 3.3: (a) Ratio between energy differential cross section  $d\sigma(E)/dE$  and photoabsorption cross section  $\sigma_p$  as a function of acceleration voltage, (a) computed according to Eq. (2.20) and (b) computed using SIGMAK2 program.<sup>10</sup> Solid lines represent an energy loss just above the carbon  $K$ -edge (at 284 eV), dotted lines represent the aluminum  $K$ -edge (at 1560 eV). For each energy loss, acceptance angle values of 10, 50, and 100 mrad are used.

of multiple scattering, increasing the acceleration voltage yields the possible use of thicker specimens. It is possible to apply (self-) deconvolution techniques to energy-loss spectra partly obscured by multiple scattering, but doing this is complicated and often yields a loss in statistics and or energy resolution.<sup>11</sup> Deconvolution of multiple scattering effects in coincidence spectroscopy is expected to be handled in a similar way, in such a sense that the low-energy region of the normal EELS spectrum is used, rather than the low-energy region of the coincidence spectrum itself.

As will be shown in 3.2 an increased acceleration voltage leads to decreased dispersion of electrons of different energy over the detector. For a given absolute energy resolution this is accompanied by a reduction of acceptance angle, shown in Fig 3.6.

In 3.1.1 it was shown that the available current increases linear with  $V_i$ , at least for small probe sizes (Eqs.(3.9) and (3.15)). The overall picture for the acceleration voltage will thus be formed by a combination of above mentioned effects. In Fig. 3.4 the energy differential cross section is shown, multiplied with the acceleration voltage. It is computed for the acceptance angle that is possible at 1 eV energy resolution, with and without (chromatic) focus correction, using the magnetic energy loss analyzer discussed in 3.2. From this graph it follows that maximum EELS signal strength is reached at the highest possible acceleration voltage.

For the coincidence technique, the effect on the emitted electron should also be

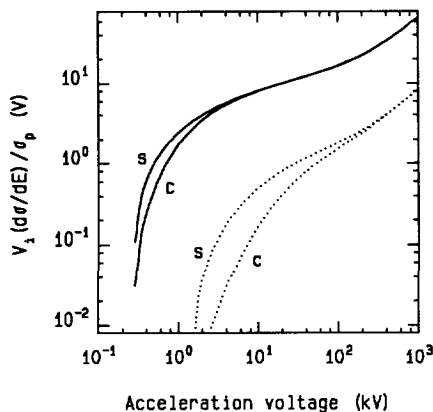


Fig. 3.4: EELS signal strength, expressed as a ratio between energy differential cross section  $d\sigma(E)/dE$  and photoabsorption cross section  $\sigma_p$ , multiplied with acceleration voltage  $V_i$ , as a function of  $V_i$ . Along the graphs the acceptance angle is varied as in Fig. 3.6, yielding a spherically (s) and a chromatically (c) limited graph. Solid lines represent an energy loss just above the carbon  $K$ -edge (at 284 eV), dotted lines represent the aluminum  $K$ -edge (at 1560 eV).

included. The operation of the collection optics for the emitted electrons is almost independent of the acceleration voltage (see 3.3). With higher acceleration voltage the emitted electron distribution is somewhat pushed forward (see 2.2.2). Emitted electron detection from the exit side therefore favors increasing the acceleration voltage, whereas detection from the entrance side will be somewhat weaker. With low mean free path for the elastic scattering of the emitted electrons, the distribution tends to become completely homogeneous. In that case, maximum signal strength for the coincidence technique matches exactly with that for the EELS technique.

### 3.1.3. Energy Spread

The energy spread of the primary beam places a lower bound on the energy resolution of the EELS technique, and with it for example also on the virtual-photo electron spectroscopy technique. If the energy spread function is well known, or shows a relatively sharp feature, deconvolution techniques might improve a little bit on the resolution; see, e.g., Batson.<sup>12</sup> As was shown in 3.1.1 the energy spread may also influence the obtainable probe size or current. For the example nanoprobe discussed there, the chromatic aberration associated with primary beam energy spread hardly influenced the probe formation qualities.

In a STEM several electron sources can be applied. The standard tungsten hairpin thermal emitter has an energy spread on the order of 1 eV. The about 10 times brighter lanthanum hexa boride ( $LaB_6$ ) emitter has a similar energy spread.

### 3. Instrumental Aspects of the Coincidence Experiment

A cold field emission gun which delivers a lower total current has a much lower energy spread on the order of 0.3 eV. The thermal or Schottky field emission gun is about two orders of magnitude better in terms of deliverable current but this at the cost of a somewhat worse energy spread of 0.4 to 0.8 eV, depending on the extracted current; see, e.g., Mul *et al.*<sup>7</sup> These values are however still considerably better than the value for the  $LaB_6$  emitter.

If lower values for primary beam energy spread are required the beam must be filtered. For high-resolution electron energy-loss measurements (but not in a STEM) this has been done with success for example by Fink.<sup>13</sup> Primary beam filtering is always accompanied by a loss in total current.

In regular EELS operation, aimed at elemental analysis (separating and quantifying different edges), energy resolution below values of 1 eV is not required. For the virtual-photo electron spectroscopy technique, which in principle is capable of showing chemical shifts, an improvement in energy resolution toward a few tenths of eV can be of more importance. Combined with the fact that the energy resolution at these values does not yet seriously deteriorate the probe formation, it can be stated that energy resolution is not a very important criterium to choose an electron source. The choice of a high brightness source like the Schottky field emission gun, with the possibility to reduce the brightness in favor of the energy spread seems advisable.

#### 3.1.4. Probe Current

The probe current  $I_{\text{probe}}$  is directly related to the amount of scattering events that take place in the sample. Probe current is therefore linearly related to the (non-coincident and true-coincident) signal strength and signal rates. For strong signals therefore probe current should be high. As will be shown in 3.5 this is limited at some point by a stronger increase in the false-coincidence countrate, which is proportional to  $I_{\text{probe}}^2$ . An obvious criterium which limits probe currents on the low side is acquisition time. From 3.1.1 it is clear that for a given brightness, an increase in probe current is only possible at the cost of spatial resolution and an increased opening angle.

#### 3.1.5. Probe Size

The size of the probe determines a lower bound on the spatial resolution. In 2.1.3 it was shown that for a 1 nm diameter probe this value actually can determine the spatial resolution itself. The probe size therefore determines the amount of atoms that are studied. If one tries to study small (absolute) amounts of atoms, the probe size should be as small as possible. For quantification of small concentrations of a certain species, one will need a large amount of these atoms to be present in the probe, which asks for large probe sizes.

### 3.1.6. Illumination Opening Angle

The opening angle, which specifies the range of angles with which the primary electrons can hit the sample, places a lower bound on the angular resolution for the EELS measurement. If the opening angle approaches the acceptance angle of the EELS detector, a loss of transmission will occur for those events generated by the electrons with large inclination angle. The momentum resolution will also be reduced since this is based on accurate measurement of the scattering angles. For these reasons one should aim for a small illumination opening angle. The only limitation is given by remaining probe current and deterioration of spatial resolution.

### 3.1.7. Non-Rotationally Symmetric Aberrations

Above considerations are for perfectly axial symmetric systems. Due to mechanical imperfections of lenses and apertures or misalignments of the optical column the axial symmetry can disappear. Fortunately in a TEM the probe shape can be visualized on the TEM viewing screen or measured by cameras below this screen. Several methods exist to check and correct the post-specimen imaging part of a TEM.<sup>14</sup> Any remaining misalignment effects like coma can then be attributed to the probe forming part. When any unroundness or astigmatism occurs the spot or the current density distribution inside it, will be of different shape and it will always lead to a reduced resolution. Astigmatism in STEMs is however a well-known problem and is suitably solved for probe forming systems by placing compensating unround optical elements or stigmators, somewhere in the optical path.

Higher order (e.g., three-fold) astigmatism requires higher order multipoles to nullify the effect of it. These multipoles (e.g., twelve-poles) are not standardly available in most present day STEMs, but will most likely become of importance in a setup where a 90° deflector is used to separate the secondary electrons from the primary beam. The deflector is expected to cause some extra three-fold astigmatism.

### 3.1.8. Instabilities

To be able to position the electron beam on different parts of the specimen the STEM has a scanning system equipped with a double set of deflectors, of which the pivot-point is adjusted to give minimum deflection aberrations. Noise in the deflector signals can cause an unwanted probe movement, especially if the scanning system is capable of large area scans. During scanning the electrical supplies for the deflectors must be bandwidth limited, just allowing the scan signal to pass through. Compared to a still probe the electrical noise in the deflection signal will then be larger. The movement of the source image can also be seen as a decrease of the (apparent) brightness of the gun during scanning, which becomes important when the source image movements are comparable in size to the source image. The above mentioned value of the reduced brightness ( $1.5 \times 10^7 \text{ Am}^{-2}\Omega^{-1}$ ) was

### 3. Instrumental Aspects of the Coincidence Experiment

obtained with a bandwidth suitable for normal scanning operation (Mul<sup>8</sup>) and a probe size of 5 nm. For smaller probes we may expect to realize this same value, if necessary with a somewhat smaller bandwidth.

Fluctuating (external) magnetic fields in the neighborhood of the electron gun also give rise to a reduction of the apparent brightness. Due to the demagnification of the source, which follows the required size of the probe, the effect of these fields is a constant decrease in brightness. Proper mu-metal shielding is necessary to minimize these influences.

A final cause for instabilities is drift of the analyzed part of the specimen with respect to the probe position. Heat leakage from the objective lens coils can cause thermal instabilities of the specimen environment. Mechanical drift of the specimen holder with respect to the objective lens pole pieces (which determine the position of the optical axis and therefore of the probe) amounts to values on the order of 1 nm/min. Electron beam induced localized heating and stress can cause the specimen area analyzed to move with respect to the specimen holder. Only certain specimens will prove to be capable of withstanding the electron bombardment. Displacements of both types are difficult to predict or to measure in a probe forming system. By regularly taking a standard TEM or STEM image of the specimen area, displacements can be measured and likewise be compensated, but the requirement of changing imaging conditions to perform such measurements is likely to cause more problems than it solves. Depending on the required measurement times, attention should be paid to the mechanical construction of the specimen holder and the thermal conditions during and also before the measurement.

#### 3.1.9. Conclusions on Probe Formation

For the purpose of high-spatial-resolution, elemental and chemical analysis of surfaces, a high acceleration voltage is favorable. The measurements should be performed with a high brightness electron source. For this purpose, a Schottky field emission gun is the best choice. A high voltage instrument like a TEM /STEM combines high quality probe forming capabilities with flexibility. Good energy resolution, small probe size, small illumination angle, and (relatively) large currents can be combined in this instrument.

## 3.2. Energy-Loss Measurement

Good transmission characteristics from specimen to detector are essential for coincidence spectroscopy. The electron-optical description of this transmission problem is not significantly different from that of normal EELS spectroscopy.

The energy-loss measurement requires good electron-optical matching of the specimen with the energy dispersing element and the detector. The first of these is dealt with by *pre-spectrometer optics*, the second by *post-spectrometer optics*. Pre- and post-spectrometer optics as well as the spectrometer itself will contribute aberrations which degrade performance. In a dedicated STEM almost no



pre-spectrometer optics is available. For example, the only element in a VG HB5 dedicated STEM that belongs to the pre-spectrometer optics section is the post-specimen objective-lens field.<sup>10</sup> The post-spectrometer section often is nothing more than a drift space, which in fact could also be regarded as part of the spectrometer. Real post-spectrometer optics becomes necessary when the dispersion of the spectrometer is not well-matched with the detector. This is especially the case for parallel detectors.

For the energy-loss measurement the different parts of the electron optics will now be discussed, followed by a treatment on the relation between acceptance and energy resolution. The EELS detector itself will be discussed in 3.4.

### 3.2.1. Pre-Spectrometer Optics

In general, the function of the pre-spectrometer optics is to match the source of the energy-loss electrons, the illuminated part of the specimen, as good as possible to the spectrometer object plane. Best matching at a certain energy resolution is achieved if the largest possible angular fraction of the scattered electrons is accepted by the spectrometer. This requires a good choice of magnification or diffraction length setting, depending if one uses image coupling or diffraction coupling. As was discussed by Kruit and Shuman,<sup>15</sup> aberrations of the pre-spectrometer optics (mainly the post-specimen objective lens field), in combination with spectrometer aberrations, will degrade the angular acceptance or the energy resolution for both modes of operation.

In *image coupling mode* the specimen is imaged on the object plane of the spectrometer, with some magnification  $M$ . The diffraction plane coincides with the angle limiting aperture for the spectrometer, which comes just below the removable TEM viewing screen. If the spot on the specimen is very small, in the nanometer range, one can select a fairly large magnification  $M$  before the image of the spot starts to degrade the energy resolution. This is then accompanied by a large angular demagnification which for a fixed spectrometer angle-limiting aperture (and accompanying energy resolution), enables large effective collection angles at the specimen level. The energy spectrum is convoluted with the current distribution in the probe.

In *diffraction coupling mode* the diffraction plane is imaged with some effective camerlength on the spectrometer object plane. The specimen is imaged on the spectrometer angle-defining aperture (or the microscope viewing screen). The aperture selects the area of the specimen that is analyzed, and should be matched with the probe size. The diffraction plane should be apertured to some effective acceptance angle to limit the spectrometer object size. The energy spectrum is convoluted with the distribution in the diffraction plane.

### 3.2.2. Spectrometer Optics

The spectrometer focuses the electrons from the spectrometer object plane to its complementary image plane, while dispersing electrons of different energy. The

action of the spectrometer is thus characterized by a magnification  $M_s$  and a dispersion  $dx/dE$ . For a  $90^\circ$  magnetic sector spectrometer the main remaining aberration after compensation of the second-order opening-angle aberration is the third-order opening-angle aberration.<sup>15</sup> In case of parallel detection another difficulty can be found in the inclination angle of the image plane, as discussed by Egerton.<sup>10</sup> This does not have to be too serious since the depth of field is quite large due to a large angular demagnification.

### 3.2.3. Post-Spectrometer Optics

The function of post-spectrometer optics is to take care that the spectrum, which is unravelled by the spectrometer, can be resolved by the detector. Without such optics, the dispersion  $dx/dE$  times the required energy resolution  $\Delta E$  gives the maximum size of the detector element(s). Post-spectrometer optics can provide extra magnification (or demagnification) to match dispersion and energy resolution with the employed detector. For a normal (serial) detector that works with an adjustable slit to define the detector size (see 3.4.2), post-spectrometer optics is not necessary. Parallel detectors however usually have larger detector elements which cannot be adjusted. They may therefore benefit from post-spectrometer optics.

To prevent problems of image rotation, a post-spectrometer system cannot be based on ordinary magnetic round lenses. Existing systems are either based on special non-rotating lens pairs,<sup>16</sup> or on one or more quadrupoles.<sup>17,18</sup>

### 3.2.4. Energy Resolution Versus Acceptance Angle

To find the obtainable energy resolution as a function of acceptance angle, we make use of some relations by Kruit and Shuman.<sup>15</sup> The best possible energy resolution  $\Delta E$  with a magnetic sector spectrometer which is limited by third order aberration (with coefficient  $A_3$ ) is given by

$$\Delta E = 1.32 \frac{1}{dx/dE} (M_s^3 A_3 \alpha^3 d^3)^{1/4} \quad (3.18)$$

where  $dx/dE$  is the dispersion of the spectrometer,  $M_s$  is the spectrometer magnification and  $d$  is the effective probe size, including pre-spectrometer-lens aberrations, defined by

$$d^2 = d_p^2 + (C_s \alpha^3)^2 + (C_c \frac{E}{eV_i} \alpha)^2 \quad (3.19)$$

where  $C_s$  and  $C_c$  are the coefficients of spherical and chromatic aberration of the pre-spectrometer lens system. To good approximation these coefficients are determined by the post-specimen section of the objective lens. Both  $d$  and  $\alpha$  are defined at the level of the specimen. Figure 3.5 shows that in practical situations with nanometer probes the geometric contribution to the energy resolution is of no importance compared to chromatic and spherical contributions. In case of serial

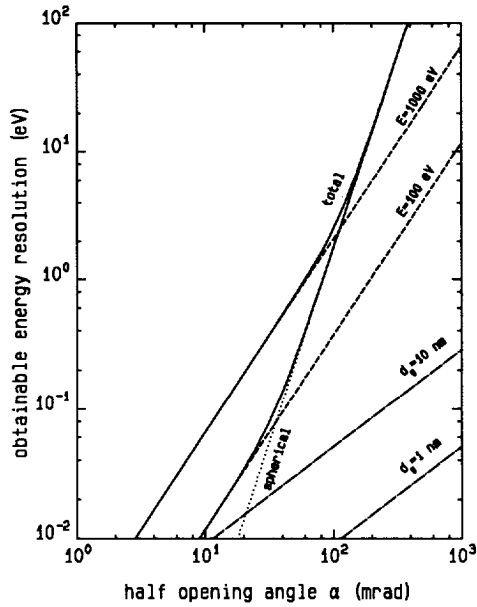


Fig. 3.5: Best possible EELS resolution  $\Delta E$  at 100 kV acceleration voltage as a function of acceptance angle  $\alpha$  for a second-order corrected spectrometer. Spectrometer coefficient of third order aberrations  $A_3=1.5$  m, post specimen objective lens coefficients of spherical and chromatic aberration are 1.1 and 1.4 mm respectively.<sup>9</sup> Graphs are shown for spherical contribution (dotted), chromatical contribution at 100 and 1000 eV 'defocus' (dashed), for geometrical contribution at 1 and 10 nm probesize (dash-dot) and for total effect (solid), with probesize of 1 nm and chromatic contributions of 100 and 1000 eV energy loss.

spectrum acquisition the chromatic aberration term can in principle be suitably corrected by refocusing of the spectrometer optics; see, e.g., Krivanek *et al.*<sup>19</sup> For parallel spectrum acquisition the chromatic term will be different for different parts of the spectrum, unless a compensation for this effect has been applied. Such a compensation could in principle be given by a suitable tilt of the detector plane. However, one needs to match the width of the detector elements with the virtual (post-specimen) spherical aberration limited probesize. At acceptable energy resolution and for practical parallel detector dimensions the required magnification from specimen to detector is so large that chromatic defocus values are often much larger than the detector size, yielding unacceptable tilt values. A parallel detector which is focussed for some energy which falls in the detector range (normally the center), will still show the effect of chromatic aberration at the edges. For a fixed amount of detector elements (on the order of 100), with the magnification tuned to resolve the optimum resolution in the center, the resolution at the edges will be

### 3. Instrumental Aspects of the Coincidence Experiment

just slightly worse than given by the spherical limitation, unless the resolution in the center is already above 10 eV.

From Fig. 3.5 we see that for 1 eV resolution, in a spherically limited situation, 100% collection efficiency is possible for acceptance angles up to about 80 mrad. Without refocussing, and for 1-keV losses this is possible up to about 60 mrad. In the spherical limit the maximum acceptable opening angle for a given energy loss is proportional to  $A_3^{1/12}$ , see Eqs. (3.18) and (3.19). This makes the maximum acceptance angle quite insensitive to the actual value of  $A_3$ , which depends somewhat on mechanical alignment of the spectrometer.

From Eq. 3.18 we see that the acceptance angle only depends on the acceleration voltage via the dispersion. For a magnetic-sector spectrometer  $dx/dE$  is given by:

$$\frac{dx}{dE} = \frac{R^*}{eV_i} \left( \frac{eV_i + m_0c^2}{eV_i + 2m_0c^2} \right), \quad (3.20)$$

where  $R^*$  is a geometrical spectrometer constant,<sup>20</sup> which may be found by substitution of the dispersion figure of  $1.8 \mu\text{m}/\text{eV}$  at 100 keV. For non-relativistic energies the acceptance angle then becomes proportional to  $V_i^{-1/3}$  in the spherical limit and proportional to  $V_i^{-1/6}$  in the chromatical limit. The influence of acceleration voltage on the acceptance angle is shown in Fig. 3.6. In this figure the

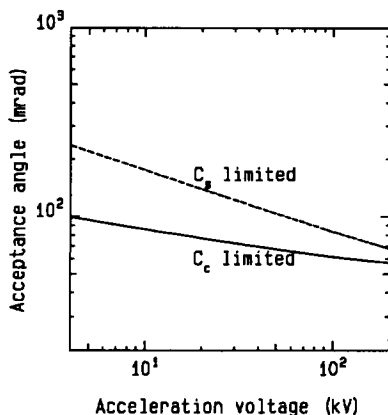


Fig. 3.6: Acceptance angle at fixed energy resolution of 1 eV as a function of acceleration voltage, in spherical and chromatical aberration limited cases. The chromatical aberration is computed for a 1-keV energy loss. All coefficients are chosen similar to those of Fig 3.5.

energy resolution is fixed at 1 eV, while all other parameters have the same value as for Fig. 3.5. The energy loss used for the chromatically limited case is 1 keV. The dispersion favors small acceleration voltages, but does this at the cost of a decreased energy range which can pass the spectrometer.

Although in practice the acceptance angle is fixed by some (chosen) aperture, it is possible to use the acceptance angle values of Fig. 3.6 as limits for the integration of Eq. (2.17). This is done in 3.1.2, resulting in Fig. 3.4.

### 3.3. Emitted-Electron Measurement

The secondary-electron measurement shows some general resemblance to the EELS measurement in the sense that it also requires the electron optical matching of the emitted electrons to the detector. Again we can speak about pre- and post-spectrometer optics. The pre-spectrometer optics consists of the parallelizer and a transfer optics system, consisting of a  $90^\circ$  deflector and an electrostatic lens system. The spectrometer is a  $180^\circ$  concentric hemispherical analyzer (CHA). The post-spectrometer optics will only be discussed briefly, since for the present experiments it does not actually exist of optical elements: the detector is put directly at the end of the spectrometer. The main difference with the EELS measurement will be the non-trivial behavior of the parallelizer and the different energy range involved.

The low-energy secondary electrons have energies below 50 eV and maybe, depending on the definition, some tail extending above it. Auger electrons can have energies up to a few keV, but we will concentrate on the electrons below 2 keV, mainly because at higher energies x-ray emission becomes the favorable decay process. At these lower energies an electrostatic spectrometer and accompanying de- or acceleration lenses becomes a suitable alternative for the magnetic one.

Below the different parts of the electron optical system for the emitted electrons will be discussed. Special emphasis is put on different modes of operation of the transfer optics and spectrometer. Operation of the spectrometer at constant pass energy ( $U_p=100$  eV), and for a single detector set-up, has already been discussed by Bleeker.<sup>9</sup> Kruit and Venables<sup>21</sup> also suggested operation at a pass energy  $U_p = U_i/2$ , with  $U_i$  the initial kinetic energy of the emitted electrons. Although both ways of operation promise good performance of the parallelizer-analyzer combination, the many system parameters allow for other modes of operation. Several optimizations are done for a parallel detector system, in terms of transmission, energy resolution and timing accuracy.

#### 3.3.1. Parallelizer

The specimen in the STEM is situated in the high magnetic field of the objective lens. Electrons released from the specimen in the scattering event will start spiraling around the magnetic field lines. Normally these fieldlines would lead the electrons to the magnetic material of the objective lens where they would be lost. In order to collect the electrons a special magnetic field form is created which is called the parallelizer. This gradually decreasing field forces the electrons to move to the low field region. In the low field they move much more parallel to the optical axis and they are guided through a magnetic aperture that ends the field. The

### 3. Instrumental Aspects of the Coincidence Experiment

principle of the magnetic parallelizer is discussed in detail by Kruit<sup>22</sup> and Bleeker and Kruit.<sup>23</sup>

There are two important parameters for the optimization of the matching of the electrons to the detector. One parameter is the maximum diameter the electrons can reach at the end of the parallelizer when they start on axis in the high-field region. In the adiabatic approximation which is valid for the slowly varying magnetic field of the parallelizer,<sup>9</sup> the radius in the final field  $r_f$  is given by

$$r_f = r_i \sqrt{\frac{B_i}{B_f}}, \quad (3.21)$$

where  $r_i$  is the cyclotron radius in the initial field  $B_i$ , given by

$$r_i = \sqrt{\frac{2mU_i \sin \alpha_i}{e^2 B_i}}, \quad (3.22)$$

with  $\alpha_i$  the initial angle with the optical axis and  $U_i$  the kinetic energy of the electron. The maximum diameter at the end of the parallelizer, which we will denote by  $d_s$  ( $s$  stands for source for the pre-spectrometer optics), is reached for  $\alpha_i = \pi/2$ :

$$d_s = 4 \sqrt{\frac{2mU_i}{e^2}} \sqrt{\frac{1}{B_i B_f}}. \quad (3.23)$$

The other parameter we need to know about the parallelizer is the maximum angle with which the electrons come out. The angle with which the electrons leave the parallelizer (if they would cross the axis at that point) is given by the relation

$$\sin \alpha_f = \sin \alpha_i \sqrt{\frac{B_f}{B_i}}, \quad (3.24)$$

which for small ratios of  $B_f/B_i$  is also a good approximation for  $\alpha_f$ . The maximum angle  $\alpha_s$  (for  $\alpha_i = \pi/2$ ) is then:

$$\alpha_s = \sqrt{\frac{B_f}{B_i}}. \quad (3.25)$$

As is explained in detail by Bleeker,<sup>9</sup> the combination of both maximum angle and maximum diameter do not occur simultaneously, but they form a good though somewhat pessimistic characterization of the parallelizer. In so-called phase space all electrons are described by a distance they have from the optical axis and an angle with this axis. The rectangular area in phase space which encloses the somewhat elliptical area that is actually occupied by electrons leaving the parallelizer, is used to characterize the transfer optics:

$$\alpha_s d_s = C \sqrt{U_i}, \quad (3.26)$$

with

$$C = 4\sqrt{\frac{2m}{e^2 B_i^2}}. \quad (3.27)$$

This way we assume that electrons have equal probability to have performed any number of rotations in the parallelizer field. A more thorough characterization should take into account the current density distribution in phase space. Bleeker<sup>9</sup> has shown that the concentration of electrons as a function of the distance to the axis is a complicated function with many sharply peaked steps caused by periodic focusing inside the parallelizer. For a more accurate current density distribution in phase space and the effect of cutting off several parts of this distribution, the non-uniform angular distribution of the electrons at emission from the sample should be taken into account.

### Timing Accuracy

The complex trajectories inside the parallelizer are likely to raise questions on timing accuracy. However, after a short distance in the parallelizer all trajectories become almost parallel to the axis. Kruit and Read<sup>24</sup> have shown by numerical raytracing techniques that the relative flight-time spread  $\Delta t/t$  due to differences of initial emission angle in the high field of the parallelizer, stays below 1% for several initial angular distributions. The flight time for an on-axis electron over the length of the parallelizer ( $l$ ) is given by

$$t = \frac{l\sqrt{2m}}{2} U_i^{-1/2}, \quad (3.28)$$

which for  $l=100$  mm indicates that

$$\Delta t < 1.68 \text{ nsec} (U_i/e)^{-1/2}. \quad (3.29)$$

This value is small compared to the spectrometer contributions, see Sect. 3.3.3.

#### 3.3.2. Transfer Optics

The transfer optics consists of a 90° deflector, just above the end of the parallelizer, and a system of electrostatic lenses. The properties of the 90° deflector are discussed by Bleeker.<sup>9</sup> In its ideal form the deflector consists of a crossed magnetic and electrostatic field, which enables achromatic deflection for a large range of energies. The deflector settings therefore do not have to be scanned while acquiring an emitted-electron energy spectrum. As a consequence the primary beam will also be undisturbed during spectrum acquisition. For the present case, the deflector can be treated as part of a larger transfer optics lens system, due to the double focussing action of the deflection field.

The matching of the virtual source, as it is formed by the parallelizer, to the entrance of the (electrostatic) spectrometer (see Fig. 3.7) is governed by the prin-

### 3. Instrumental Aspects of the Coincidence Experiment

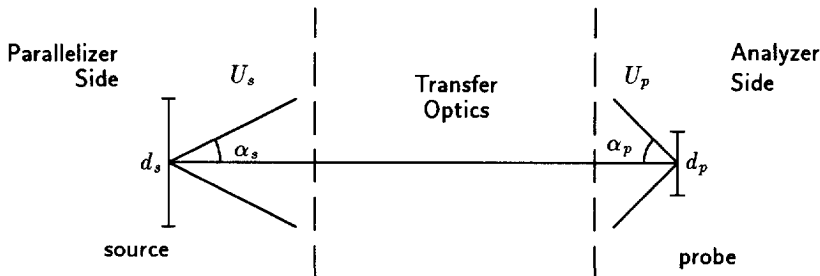


Fig. 3.7: Schematic transfer optics between parallelizer and 180° analyzer.

principle of Liouville, the constancy of the product of the sine of opening angle (or for small angles the opening angle), probe diameter and the square root of the kinetic energy:

$$d_p \alpha_p \sqrt{U_p} = d_s \alpha_s \sqrt{U_s}. \quad (3.30)$$

If we assume no electrostatic acceleration or deceleration between the sample and the (virtual) source, we can replace  $U_s$  directly by  $U_i$ , the initial kinetic energy. Aberrations of the transfer optics will effectively enlarge the left-hand side of above equation to some extent. The values of  $d_p$  and  $\alpha_p$  that can be accepted will be limited by the dimensions of the spectrometer.

The free parameters in this system are the magnification  $M$  defined by:

$$|M| = \frac{d_p}{d_s}, \quad (3.31)$$

and the kinetic energy inside the spectrometer  $U_p$ . The choice of  $U_p$  depends on the spectrometer optics, for example on energy resolution and number of detector channels. High-voltage insulation may also impose practical limits on the value of  $U_p$ . If because of that (3.30) cannot be met, this finds expression in reduced energy resolution or transmission.

The transmission will be defined as the actual accepted area in phase space divided by the original phase space area of Eq. (3.26), corrected for changes in kinetic energy according to Eq. (3.30):

$$T = \frac{\alpha_{acc} d_{acc}}{\alpha_p d_p}, \quad (3.32)$$

where  $\alpha_{acc}$  and  $d_{acc}$  are the accepted opening angle and diameter of the beam in the analyzer. By this definition we assume that in the direction perpendicular to the dispersion there are no limitations. The definition can only give a good measure for the actual current transmitted by the system if the current is homogeneously distributed over phase space. By using this definition for a non-homogeneously



filled phase space, as it is formed by the parallelizer, we can only see the transmission figure as a measure for the area of the phase space and not so much as a percentage of current that comes through.

To operate the system there are several alternative options, which all share some common considerations. First of all we assume that we want to accumulate a spectrum for as many channels as possible during a minimum of time, where the number of counts in each channel should satisfy certain statistical requirements. If we can assume a homogeneously-filled phase space this indicates the need to optimize the product of transmission and the number of channels. Furthermore one would prefer not to have to adjust mechanical slits while scanning. Depending on the implementation there can also be limitations on the optical system and the way variations in this system can be realized. For example, complex non-linear variations of lens excitations can require some (semi-) computerized control. Above that, some settings (for example the spectrometer setting itself) might be very critical, and one could opt to keep these fixed at their set values.

Depending on the situation one would like to have either optimum energy resolution or the largest possible range at a fixed resolution. As will be shown the optimum energy resolution as well as the energy range depend on the position in the spectrum.

Because of the uncertainties about the filling of phase space there is something to say for the wish for 100% transmission. This means that no slits near the optical axis are required. Only than one can be sure not to throw away any essential part of the original angular distribution. Furthermore no direct effects of the periodic-focusing steps in the current density distribution show up in the spectrum. Unfortunately effects of periodic focusing will show up in the form of periodic energy resolution variations.

Alternatively we could opt for less than 100% transmission, especially if we are not too concerned with the angular distribution, but mainly with intensity. If the intensity is somewhat concentrated in the center of phase space, we can expect that cutting off some of the outer area of this phase space, will degrade intensity to a smaller extent than the gain in channels or resolution that can be realized as a result of a reduced transmission. For this option the periodic focusing will have a direct effect on the intensity as a result of cutting-off some of the current distribution as well as via the energy-resolution variations. The different operation modes will be discussed in 3.3.4, after a discussion of the spectrometer optics.

### **Aberrations of the transfer optics**

Independent of the actual mode of operation one should consider the effects of electron optical aberrations. The most important aberrations will be spherical and chromatical aberration. Off-axial aberrations such as distortion and curvature of field may also be of some importance, due to the relatively large diameter of the beam in the system, but their effect will not be discussed here. In principle they seem to act on performance in a way similar to spherical aberration.

### 3. Instrumental Aspects of the Coincidence Experiment

Spherical aberration causes a blurring of the edges of the spot at the spectrometer entrance plane, which effectively enlarges the spot. The performance in terms of transmission, energy resolution and/or energy range will be diminished to some extent.

Chromatical aberration is normally also treated as causing a larger spotsize, but we need to look into this a little deeper. If we aim for a certain energy resolution, we could indeed take the relative energy resolution, multiply this with the opening angle and get a measure for the size of the enlargement of the spot. By doing this we implicitly assume that the transfer optics is focussed on the entrance plane of the spectrometer for only one energy. For electrons of different energy the focus will be in front or after this plane. For the detection at the ends of a parallel detector this means that half the energy range should be used in the computation of the chromatical aberration. Or in different words, at both ends of the parallel detected spectrum the transmission is decreased (when slits are present). Without slits the energy resolution will be worse at the ends (due to defocusing). At large energy ranges the effect of chromatic aberration may not be discarded and care must be exerted to minimize this aberration.

Since the transfer optics should be operated over a large range of energies, the design of the transfer optics will not be trivial. Combined with changing demands on the magnification this could require a complex behavior of the lens voltage settings as a function of the analyzed energy. Electron optical optimization programs such as described by van der Steen, Barth and Adriaanse<sup>25</sup> have proved to be an important tool in the optical design.<sup>26</sup>

#### Timing Accuracy

For a straight section of transfer optics, of length  $l$ , flight time differences may be caused by differences in electron energy  $U$  and by different angles  $\alpha$  with the optical axis. The effect of a range of different energies  $\Delta U$  yields a time accuracy

$$\Delta t = -\frac{l\sqrt{2m}}{4}U^{-3/2}\Delta U, \quad (3.33)$$

which, for a (constant) pass energy of  $U=100$  eV, a resolution of  $\Delta U=1$  eV and for a length of 400 mm (that is including the parallelizer) gives a small 0.3 nsec time accuracy. As will be shown later, Eqs. (3.46) and (3.49), the obtainable energy resolution is proportional to  $U_i^2$ , so that the time accuracy due to the finite width of the energy band becomes proportional to  $U_i^2/U^{3/2}$ .

For electrons which have an opening angle  $\alpha$  with the optical axis, the relative time accuracy becomes

$$\frac{\Delta t}{t} = \frac{1}{2} \sin^2(\alpha) \frac{U_i}{U}, \quad (3.34)$$

where we have used Eq. (3.30). Since the parallelizer reduces initial emission angles  $\alpha_i$  to the value of Eq.(3.25), which is of the order of 0.1 rad, this means that the

relative time accuracy stays below  $0.5\% U_i/U$ . For a total length of 400 mm this gives a time accuracy

$$\Delta t = 3.4 \text{ nsec} \frac{(U_i/e)^{1/2}}{U/e}. \quad (3.35)$$

In strong decelerating lenses  $U$  may be of the order of  $0.1 U_i$ . Therefore, for detection of low-energy electrons, one should avoid long strongly decelerating lens sections.

### 3.3.3. Spectrometer Optics

The spectrometer discussed here is of the concentric hemispherical analyzer type. The dispersion of a  $180^\circ$  analyzer is given by  $\Delta x/\Delta U = 2R/U_p$ , where  $\Delta x$  is a displacement in the radial direction due to an energy difference  $\Delta U$ , with respect to electrons of energy  $U_p$  which follow the central radius  $R$ . The energy resolution of the spectrometer is mainly governed by the dispersion, the size of the probe at the entrance of the analyzer and the second-order angular aberration. The size of the detector or the width of the channels in the detector determines how well this energy resolution is preserved. Imhof *et al.*<sup>27</sup> have found an expression for the energy resolution, valid for a homogeneously illuminated entrance slit of width  $\Delta d$ , with an opening angle for each point of this slit ranging from  $-\alpha_{\max}$  to  $+\alpha_{\max}$ :

$$\frac{\Delta U}{U_p} = k_1 \Delta d + k_2 \alpha_{\max}^2, \quad (3.36)$$

where  $k_1 = 0.43/R$  and  $k_2 = 0.25$ . The relative size of the first term in relation to the second term will be denoted by  $k_3$ . A different choice of  $k_3$  just means a little change of the shape of the final function with which the original emitted-electron energy distribution will be convoluted.

We will suppose the detector length is limited to some value  $d_a$ . Similarly the maximum angle for  $\alpha_p$  in the analyzer is limited to  $\alpha_a$ . For both values the limitation primarily comes from the restricted space between the inner and outer sphere of the analyzer.

In the plane perpendicular to the dispersion plane we will assume that no obstructions limit the beam size or opening angle. The aberrations in this plane will be disregarded for the discussion on different operating modes (in 3.3.4).

### Timing Accuracy

One of the aspects of the spectrometer optics, of specific concern to coincidence spectroscopy, is timing accuracy. Depending on the flight path inside the analyzer different travel times will be experienced by the electrons. Expressions for the dispersion of the transit time  $t$  with radial position  $r$ , incident energy  $U$  and opening angle  $\alpha$  can be found in literature; cf., e.g., Hayes *et al.*<sup>28</sup>

$$\left. \frac{\partial t}{\partial r_{\text{in}}} \right|_{\alpha=0} = 0, \quad (3.37)$$

### 3. Instrumental Aspects of the Coincidence Experiment

$$\left. \frac{\partial t}{\partial U} \right|_{r_{in}=R_0; \alpha=0} \sim \frac{3}{4} R_0 \pi \sqrt{2m} U_p^{-3/2}, \quad \text{and} \quad (3.38)$$

$$\left. \frac{\partial t}{\partial \alpha} \right|_{U=U_p; r_{in}=R_0} = 2R_0 \sqrt{2m} U_p^{-1/2} \frac{\cos \alpha}{(1 + \sin^2 \alpha)^2}. \quad (3.39)$$

The resulting transit time spread  $\Delta t$  does not depend on the entrance position in the analyzer, but only on the opening angle inside it and the realized energy resolution.

In terms of timing resolution it is profitable to shape the phase diagram at the entrance of the analyzer in such a way that smaller opening angles occur at the cost of larger off-axial distances. In practical cases the angular time spread is the most important. For example, for a 1-eV energy-resolution setting at a pass energy of 100 eV in a 140-mm radius analyzer, the minimum time spread is 1.1 ns and the time spread due to the opening angle is shown in Fig. 3.8.

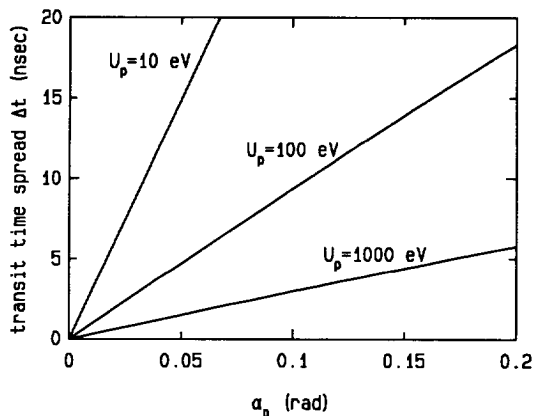


Fig. 3.8: Transit time spread  $\Delta t$  as a function of opening angle  $\alpha_p$  inside a 140-mm radius analyzer, for different values of pass energy  $U_p$ .

#### 3.3.4. Modes of Operation

##### Maximizing number of channels at 100 % transmission

Let us suppose we do not want to introduce slits to limit the beam, but have the optics determine the size of the beam. As long as no slits limit the beam the transmission must be equal to one. The following treatment now holds for a situation with 100 % transmission. Given this choice, we will try to find the optimum resolution and the relationships required for the pass energy in the analyzer and the magnification of the transfer optics.

If we replace the slit width  $\Delta d$  by the probe diameter  $d_p$  Eq. (3.36) becomes:

$$\frac{\Delta U}{U_p} = d_p k_1 \frac{1 + k_3}{k_3}. \quad (3.40)$$

If the detector of total width  $d_a$  is built up of  $N_{\text{ch}}$  channels of width  $d_{\text{ch}}$  and we want each channel to represent some fraction  $k_4$  of the energy resolution, we can relate the required probe size  $d_p$  at the entrance of the analyzer to the channelwidth  $d_{\text{ch}}$  via:

$$d_{\text{ch}} = k_4 \frac{2R}{U_p} \Delta U, \quad (3.41)$$

and using Eq. (3.40) we find

$$d_p = \frac{d_a}{N} \frac{1}{2R} \frac{k_3}{k_1(1 + k_3)}. \quad (3.42)$$

The quantity  $N = k_4 N_{\text{ch}}$  represents the effective energy range in units of  $\Delta U$ .

For  $k_3$  we can now write

$$k_3 = \frac{d_a}{2k_2 N R \alpha_p^2} - 1. \quad (3.43)$$

Using Eq. (3.30) and (3.41) the required kinetic energy inside the analyzer is given by

$$U_p = U_i \frac{\alpha_s^2 d_s^2}{\alpha_p^2 d_a^2} N^2 4R^2 k_1^2 \frac{(1 + k_3)^2}{k_3^2}. \quad (3.44)$$

Minimizing  $\Delta U$  with respect to  $\alpha_p$  for given  $U_i$  yields (after substitution of Eqs. (3.42)–(3.44) in Eq. (3.40)) an optimum probe angle

$$\alpha_{p\text{opt}} = \sqrt{\frac{1}{3} \frac{d_a}{k_2 N} \frac{1}{2R}}, \quad (3.45)$$

which is reached for  $k_3 = 2$ , provided that  $\alpha_p < \alpha_a$ . For the energy resolution this yields, using Eqs. (3.23), (3.25), (3.44) and (3.45)

$$\Delta U = \frac{27C^2 k_1^2 k_2 N^2 R^2}{d_a^2} U_i^2. \quad (3.46)$$

The required value for  $U_p$  then becomes

$$U_p = \frac{54C^2 k_1^2 k_2 N^3 R^3}{d_a^3} U_i^2, \quad (3.47)$$

and the magnification is

$$|M| = \frac{d_a}{3C k_1 N R} \sqrt{\frac{B_f}{B_i U_i}}. \quad (3.48)$$

### 3. Instrumental Aspects of the Coincidence Experiment

If  $\alpha_p$  computed from Eq. (3.45) would come out larger than  $\alpha_a$ , its value should be fixed on  $\alpha_a$ , thereby giving in on the optimum value of  $k_3$ . For our case, if we take  $d_a = 40$  mm,  $R = 140$  mm and  $\alpha_a = 0.15$  rad then only at  $N > 8.46$  is  $\alpha_{p_{opt}} < \alpha_a$ . Below this value of  $N$ , the energy range collected at a time in terms of energy resolution, becomes too small to justify such a 'small though maximum' opening angle. The first term in Eq. (3.36) should then be increased by readjusting both magnification and pass energy. The energy resolution then becomes

$$\Delta U = \frac{2C^2 k_1^2 N R d_a}{\alpha_a^2 (d_a - 2k_2 N R \alpha_a^2)^2} U_i^2, \quad (3.49)$$

with a required value for  $U_p$  given by

$$U_p = \frac{4C^2 k_1^2 N^2 R^2}{\alpha_a^2 (d_a - 2k_2 N R \alpha_a^2)^2} U_i^2, \quad (3.50)$$

and the magnification set for

$$|M| = \frac{1}{2C k_1 N R} \sqrt{\frac{B_f}{B_i U_i}} (d_a - 2k_2 N R \alpha_a^2). \quad (3.51)$$

The behavior of magnification, pass energy and energy resolution for different choices of  $N$  are shown as a function of initial kinetic energy in Figs. 3.9, 3.10 and 3.11.

The required potential  $V_c$  at the central radius of the  $180^\circ$  analyzer is given by

$$V_c = \frac{U_p - U_i}{e}, \quad (3.52)$$

which is shown in Fig. 3.12.

#### Constant $\Delta U$ at 100 % transmission

A different mode of operation, also at 100 % transmission is obtained by keeping  $\Delta U$  constant while varying  $U_i$ . This is only possible by effectively varying  $N$  or  $k_4$  in Eqs. (3.46) or (3.49), depending on the value of  $\alpha_p$ . This requires a somewhat different choice of magnification and pass energy. For several values of  $\Delta U$  the requirements of this mode of operation are also shown in Figs. 3.9 and 3.10. A limitation to this operation is given by  $k_4 \leq 1$ , otherwise the energy resolution is not actually resolved, and by  $k_4 N_{ch} \geq 1$  otherwise the effective energy range is less than the energy resolution. In the latter case one might shift the pass energy over steps less than the energy resolution, thereby collecting the complete spectrum albeit at a longer time than actually required, without real gain of information.

All of the above mentioned discussion on the transfer optics concentrated on the operation at 100 % transmission. Of course with small adaptation this same story could be applied to a differently chosen transmission, which is again kept fixed. But the problem than is that somewhere the probesize and/or angle should be limited by slits in a way which requires continuous adaptation of these slits.

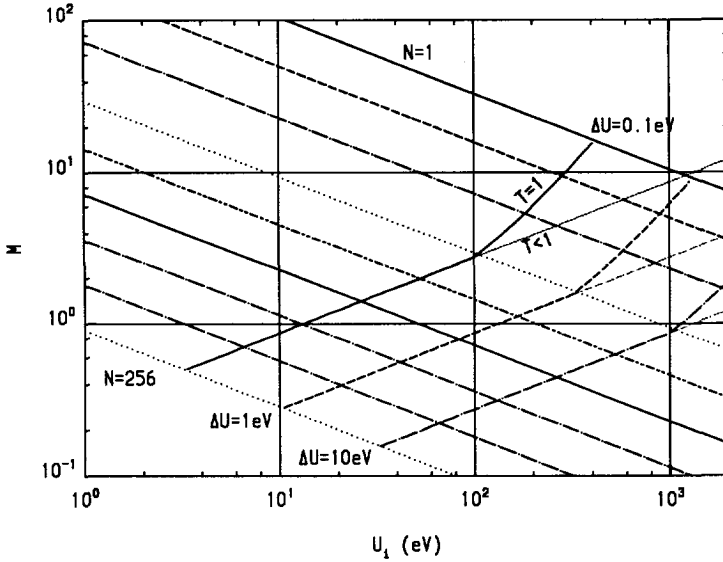


Fig. 3.9: Required magnification of transfer optics for optimum energy resolution at 100 % transmission. Graphs are for various values of  $N$ , from 1 to 256 (powers of 2), with  $d_a = 40$  mm,  $R = 140$  mm and  $\alpha_a = 0.15$  rad. Rising graphs are for constant energy resolution, at 100 % transmission, or (grey lines) smaller transmission at constant pass energy.

### Maximizing the product of number of channels and transmission

If we leave the demand of 100 % transmission, the best optimization that can be made is that of the product of the number of simultaneously detected channels (expressed in units of  $\Delta U$ ) and the transmission per channel,  $NT$ . Here again it should be stressed that the optimization for this mode of operation is only an approximation in case of a non-homogeneously filled phase space. Below we will concentrate on the case that  $\Delta U$  is kept fixed. A fixed value for  $\Delta U$  makes the interpretation of the spectra more direct.

By combining Eqs. (3.40) and (3.42), the number of channels  $N$  can be written as

$$N = \frac{d_a}{2R} \frac{U_p}{\Delta U}. \quad (3.53)$$

We see that if  $U_p$  is kept fixed as well, the number of channels will be constant. The change in  $NT$  will then come only from the change in  $T$ . Transmission will be changed by cutting off some part of the spot at the entrance of the analyzer. The condition of a fixed  $U_p$  makes it relatively easy to realize this mode in practice.

The accepted opening angle  $\alpha_{acc}$  will not be limited by slits, but be determined by the angular magnification of the transfer lenses, so that  $\alpha_{acc} = \alpha_p$ .

### 3. Instrumental Aspects of the Coincidence Experiment

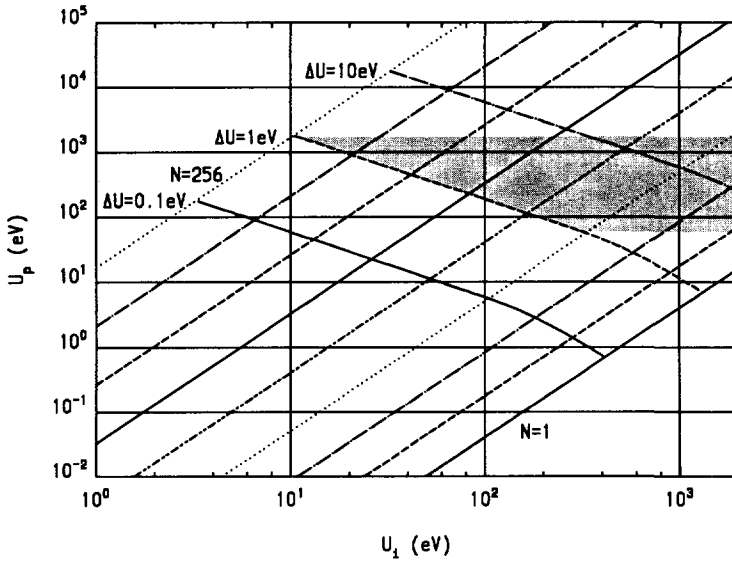


Fig. 3.10: Required pass energy in the  $180^\circ$  analyzer for optimum energy resolution at 100 % transmission. Rising graphs are for various values of  $N$ , from 1 to 256, with  $d_a = 40$  mm,  $R = 140$  mm and  $\alpha_a = 0.15$  rad. Declining graphs show required  $U_p$  for operation at three values of  $\Delta U$  at 100 % transmission. Shaded area shows valid region for operation at fixed  $\Delta U$  (1 eV) and fixed  $U_p$  with transmission below 100 %.

The accepted spotdiameter  $d_{acc}$ , limited by slits at the analyzer entrance plane, will be expressed in the accepted opening angle  $\alpha_p$  and the energy resolution  $\Delta U$  (compare Eq. (3.36)):

$$d_{acc} = \frac{1}{k_1} \frac{\Delta U}{U_p} - \frac{k_2}{k_1} \alpha_p^2. \quad (3.54)$$

Together with Eq. (3.26), (3.32) and (3.53) the product  $NT$  is now given by:

$$NT = \frac{d_a \sqrt{U_p} (\alpha_p - k_2 \frac{U_p}{\Delta U} \alpha_p^3)}{2C k_1 R U_i}, \quad (3.55)$$

which can be optimized with respect to  $\alpha_p$ . For fixed  $U_p$  and  $\Delta U$  we find the relation:

$$NT = \frac{d_a \sqrt{\Delta U}}{3C k_1 R \sqrt{3k_2 U_i}}, \quad (3.56)$$

which, as in the 100 % transmission mode, is reached for  $k_3 = 2$ . In fact  $NT$  turns out to be independent of  $U_p$ . Due to the fact that  $\alpha_p < \alpha_a$  the choice of  $U_p$  is limited on the low side by

$$U_p \geq \frac{\Delta U}{3k_2 \alpha_a^2}, \quad (3.57)$$



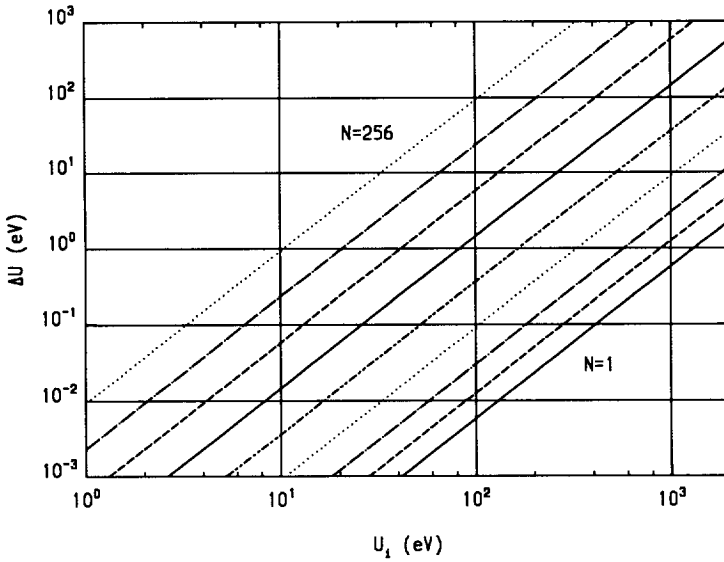


Fig. 3.11: Obtainable energy resolution at 100% transmission. Graphs are for various values of  $N$ , from 1 to 256, with  $d_a = 40$  mm,  $R = 140$  mm and  $\alpha_a = 0.15$  rad.

for our spectrometer this means approximately  $U_p \geq 60\Delta U$ . A practical limit on the high side is given by the maximum number of channels that can be dealt with ( $N_{\max}$ ), so that

$$U_p \leq \frac{2RN_{\max}\Delta U}{d_a}. \quad (3.58)$$

In Fig. 3.13 the behavior of  $NT$  as a function of  $U_i$  is shown for several choices of energy resolution. For comparison with the 100% transmission mode, the graphs for that mode which drop faster at higher energies, are shown as well.

The transmission itself behaves like

$$T = \frac{2}{3Ck_1\sqrt{3k_2}} \frac{\Delta U^{\frac{3}{2}}}{U_i U_p}, \quad (3.59)$$

which for small  $U_i$  is limited by  $T \leq 1$ . This gives another lower limit on the value of  $U_p$ :

$$U_p \geq \frac{2}{3Ck_1\sqrt{3k_2}} \frac{\Delta U^{\frac{3}{2}}}{U_i}, \quad (3.60)$$

In Fig. 3.10 the allowed area for combinations of  $U_p$  and  $U_i$  is depicted for  $\Delta U = 1$  eV, and  $N_{\max} = 256$ . Figure 3.14 shows the transmission as a function of  $U_i$  for the minimum number of channels and for an arbitrary choice of  $N = 64$ .

### 3. Instrumental Aspects of the Coincidence Experiment

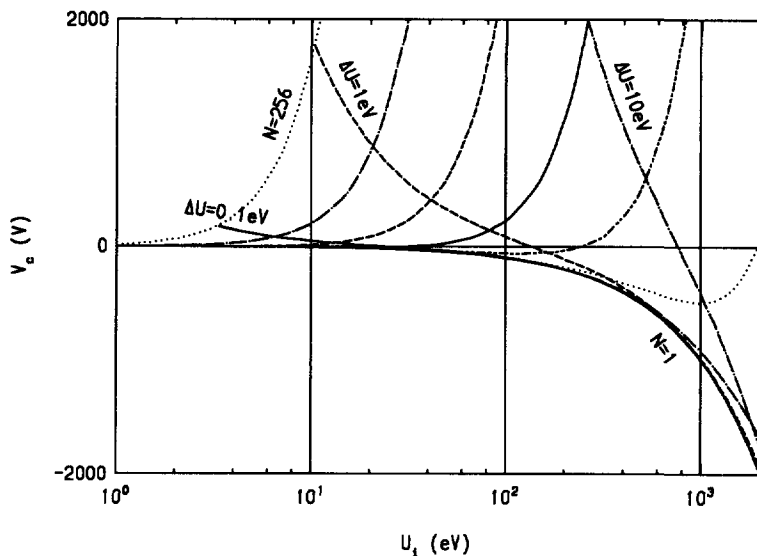


Fig. 3.12: Required potential at central radius of  $180^\circ$  analyzer. Three monotonously declining graphs are for constant pass energy mode, at given energy resolution. The set of (mostly) non-monotonous graphs are for 100 % transmission and optimal energy resolution at various values of  $N$ , from 1 to 256, with  $d_a = 40$  mm,  $R = 140$  mm and  $\alpha_a = 0.15$  rad.

The latter could correspond for example with a 256 channel detector, where each channel represents one quarter of the energy resolution ( $k_4 = 0.25$ ).

The magnification that is required for this mode varies according to

$$|M| = \sqrt{\frac{3k_2 B_f}{B_i}} \sqrt{\frac{U_i}{\Delta U}}. \quad (3.61)$$

This shows the same behavior for  $M$  as was required for operating at constant energy resolution with 100 % transmission (see grey lines in Fig. 3.9). In that mode this behavior changed where  $\alpha_{p\text{opt}}$  became larger than  $\alpha_a$  so that a larger magnification was required to keep the transmission one.

#### Concluding remarks on operating mode for transfer optics

From above considerations we may draw the conclusion that there is not very much difference in performance for either the 100% transmission mode or the constant pass energy mode. The 100 % transmission mode is aimed at either optimum energy resolution at a given number of channels or at a maximum number of channels at a given energy resolution. This mode must give in something on the value of  $NT$  when operating at constant energy resolution mode (see Fig. 3.13). However

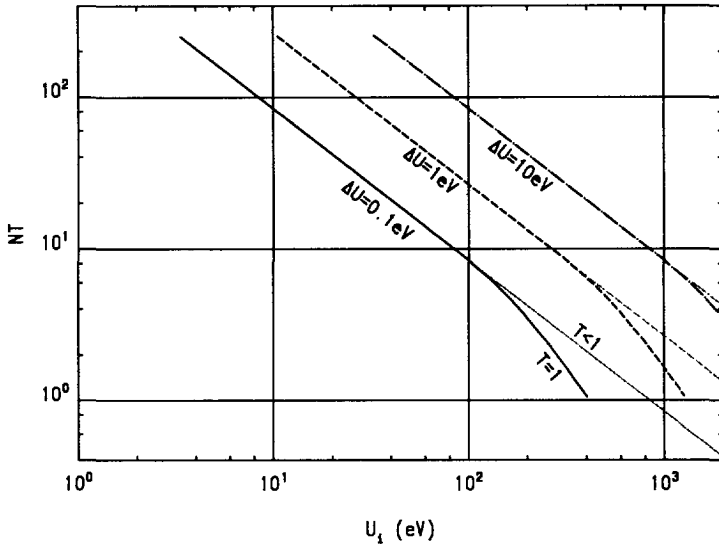


Fig. 3.13: Number of energy channels times transmission as a function of initial energy, for several values of  $\Delta U$ . Black lines are for the 100 % transmission mode, grey lines for the constant pass energy mode. Graphs are for a spectrometer with  $d_a = 40$  mm,  $R = 140$  mm,  $\alpha_a = 0.15$  rad and  $N_{\max} = 256$ .

no part of the original angular distribution of the electrons is discarded, so that this mode gives the most complete information on the emitted-electron energy distribution.

On the other hand, the mode of operating at constant pass energy and constant energy resolution, while varying the transmission is specifically aimed at maximizing  $NT$ . It has the advantage of easier practical operation of the spectrometer and more direct interpretation of the raw spectra obtained with this mode. As a consequence of the reduction of transmission, the inhomogeneities of the phase space at the beam-limiting slits appear directly as intensity changes in the spectrum, whereas in the 100 % transmission mode such inhomogeneities only appear due to changes in energy resolution. A reduced transmission also indicates a particular loss of signal from the higher angles of emission.

The seriousness of losing this information depends on what one wants to measure. For Auger spectroscopy aimed at identifying different materials in the specimen, the intensity in the peaks is the most important parameter. If we are interested in specific differences between several Auger peaks of one material, the angular dependence could become important, due to differences in angular emission. For coincidence spectroscopy we have seen in Chapter 2 that especially from the top surface a certain minimum amount of upward momentum is required to

### 3. Instrumental Aspects of the Coincidence Experiment

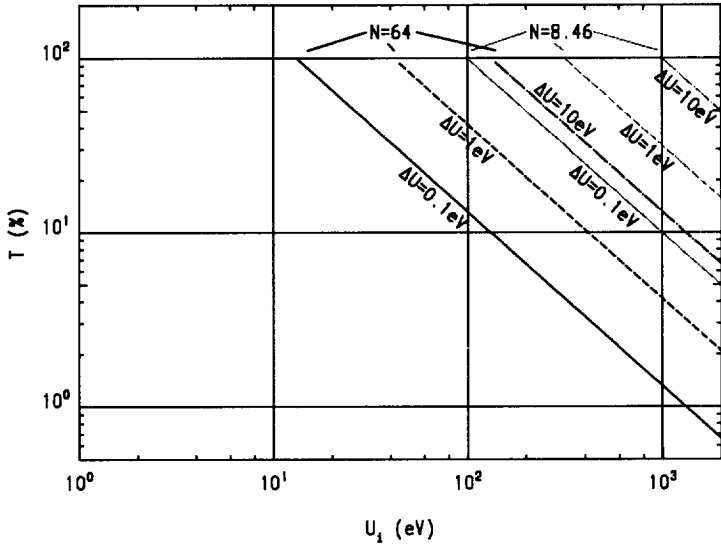


Fig. 3.14: Obtainable transmission for fixed pass energy and energy resolution. Two sets of graphs are for two different values of  $N$ : 64 and 8.46, the minimum number of channels. Each set shows three graphs for different values of energy resolution. Graphs are for a spectrometer with  $d_a = 40$  mm,  $R = 140$  mm and  $\alpha_a = 0.15$  rad.

overcome the workfunction at the surface. A reduction in collection angle, caused by a reduced transmission, will in a similar way demand a certain minimum ratio of upward and sideward momentum.

To get an idea about the transmission for a more or less realistic angular distribution, the following estimate has been made. We assume a so-called (three-dimensional) cosine distribution for the emission of electrons from the sample. This distribution is based on an approximation that electrons generated inside the sample can only escape in a certain direction if the pathlength inside the sample is smaller than the mean free path. The workfunction barrier is not included in this model. In two dimensions this distribution should be multiplied by the solid angle which is proportional to the sine of the angle with the normal. The distribution then looks like a  $\sin(2\alpha_i)$  function.

Suppose the transmission is reduced by placing slits in the beam (centered on the optical axis). The effect on this distribution can only be given when the exact relation between starting angles at the sample and positions in the plane of the slits is known. This relation however reflects the complex behavior of the parallelizer and will not be used here. Instead, as an approximation we will make use of Eq. (3.24), which gives a lower estimate on the actual transmission. By doing that we actually curl up the already quite curled-up graph of a parallelizer phase

diagram, so that effectively each starting angle is transformed into a circle (in a 'reduced' phase diagram) of which the 'radius'  $\alpha_f$  behaves like Eq. (3.24). The transmission as a function of initial angle is then as shown in Fig. 3.15 for several values of  $T$  as defined by Eq. (3.32). The effect of the angular transmission on the

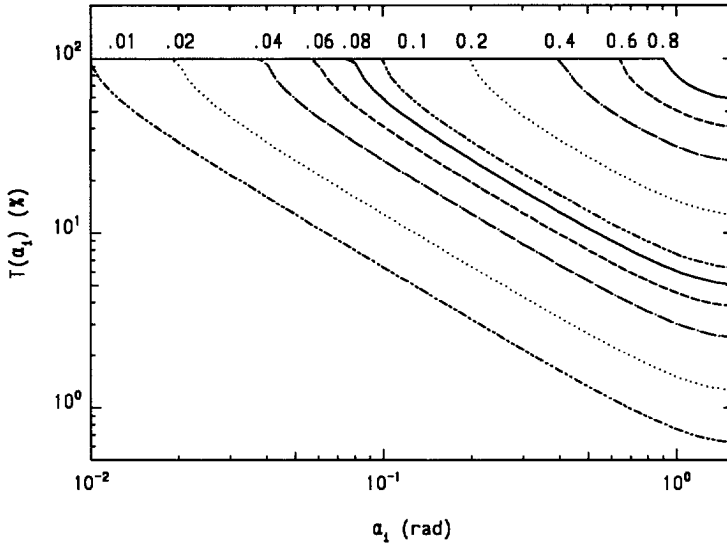


Fig. 3.15: Lower bound for angular transmission due to (idealized) parallelizer action, shown for several values of  $T$ , defined as the accepted fraction of a square phase diagram.

angular intensity distribution of a cosine distribution is shown in Fig. 3.16. The minimum for the integral intensity that is detected with a system with (ideal) parallelizer and partly closed slits is computed by integration of the curves of Fig. 3.16. Figure 3.17 shows the fraction of the total emitted current that is detected for a cosine distribution as a function of  $T$ .

### 3.3.5. Post-Spectrometer Optics

The most obvious solution for post-spectrometer optics is to have none at all: placing a detector at the spectrometer endplane. The equipotential plane at the detector input side can have an effect on the equipotential distribution inside the analyzer. The detector plane can be interpreted as a so-called Herzog correction with closed slits. Such a correction is often applied to give a well-defined end to the analyzer sector. For a CHA with  $180^\circ$  mechanical sector angle this means that the object plane should lie just inside the analyzer. Of course, placing a slit inside the analyzer will also disturb the analyzer equipotential distribution, but a virtual slit can be positioned at this plane, by imaging a real slit using pre-spectrometer optics.

### 3. Instrumental Aspects of the Coincidence Experiment

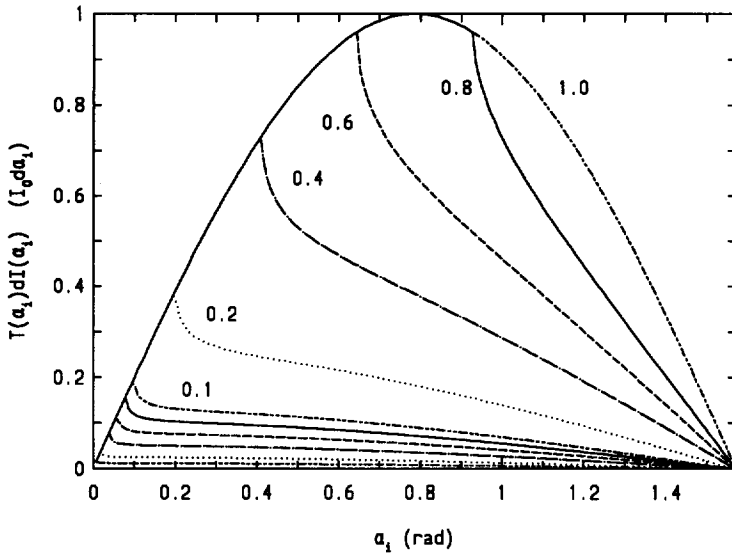


Fig. 3.16: Transmitted intensity for cosine distribution for several values of  $T$ .

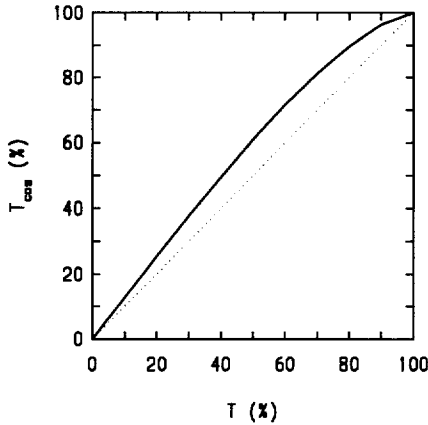


Fig. 3.17: Actual transmission for cosine distribution as compared to the accepted fraction of a square phase diagram ( $T$ ).

An alternative solution is to use a real entrance slit at the entrance of the CHA, preferably in the Herzog-correction position, and image the spectrometer endplane on the detector using actual post-spectrometer optics. Such optics can exist of a more or less simple lens system but can also include for example a second spectrometer, this to minimize stray electron problems.

By employing Herzog correction on both begin and end of the analyzer, real entrance slits as well as a detector at the endplane can be used. This can be achieved with a mechanical sector angle somewhat smaller than  $180^\circ$ .

Another viewpoint for post-spectrometer optics is the minimization of timing inaccuracies. Due to different trajectories in the spectrometer, different flighttimes result, see Eq. (3.39). By clever design of the post-spectrometer optics it may be possible to compensate for flighttime differences, for example by using decelerating lenses at suitably chosen positions. The concept of *isochrones*,<sup>29,30</sup> surfaces of equal flighttime, can be of help in this design process. In principle such flighttime considerations can already be incorporated in the pre-spectrometer optics, but an extra constraint on that optics is maybe hard to fulfill.

Like with the EELS measurement it may be necessary to match the spectrometer dispersion with the size of the detector. Because of the combination of requirements to accommodate large object size (larmor radius), large acceptance angle and small energy resolution (at low pass energy), the spectrometer image size will have to be fairly large, compared to the intrinsic resolution of detector types (e.g. 20–50  $\mu\text{m}$  for MCPs). This indicates that even without post-spectrometer magnification the detector does not have to limit the obtainable resolution. If total detector size  $d_a$  is limited it can even be advantageous to demagnify the spectrometer endplane. In any case post-spectrometer optics must be designed to accept both large object size and large opening angles, which means that off-axial aberrations can play an important role.

A last but important purpose of post-spectrometer optics can be the optimization of the electron velocity, to match the detector sensitivity. Best energy resolution is normally reached with low spectrometer pass energy, while maximum sensitivity of detectors occurs at electron energies on the order of 1000 eV. Fortunately in 3.3.4 it was shown that for example 1-eV energy resolution operation at 1000 eV pass energy is a good possibility for a detector with many channels (see shaded area in Fig. 3.10).

### 3.4. Electron Detection

The detection of electrons can be based on three main principles: a) the creation of photons in a scintillation material, which can be subsequently detected in a photo-multiplier tube, b) the creation of electron-hole pairs in a semiconductor material, or c) the creation of several secondary electrons, a process which can be subsequently repeated to release more of them. Normally type a) and b) are used for fast-electron detection, and c) is used for slower electrons. We will distinguish between possible detectors for the ‘slow’ emitted electron analysis, and detectors for the fast EELS electrons. After that, parallel detection of both slow and fast electrons, and the combination of two detectors in a parallel coincidence setup, will be discussed.

### 3.4.1. Slow-Electron Detection

Electron detectors for the emitted electrons, will have to be sensitive in the low energy range of the spectrum. In this range detection principles based on scintillation or electron-hole pair creation are not very efficient. Most efficient are detectors which use the principle of secondary electron production. Such detectors are (windowless) discrete electron multipliers, channel electron multipliers (channeltrons) and *microchannel plates* (MCPs). An electron multiplier consists of a discrete number of 'dynode' electrodes which repeatedly accelerate the emitted electrons and increase their number by a secondary electron emission process, like in a *photomultiplier tube* (PMT). A channel electron multiplier is a continuous form of the discrete electron multiplier, with a resistive layer on the inside of a glass capillary tube. A high voltage put across this tube causes the secondary electron amplification process. Both types of electron multipliers are single channel detectors, and because of their size are not very suitable to form an array of detector elements.

A MCP basically consists of many parallel miniaturized channel electron multipliers,<sup>31</sup> placed under a small bias angle with the normal of the plates, typically  $10^\circ$ . The individual channels are hexagonally packed, with typical channel diameters of  $10\text{--}50\ \mu\text{m}$ , and have length to diameter ratios between 40 and 100. MCPs can be stacked on top of each other to increase gain, and improve the pulse height distribution of the charge pulses which leave the back of the last plate. MCP detectors yield relatively large electrical pulses with preservation of both timing and positional information, which opens the door to parallel coincidence detection.

A disadvantage of an MCP based detector is that it is limited by the recovery time of the individual microchannels. This means that each channel after being triggered by incident particles shows reduced gain for times up to the order of 0.1 s. The positive charge that remains at the output end of a microchannel, due to the emission of a cloud of electrons, suppresses succeeding electron amplification. The charge must be restored by a strip current, which flows through the MCP. The resulting dead time increases with gain (per channel), and the resistance of a channel. Commercially available MCPs<sup>32</sup> are specified to be linear for output currents which do not exceed  $\approx 5\%$  of the strip current. This is equivalent to a dead time on the order of 50 ms, representing a few  $RC$  times, with  $R$  and  $C$  the resistance and capacitance of the MCP (per channel).

Considering optimized electron optics in the sense of using relatively large dimensions perpendicular to the dispersion direction (for example by using quadrupole optics<sup>18</sup>), gives an upper limit for the amount of individual microchannels that accompany each (effective) energy channel and with it also the maximum countrate per energy channel. For example for a  $22 \times 20\ \text{mm}^2$  detector, with 96 strips of each  $200\ \mu\text{m}$  by  $20\ \text{mm}$  and for a stack of two MCPs (required for enough gain), with  $15\ \mu\text{m}$  separation between individual channels ( $2 \times 10^{-10}\ \text{m}^2/\text{channel}$ ), this effectively means that there are about  $2 \times 10^4$  microchannels per strip. If on top of this we assume an effective triggering of about 7 channels per incident particle (caused by spreading between the two MCPs), then this indi-



cates a number of about  $2.9 \times 10^3$  independent trigger positions per 50 ms, or  $5.7 \times 10^4$  cts/s/detectorstrip. When multiplied with the number of channels this indicates a maximum total detector countrate of  $5.5 \times 10^6$  cts/sec. Of course with this approximation one assumes a completely homogeneously exposed MCP, so that in practice at these total countrates non-linearities will already play a role. Especially for the position-sensitive readout systems, this can cause problems.

Any improvements on above choices, should be based on either larger detectorstrip dimension, smaller microchannel spacings, or materials with lower resistivity. The MCP gain should be chosen just high enough to enable discrimination of incoming particles against background noise. Preventing the spreading over the above mentioned 7 microchannels in between the two MCPs, (by decreasing the distance, or increasing the voltage difference between them) reduces overall gain, but effectively decreases dead time. Since perfect matching over the complete MCP area will be practically impossible, at least 2-3 channels of the second MCP will be triggered.<sup>33</sup> Using longer, curved channel MCPs, which yield gains comparable to stacked straight channel MCPs, prevents problems of spreading.

### Background Signals

For a MCP based detector, several sources of spurious background signals exist. Since a MCP is sensitive for stray electrons, ions, and ultra-violet (UV) and x-ray photons, several protective measures should be taken to reduce the number of counts produced by them. If possible, stray-light apertures and electron and ion traps should be used. Of course the electron trap (e.g., a high transmission decelerating grid) should have no or little effect on the emitted electrons under study, but should stop slower electrons which may be caused by scattering or photo emission on slits or analyzer surfaces. Care should be taken that scattering on the grid of an electron trap does not increase the background. Ions can for instance originate from ion getter pumps, or vacuum gauges, and they should be carefully screened from the detector. Also internally in the MCP, due to the large number of electrons that are released at electron impact, ionizations may occur (depending on vacuum level). The electric field in the microchannels can accelerate the ions back to the front of the MCP (ionic feedback), where they can start new cascade processes, which will contribute to background counts.

#### 3.4.2. Fast-Electron Detection

Slit-Scintillator-Photomultiplier detectors (see Fig. 3.18) are well-suited for normal (serial) EELS as well as for coincidence EELS spectroscopy. The technique for these systems is reliable, it provides single electron counting possibilities at high detection efficiency with fast timing (using plastic scintillators) and the additional possibility of analog counting at high incident currents.

For parallel energy loss spectroscopy there is no such recognized best-suitable detection scheme. Most present-day parallel detectors employ a diode array, based on electron-hole pair creation, with internal readout circuitry.<sup>17,18,34</sup> In between

### 3. Instrumental Aspects of the Coincidence Experiment

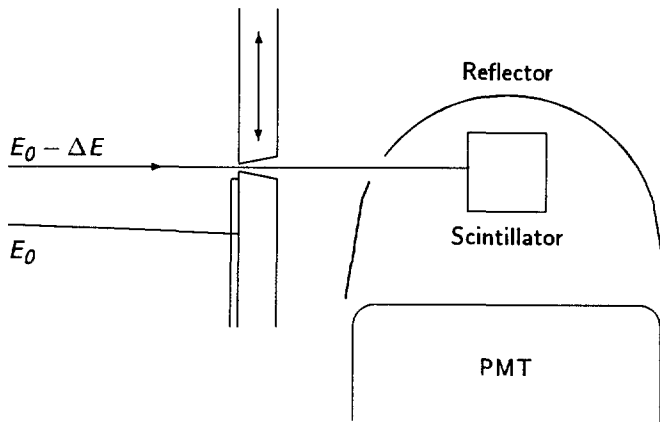


Fig. 3.18: Schematic slit-scintillator-photomultiplier detector. Fast electrons that have passed a dispersive element are focused on the plane of the slit. Only those electrons of a selected energy are able to pass the slit and reach the scintillator. The light created inside the scintillator is reflected toward the photomultiplier, which in return gives an electrical signal. The width of the slit can be adjusted to give a certain energy resolution.

readouts (typical timescale of milliseconds) the counts in each channel are integrated and this makes these detectors rather unsuitable for coincidence spectroscopy.

Another approach for parallel detection uses 'position-sensitive detectors', which respond to incident electrons by producing an electrical signal in an electrode at each end of the device, see Fig. 3.19. Normally these type of detectors are based on microchannel plates.

We investigated the possibility to design a detector, which did not incorporate a microchannel plate.<sup>35</sup> By using a scintillator the fast-electron signal can be converted to a light pulse. An optical system images the scintillator onto a mirror that has variable transmission along the dispersion direction. The transmission and reflection side of the mirror are each imaged on a different photon detector (PMT). From the ratio of the number of photons which reach these detectors one can determine the position on the variable transmission mirror, and thus the position on the scintillator. However, preliminary tests of such a system failed because of too large gain variations of the PMTs that were used.

For MCP-based position-sensitive detectors the electrical signals are formed by a cloud of electrons leaving the MCP. Since the detection efficiency of MCPs for fast electrons is not so high (on the order of 10%), an intermediate conversion seems inevitable. A possible conversion is one to photons, by using a scintillator. This requires a fiber-optics or lens coupling and a photocathode in front of the MCP.

As alternative to the use of photons, a conversion from fast to slower (secondary) electrons in some intermediate material may enhance the detection sensitivity. The conversion-material properties should of course be optimized for this purpose.<sup>36</sup> Considerations for these properties are high secondary electron yield (using a low workfunction), low lateral spreading of secondary electron production (using e.g., a thin transmission layer), and low x-ray production, to prevent lateral resolution degradation and enhancement of spurious background counts. The latter can be caused by photo electrons that are being released by stray x rays.

Common to all approaches for parallel detection is the need for good alignment and adjustment of the spectrometer. For serial acquisition systems such as the slit-scintillator-PMT system, the alignment procedure for a magnetic spectrometer has been well solved. This alignment is mainly performed with the zero-loss electrons, which have the highest intensity. Some parallel detectors may not be capable of dealing with the full zero-loss intensity, in which case other alignment procedures must be followed. A serious option for parallel detector setups is to have a serial system available, next to the parallel system. A possible solution is given by Batson<sup>34</sup> where an electron optical deflection can be invoked for choosing one of two detectors.

### Background Signals

The EELS technique has known a lot of spurious background sources, which in the serial EELS, with slit-scintillator-photomultiplier systems (Fig. 3.18) have been largely overcome.<sup>10</sup> Scattering of the fast electrons at residual gas particles, at angle-defining apertures, at the analyzer surfaces and finally at the analyzer slit blades are well-understood causes for this background. Minimization of these effects is achieved by careful design of the electron optical system and placing of (extra) apertures at positions where scattering causes least possibilities to reach the detector. If one likes to use large acceptance angles, to get higher detection efficiencies for certain scattering processes, the sensitivity to unwanted forms of scattering will also be larger.

The quality of the vacuum determines the probability for residual gas scattering. The ultra-high vacuum which is required at the specimen level to ensure useful surface-sensitive measurements (order of  $10^{-8}$  Pa), must be extended to good vacuum conditions (order of  $10^{-5}$ - $10^{-6}$  Pa) in the region from specimen to EELS detector.

When collecting a spectrum, almost all current hits the analyzer slits. Therefore effects associated with (multiple) backscattering mainly occur on these slits. Using special (conducting) carbon coatings on the slits minimizes backscattering. Another source of background signals is given by x-ray penetration through the analyzer slit blades and (after reflection) through the slit itself. Using thick slits (5 mm) with slit angles close to  $90^\circ$  reduces the x-ray penetration.

The dark current of the PMT is another source of background noise. It can be minimized by careful selection of the material of the first dynode, good matching

### 3. Instrumental Aspects of the Coincidence Experiment

with the scintillator output to raise sensitivity and thus lower the required gain, and finally by cooling the PMT. For (single-channel) coincidence EELS the sources of all these unwanted effects are exactly similar, as long as the post-specimen part or detector are unchanged. The influence of spurious counts on a measurement must be related to the normal signal strength (both true and false coincidences, see 3.5). Spurious counts can only contribute to false coincidences. The coincidence technique will therefore effectively filter out a great deal of the background counts.

For parallel EELS some of the background sources which were taken care of in the case of serial EELS may reappear. Parallel EELS is in conflict with the use of analyzer slits. This means that x-ray photons and multiply backscattered electrons will no longer be stopped by them. Fortunately these background counts will be spread out over the complete detector, so that the signal to background ratio per channel will not differ too much from that in serial operation.

#### 3.4.3. Parallel Electron Detection

For parallel detection of electrons several options are available. Based on considerations in 3.4.1 and 3.4.2 only MCP based detectors will be considered. Parallel detectors can be either discrete, or have shared outputs from which position and/or timing can be deduced.

A position-sensitive detector of the type shown in Fig. 3.19, can be based on two principles. Either the relative amplitude of the two signals or the time-delay

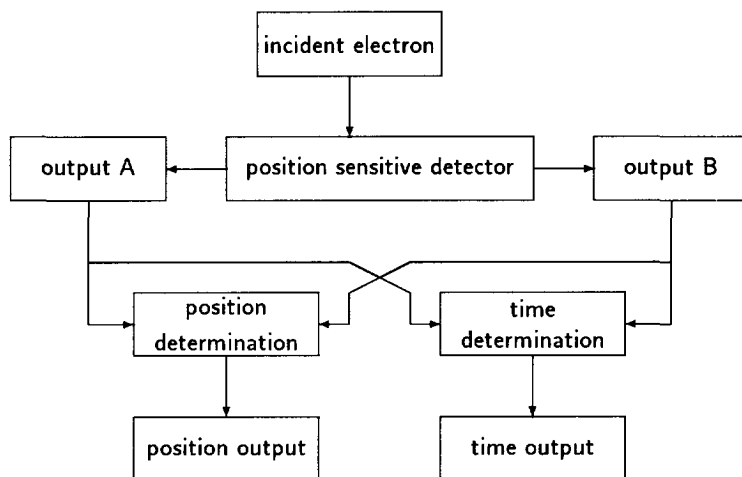


Fig. 3.19: Principle of a position-sensitive detector. The signals arriving at the two ends of the detector are used to determine both position and time of the electron impact.

between them gives a measure for the position where the incident electron hit the detector. Alternative schemes can use more than two signal amplifiers to prevent problems of non-linearity due to stray capacitance.<sup>37</sup>

The time of impact on the detector can also be deduced; either from the combination of outputs A and B, or from one of those combined with the position output. In addition to this, on the exit plane of the MCP a positive charge pulse results, caused by the electrons which were released and accelerated to the anode. This pulse can be used to extract the timing information. A position-sensitive detector system has as main disadvantage that only one incident electron on the whole detector can be dealt with, during the time required for determining the incident position.

Charge division can be achieved by charge dissection along a capacitively coupled network or along a resistive network. In both cases the position-sensitive detector consists of a resistor or capacitor chain, connected to a series of detector strips behind the MCP. A continuous anode can be seen as an extreme form of the resistive network. A fundamental limit to the speed of these devices is the  $RC$  time of the anode, which can be made as small as 50–70 ns.<sup>33</sup> In general however the speed of the charge division detectors is not limited by the response time of the network, but rather by the processing electronics.

The actual division can either be performed in analog electronics, followed by an analog-to-digital conversion, or in digital electronics after two analog-to-digital conversions, which can be done in parallel. To save time during data-acquisition the digital division can be postponed to the post-processing phase, but performing the division directly gives a useful data-compression. A digital division of 16-bit words can for example be performed within 44 clock cycles (of a general purpose 68030 processor), which at present clock rates of 50 MHz amounts to less than 1  $\mu$ sec. Fast analog-to-digital converters (ADCs) are available for video purposes and can be operated at countrates up to 30 MHz for an 8-bit flash ADC.<sup>38</sup> Higher precision successive-approximation ADCs are considerably slower and can be operated at countrates up to 800 kHz for 12-bit resolution.<sup>39</sup> Faster 12-bit subranging ADCs running at countrates up to 10 MHz are available too, at considerably higher cost. Analog division at up to 1% accuracy<sup>40</sup> (effectively 100 parallel channels) is limited to countrates below 20 kHz. Fast analog multipliers can also be operated as dividers, but in this mode less accuracy is reached (for example 1 MHz at 3% accuracy<sup>41</sup>).

Another way to go is to use a MCP with behind it an array of individual detector strips each connected to a preamplifier and subsequent coincidence electronics, see Fig. 3.20. The interpretation of pulses on these strips is quite straightforward. The omission of the division operation makes it faster and above that each strip can count electrons simultaneously, but the amount of coincidence electronics and the way of connecting that to the other coincidence detector(s) make it rather complicated. A possible situation in which it is useful to be able to register simultaneous counts within one detector, is where both the virtual-photo electron and the Auger electron fall within the detector energy range, in combination with an energy-loss electron yielding a triple coincidence. In other situations only one count can be identified as a 'true' coincident count that belongs to a count in the

3. Instrumental Aspects of the Coincidence Experiment

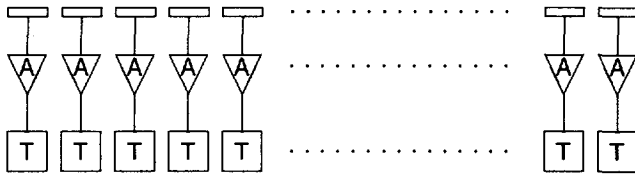


Fig. 3.20: Principle of a detector with individual timing electronics. Each detector strip is connected to individual amplifiers (A) and subsequent timing outputs (T).

other coincidence detector.

To avoid the complicated combination of two detectors with individual timing electronics one could choose to have each strip connected to separate preamplifiers and to a shared coincidence circuit, see Fig. 3.21. A single timing signal can be

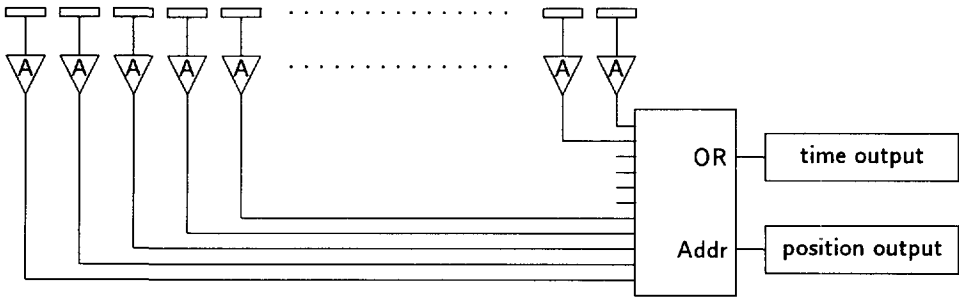


Fig. 3.21: Principle of a detector with combined timing electronics. Each detector strip is connected to individual amplifiers (A) and to an logical circuit, which gives the 'address' of the hit strip and performs an OR function for the time output.

obtained either from the MCP, or from some logical OR function of the amplifier outputs. This way one can again have only one incident electron at a time at the whole detector, but the duration for which this holds is much smaller, since no analog-to-digital conversion has to take place. In case the charge cloud from the MCP can reach more than one individual detector strip, some centroid finding electronics should be applied. If only one strip at a time can be hit, such electronics is based on a simple 'encoder' circuit. If one wants to be able to handle cases where two or more electrons reach the detector simultaneously, it becomes necessary to save the stream of data in latch registers, which can be accessed by fast processors. At present, dedicated hardware is being designed, which makes use of such fast processors and can manage very high countrates.<sup>42,43</sup>

In case it takes relatively much time to determine the time difference between arrival of the electrons in the two detectors, as in TAC-based systems (order of

$1 \mu\text{sec}$ ),<sup>44</sup> it is convenient to save the position information of the coincident count that is being processed in some temporary register. Normal (non-coincident) counts can then be registered in the mean time. Partial schematics for a parallel coincidence detector set-up, with the simultaneous possibility to register the regular EELS and/or emitted-electron spectra, based on individual detector strips are shown in Fig. 3.22. These schematics only give the basic components of the sys-

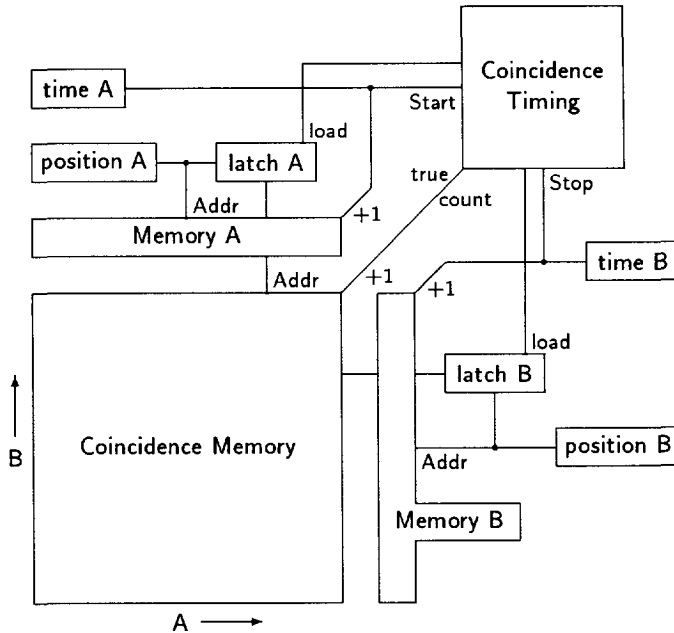


Fig. 3.22: Simplified schematics for doing both regular and coincidence spectroscopy. The time and position output for detectors A and B are for example taken from a detector with a principle as shown in Fig. 3.21. The address in the coincidence memory is formed by a combination of the position-information data from both detectors. This information can include the absolute settings of the analyzer energies, which asks for one big memory, representing a large part of the full 2-D coincidence spectrum (Fig. 1.2). If the analyzer settings are not included in the position information, the data should be transferred to another (larger) memory, before the analyzer settings are changed. The '+1' indicates a request to start an increment operation on the addressed memory location. At some points in the schematics, enable and disable signals as well as delays may be required to synchronize the dataflow.

tem. In practice they may need to be somewhat more complicated in order to work properly at high countrates, prevent dead-times, and to enable data-transfer to a computer system. Preferably also a false coincidence memory should be present,

so that a correction for false coincidences can be made after spectrum acquisition; see 3.5. A disadvantage of this simplified hardware-based schematics is its lack of flexibility. Systems based on fast data processors are easier upgraded or adapted to new tasks.

Under certain conditions different detector positions are associated with different flight times of the electrons,<sup>28</sup> see also Eq. (3.38). In that case, for better timing accuracy, it is necessary also to provide the position information to the coincidence timing unit.

Using high-speed time-to-digital converters (TDCs) the time information can be available within a few nanoseconds after arrival of the stop pulse. If known flight-time differences as a function of impact position of the detector can be fully pre-compensated, the speed for coincidence spectroscopy is ultimately limited by the remaining intrinsic time resolution. Before this limit is reached, delay times (order of 50 nsec) associated with data transport to memory registers will start to play a role.

### 3.5. Coincidence Parameters

In any coincidence experiment there is a problem of distinguishing between the real or true coincidences and the random or false coincidences (coincident noise). In this section the parameters that determine the amount of true and false coincidences will be discussed. For this we must first know what we will call the real or true coincidences.

*True coincidences* are the events where two particles are detected that are caused by a single event, the impact of a single particle on the specimen of interest. In the present study the impact particle is a primary electron and the two outgoing particles are this same electron after it has lost a specific amount of energy and the emitted electron which is created in the specimen as a result of this energy loss.

From Chapter 2 we know that the emission takes place almost immediately after passage of the primary electron. To make a coincidence technique work this timing information is essential and it should not be lost. As was discussed in sections 3.2 and 3.3 some uncertainty in timing will arise from among other things different flight paths or electronics jitter. This does not mean the timing information is completely lost. We still can relate the two detector signals to each other when they arrive within the time window given by the different causes for timing imprecision.

In practice (where this time window will be in the nanosecond range) it does however mean that the timing information which might give clues to the physical processes involved, (in the (sub-)picosecond range,) is completely obscured. Therefore different physical processes which yield the two detected electrons cannot be distinguished by a coincidence method that has a timing imprecision which is a



few orders of magnitude larger than the timing spread involved in the creation and emission process.

Now we know there is a certain (non-zero length) time window in which the true coincidences are grouped, we are also faced with the possibility that both detectors detect an electron within this time window which are not caused by a single event. Any pair of unrelated and detected electrons that arrives within the time window as set for the true coincidences is called a *false coincidence*.

Since both true and false coincidences can occur in the same time window, timing itself cannot give an absolute distinction between both types. Of course because of different origin of both coincidences there are parameters which determine the amount of coincidences and the ratio between both types. In this section these parameters will be discussed.

### 3.5.1. False Coincidences

The false coincidence count rate  $R_F$  can be estimated most easily in the case where no true coincidences are present and the count rate of both start signal ( $R_\alpha$ ) and stop signal ( $R_\beta$ ) is low compared with the coincidence time window  $\tau$ , ( $R_\alpha\tau \ll 1$  and  $R_\beta\tau \ll 1$ ). The false coincidence count rate is then given by the count rate of the stop signal multiplied by the fraction of time that the coincidence time window is open. Since this fraction of time is given by the count rate of the start signal times the coincidence time window, we find:

$$R_F = R_\alpha R_\beta \tau. \quad (3.62)$$

Of course when the count rate of either signal is too high things go wrong. For this we will consider the distribution of time differences between unrelated start and stop signals.

Since the start signal, the moment the time measurement is begun, has no relation with the stop signal, it is only the stop signal that determines the timing distribution of the time differences. For such a random (Poisson distributed) counting process the time-delay spectrum has the form of a decaying exponential function. At zero time difference the false coincidence rate will approach the value as given by the above formula. The  $1/e$  value is reached at a time difference which equals the average time interval between stop signals ( $1/R_\beta$ ).

At higher count rates not all start signals can be used for the time difference measurement. Since the electronic processing takes a while, typically at least as long as the time difference itself, the false coincidence count rate at zero time difference will be decreased with a factor  $1/(1 + R_\alpha\tau_{\text{dead}})$ . Here  $\tau_{\text{dead}}$  is the so-called *dead time* during which no new start pulses are accepted, and where we assume that such pulses do not extend the dead time itself (nonparalyzable dead time behavior). Clearly this dead time is decreasing the true coincidence count rate in exactly the same way, provided that true coincidences occur near zero time difference. To minimize the effect of signal loss due to dead time, the start signal should be the one with the lowest count rate. In case a coincidence spectrum is

### 3. Instrumental Aspects of the Coincidence Experiment

collected in which only one of the two signals is swept, preferably the fixed one should be taken as the start signal to prevent changes in system dead time. Unfortunately these demands can be conflicting, in which case correction is necessary. Interchanging start and stop signals is easily done by introduction of fixed (cable) delays.

The rate of both start and stop signal are linearly related to the rate of the incoming electrons and thus the probe current. Using Eq. (3.62) we can write the relation

$$R_F = Y_\alpha Y_\beta \frac{I_{\text{probe}}^2}{e^2} \tau, \quad (3.63)$$

where  $Y_\alpha$  and  $Y_\beta$  are the yield of start and stop counts per primary electron. Most noteworthy is the quadratic relation of the false count rate with probe current.

#### 3.5.2. True Coincidences

Just like the rate of both start and stop signal the rate of true coincidences is linearly related to the probe current:

$$R_T = Y_{\text{true}} \frac{I_{\text{probe}}}{e}. \quad (3.64)$$

Since all coincidences fall within the coincidence time window  $\tau$  the true count rate is independent of this parameter. If the time window is chosen somewhat differently, either shifted in time or too small to contain all true coincidences, this would mean a fraction of the true counts is lost. This fraction could be thought to be incorporated in  $Y_{\text{true}}$ . Doing so, will however increase the sensitivity to changes in the exact time difference, caused for example by temperature variations in electronic components.

#### 3.5.3. True to False Ratio

With Eq. (3.63) and (3.64) we find the ratio of true to false counts:

$$\frac{R_T}{R_F} = \frac{Y_{\text{true}}}{Y_\alpha Y_\beta} \frac{e}{I_{\text{probe}} \tau}. \quad (3.65)$$

The yields  $Y$  can be written as a combination of a production and collection part. The production part contains atomic density  $n$ , the specimen thickness  $t$  and the cross section  $\sigma$ . The cross section depends on the position in the spectra, so that  $\sigma_\alpha = \sigma_\alpha(E_\alpha)$ ,  $\sigma_\beta = \sigma_\alpha(E_\beta)$  and  $\sigma_{\text{true}} = \sigma_{\text{true}}(E_\alpha, E_\beta)$ . In this treatment the short notations will be used. The collection part of the yield contains the fraction  $f$  of the electrons that can escape from the specimen, the transmission  $T$  of the transfer optics, and the collection efficiency  $\eta$  of the detector(s) involved. Therefore we can write:

$$\begin{aligned} Y_\alpha &= nt\sigma_\alpha f_\alpha T_\alpha \eta_\alpha, \\ Y_\beta &= nt\sigma_\beta f_\beta T_\beta \eta_\beta, \\ Y_{\text{true}} &= nt\sigma_{\text{true}} f_\alpha f_\beta T_\alpha T_\beta \eta_\alpha \eta_\beta, \end{aligned} \quad (3.66)$$

so that the true to false ratio becomes

$$\frac{R_T}{R_F} = \frac{1}{nt} \frac{\sigma_{\text{true}}}{\sigma_\alpha \sigma_\beta} \frac{e}{I_{\text{probe}}} \frac{1}{\tau}. \quad (3.67)$$

From this equation we learn that to observe a well defined coincidence peak in a time difference spectrum a good time resolution  $\tau$  and a low beam current  $I_{\text{probe}}$  are required. Also the two spectrometers should be set in such a way that the chance for coincidences is relatively high. The best specimen is thin and has a low atomic density. Since the true to false ratio is independent of the collection part of either detector, it can be no measure for the quality of the setup.

In case of secondary electron detection from samples of thickness beyond  $\lambda_{\text{esc}}$  the fraction  $f_{\text{SE}}$  as it is used in Eq. (3.66) should not be constant. The yield  $Y_{\text{SE}}$  should not rise linear with thickness  $t$ , but flatten out at some maximum. This can be done by taking  $f_{\text{SE}}$  proportional to  $\lambda_{\text{esc}}/t(1 - e^{-t/\lambda_{\text{esc}}})$ .

A more complete description of the problem should also take into account the fact that more than one atomic species can be present in the sample. Each species brings with it several possible excitation processes which all have their specific cross section. In above relations therefore  $n\sigma$ , for the single as well as the coincidence techniques, should be replaced by a summation over all species (s) and processes (p):  $\sum_{\forall s} \sum_{\forall p} n_s \sigma_{s,p}$ . The simplification that is made by not performing such summation is allowed, provided that at the position in the spectrum where we are looking, only one excitation process for one atomic species is dominant.

#### 3.5.4. Signal-to-Noise Ratio

Improving on the true to false ratio is not always the best way to go. Reducing primary beam current as suggested by Eq. (3.67) would clearly reduce the signal of true coincidences as given by Eq. (3.64). The noise which is accompanied by this, can become a problem. Below the signal-to-noise ratio of the number of true coincidences will be discussed. It is based on measurements where we have two separate time windows. Fig. 3.23 shows how one window of width  $\tau_{\text{tw}}$  is set to accept all true coincidences  $N_T$  during a dwelltime  $T_{\text{dwell}}$ . In total this true window accepts  $N_{\text{tw}}$  counts. The other (false) window of width  $\tau_{\text{fw}}$  accepts just  $N_{\text{fw}}$  false coincidences. The ratio of true to false counts can then be expressed as

$$\frac{R_T}{R_F} = \frac{\tau_{\text{fw}}}{\tau_{\text{tw}}} \frac{N_{\text{tw}}}{N_{\text{fw}}} - 1. \quad (3.68)$$

To determine the number of true coincidences one needs to estimate the amount of false coincidences in the true time window. For this we assume again low count rates ( $R_\alpha \tau \ll 1$  and  $R_\beta \tau \ll 1$ ). Since the false coincidence background is also present outside the true time window, background estimation is possible. The false time window will accept  $\frac{\tau_{\text{fw}}}{\tau_{\text{tw}}}$  times the number of false counts that are collected in the true window  $N_{\text{tw}}$ . Therefore an amount  $\frac{\tau_{\text{fw}}}{\tau_{\text{tw}}}$  times the number of false counts

### 3. Instrumental Aspects of the Coincidence Experiment

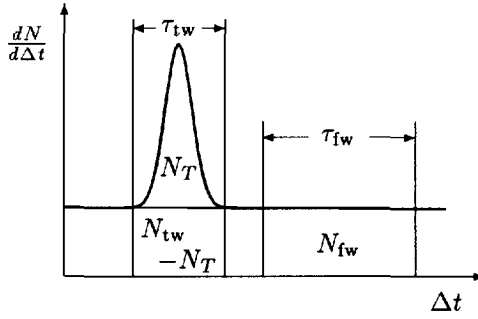


Fig. 3.23: Schematic time-delay spectrum.

in the false window ( $N_{fw}$ ) can be subtracted from the total number of counts in the true window:

$$N_T = N_{tw} - \frac{\tau_{tw}}{\tau_{fw}} N_{fw}. \quad (3.69)$$

The quality of this signal is described by the signal-to-noise ratio. The noise on  $N_T$  is governed by the Poisson noise on  $N_{tw}$  and  $N_{fw}$ . Any uncertainty on the ratio  $\tau_{tw}/\tau_{fw}$  (e.g. due to non-linearity of the time to amplitude conversion) is considered to be a systematic error. It is assumed that this error can be diminished by analysis of suitable (calibration) measurements. Without this assumption the uncertainty would cause a decreased signal-to-noise ratio at high probe currents. The error in estimating the number of true coincidences  $N_T$  is expressed as a standard deviation  $\sigma_{N_T} = \sqrt{\text{Var}(N_T)}$ , which results in a signal-to-noise ratio

$$\frac{N_T}{\sigma_{N_T}} = \frac{N_{tw} - \frac{\tau_{tw}}{\tau_{fw}} N_{fw}}{\sqrt{N_{tw} + \frac{\tau_{tw}^2}{\tau_{fw}^2} N_{fw}}}. \quad (3.70)$$

For the collection of a complete coincidence spectrum over  $N_{\text{total}}$  channels by means of parallel detectors  $\alpha$  and  $\beta$ , each collecting  $N_\alpha$  and  $N_\beta$  adjacent energy channels at a time, the effective dwell time per point in the two-dimensional spectrum is given by

$$T_{\text{point}} = T_{\text{dwell}} N_\alpha N_\beta = \frac{T_{\text{total}}}{N_{\text{total}}} N_\alpha N_\beta, \quad (3.71)$$

where we will assume for simplicity that  $N_{\text{total}}$  is a multiple of  $N_\alpha N_\beta$  and  $T_{\text{total}}$  is the time available for the complete measurement.

When expressed in terms of true and false countrates and the time effectively spent for each measurement point, Eq. (3.70) becomes

$$\frac{N_T}{\sigma_{N_T}} = \frac{\sqrt{R_T T_{\text{point}}}}{\sqrt{1 + \frac{R_F}{R_T} \left(1 + \frac{\tau_{tw}}{\tau_{fw}}\right)}}. \quad (3.72)$$

Substitution of Eqs. (3.63), (3.64) and (3.66) into Eq. (3.72) leads to the following expression:

$$\frac{N_T}{\sigma_{N_T}} = \frac{\sqrt{ntf_\alpha f_\beta T_\alpha T_\beta \eta_\alpha \eta_\beta \sigma_{\text{true}} \frac{I_{\text{probe}}}{e} T_{\text{point}}}}{\sqrt{1 + \frac{nt\sigma_\alpha \sigma_\beta}{\sigma_{\text{true}}} \frac{I_{\text{probe}}}{e} \tau_{\text{tw}} \left(1 + \frac{\tau_{\text{tw}}}{\tau_{\text{fw}}}\right)}} \quad (3.73)$$

A set of  $N_T/\sigma_{N_T}$  against  $I_{\text{probe}}$  curves is shown in Fig. 3.24, for a specific choice

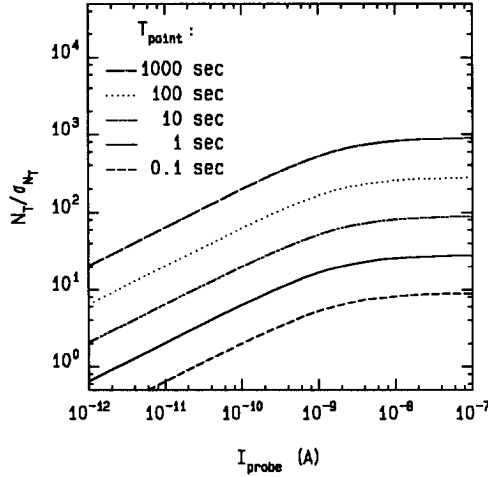


Fig. 3.24: Signal-to-noise ratio  $N_T/\sigma_{N_T}$  as a function of  $I_{\text{probe}}$  for values of  $T_{\text{point}}$  ranging from 0.1 to 1000 seconds. Active values for this graph are  $\tau_{\text{tw}} = \tau_{\text{fw}} = 10 \text{ nsec.}$ ,  $\sigma_\alpha = 1.3 \times 10^{-26} \text{ m}^2$ ,  $\sigma_\beta = 4.14 \times 10^{-26} \text{ m}^2$ ,  $\sigma_{\text{true}} = 1.3 \times 10^{-28} \text{ m}^2$ ,  $n = 100 \text{ nm}^{-3}$ ,  $t = 10 \text{ nm}$ ,  $\eta_\alpha = \eta_\beta = 0.8$ ,  $f_\alpha = 1.0$  and  $f_\beta = 0.8$ .

of instrumental and specimen parameters. The values for cross sections are based on a carbon sample, where one accepts energy losses 34 eV above the carbon  $K$ -shell edge and emitted electrons of 30 eV, with 1-eV energy windows. Each curve represents a different dwell time per point ( $T_{\text{point}}$ ). On the low probe current side of the curves, the slope follows the square root dependence of  $\sqrt{R_T T_{\text{point}}}$  and at the high probe current side the slope approaches zero.

Since a high intensity measurement carried out on a sensitive specimen might be quite effective in changing this specimen, causing so-called radiation damage, there might not be enough time to perform the measurement. For several materials effects have been observed of mass loss of certain atomic species in the specimen as a function of irradiated electron dose. To show the effect of a limited dose on the signal-to-noise ratio,  $T_{\text{point}}$  has been replaced by  $\text{Dose}/I_{\text{probe}}$  in Eq. (3.73). Figure 3.25a shows the signal-to-noise ratio as a function of probe current for several constant dose values. These curves tell that the best signal-to-noise ratio

### 3. Instrumental Aspects of the Coincidence Experiment

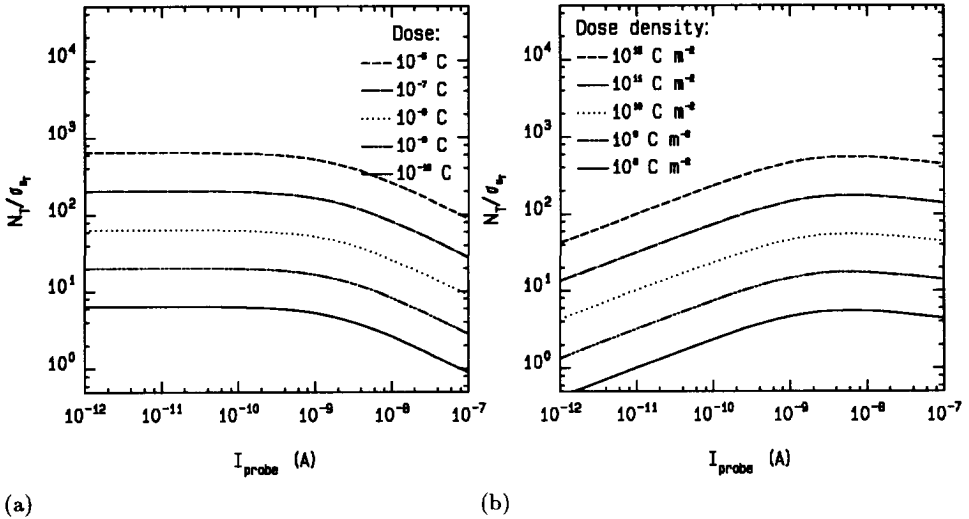


Fig. 3.25: Signal-to-noise ratio  $N_T/\sigma_{N_T}$  as a function of  $I_{\text{probe}}$  (a) for values of the dose ranging from  $10^{-10}$  to  $10^{-6}$  Coulomb and (b) for values of the dose density ranging from  $10^8$  to  $10^{12}$  Coulomb m $^{-2}$ . Chosen parameters are equal to those in Fig. 3.24.

is reached at the lowest possible probe currents, but of course that is after very long dwell times. When both dose and dwell time are limited one should aim for the crossing of the appropriate graphs of Fig. 3.24 and 3.25a.

For some cases it might be more appropriate to assume a maximum dose per illuminated area. Since the (optimized) probesize is a function of probe current (Eq. (3.9)), the signal-to-noise ratio again increases with  $I_{\text{probe}}$ , see Fig. 3.25b.

#### Single Atom Identification

Without any doubt, the most challenging promise of the coincidence techniques is the identification of single atoms. The results of a tentative thought experiment, where a single carbon atom is present in the surface layer of a thin aluminum sample, are presented in Fig. 3.26. In Fig. 3.26a the brightness value of a Schottky field emitter is used for the simulation. For Fig. 3.26b a 100 times smaller brightness value is used, representing for example a  $LaB_6$  cathode. Despite a smaller brightness and therefore smaller probe current, at the larger probe sizes equal signal-to-noise ratios result. In all graphs the probe diameter is computed using the squared summation method (Eqs. (3.1)–(3.10), not ignoring diffraction). The cross sections are based on a selection of energy losses about 34 eV above the carbon  $K$ -edge and an emitted electron energy of 30 eV, both with a 1 eV window. Without a carbon atom present, the chance for an aluminum  $L$ -edge excitation causing the emission of an electron around 30 eV is very small. Only cascade losses

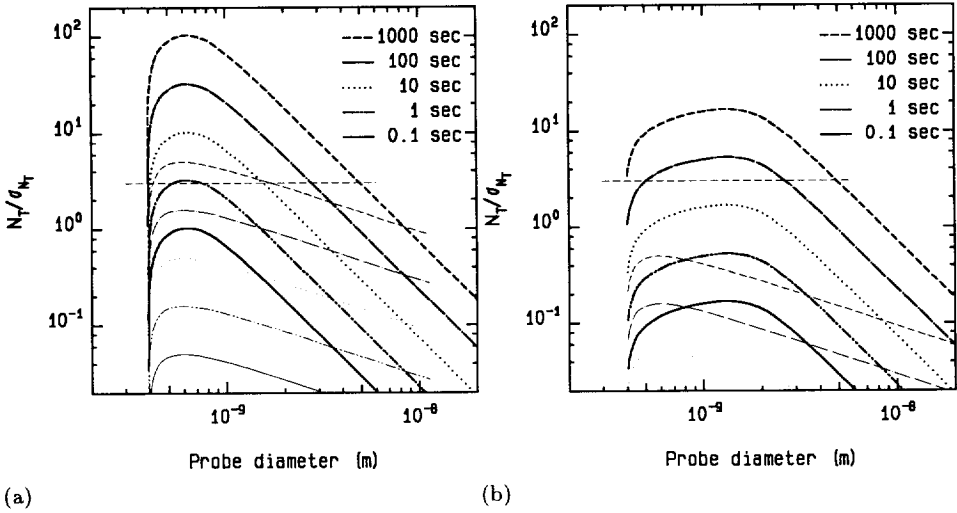


Fig. 3.26: Signal-to-noise ratio for the detection of a single carbon atom on top of a 10 nm thick aluminum sample, for 100 keV primary energy and a 50 mrad acceptance angle, at 318 eV energy loss and 30 eV kinetic energy of the emitted electron, using 1-eV energy windows. Reduced electron source brightness  $B_r$  is (a)  $1.5 \times 10^7 \text{ Am}^{-2}\Omega^{-1}\text{V}^{-1}$ , representing a Schottky field emission gun or (b)  $1.5 \times 10^5 \text{ Am}^{-2}\Omega^{-1}\text{V}^{-1}$ , representing a  $\text{LaB}_6$  cathode. Thick graphs represent the coincidence technique, thin graphs are for regular EELS, at the same energy loss.

might by chance result in an emitted electron with 30 eV kinetic energy. The excitation of a carbon  $K$ -shell electron leads to a virtual-photo electron, in the selected emitted-electron energy band, with a much higher probability.

A signal-to-noise ratio which reaches above 3 for some of the graphs, should be interpreted as the possibility to recognize the feature of the carbon atom in the spectrum with over 99% certainty: *single atom identification*. Even the graph representing a dwell time  $T_{\text{point}}$  of 1 s (for the field emitter), gets above the signal-to-noise ratio of 3.

For a comparison the signal-to-noise data for regular EELS are also shown in Fig 3.26. They have been computed for the same energy loss and show maxima at the smallest probe sizes (limited by diffraction). The signal-to-noise values are at least an order of magnitude smaller, compared to the coincidence technique. The required dose is about 2–3 orders of magnitude higher.

The relative probabilities (energy-differential cross sections) for  $K$ - and  $L$ -shell energy-loss processes for a range of different elements are shown in Fig. 3.27. The cross sections for carbon  $K$ -shell and aluminum  $L$ -shell excitation (and also for other materials) are on the same order of magnitude at or somewhat above the carbon edge. It is obvious that the regular EELS signal from a single atom on top

### 3. Instrumental Aspects of the Coincidence Experiment

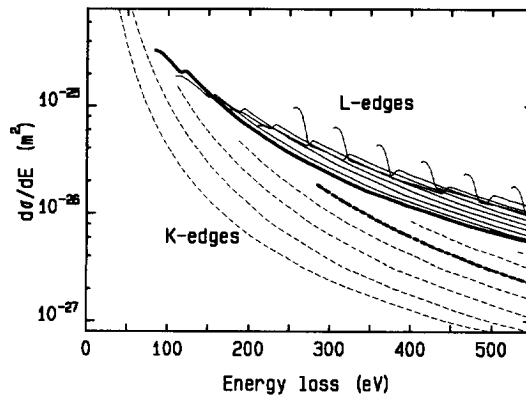


Fig. 3.27: Energy differential cross sections for *K*- and *L*-shell edges. *K*-shell edges (dashed lines) are shown which start with helium and are visible up to oxygen. The *L*-shell edges (solid lines) from aluminum and heavier elements show some extra structure, among other things due to different subshells. Marked with heavier lines are the *K*-shell cross section for carbon and the *L*-shell cross section for aluminum. Data are computed for 100 keV primary electron energy at 100 mrad acceptance angle, using programs SIGMAK2 and SIGMAL2, by Egerton.<sup>10</sup>

of a 10 nm thick sample, illuminated with a probe of nanometer dimensions, is easily drowned in the signal from the many (100–1000) atoms of the bulk.

Because of the separation of the different edges, very high energy resolution seems unnecessary. Elemental identification is still possible with energy windows of 10 eV or even up to 100 eV. By using for example 10 times as wide energy windows in EELS and/or emitted-electron detection, one effectively increases the individual and/or coincidence cross sections with almost the same amount. The result on the signal-to-noise ratio is shown (for a 10 s dwell time) in Fig. 3.28. The effect on the sensitivity for regular EELS is an obvious increase in signal-to-noise ratio. Also for the coincidence technique an increase is observable, however this effect is only important in the low probe current region. Using different resolutions in the two detecting systems is not useful for the virtual-photo electron case discussed here. In case individual Auger lines are selected with the emitted-electron detector, this situation is somewhat changed, and choosing a different energy resolution in each detector can be profitable.

### 3.6. References

- <sup>1</sup> A. Delong, J. Chmelík, V. Kolařík, J. Komůrka and J. Očadlík, *A new design of field emission electron gun with a magnetic lens*, *Optik* **81**, 103 (1989).



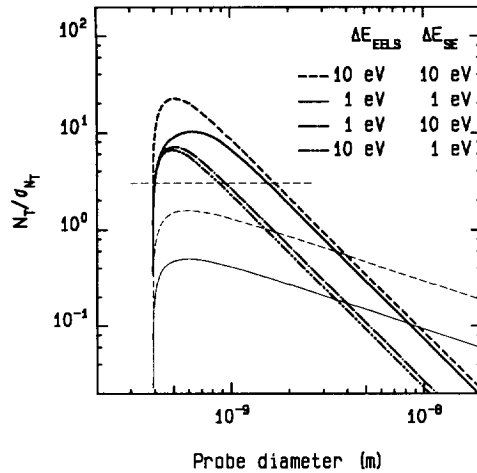


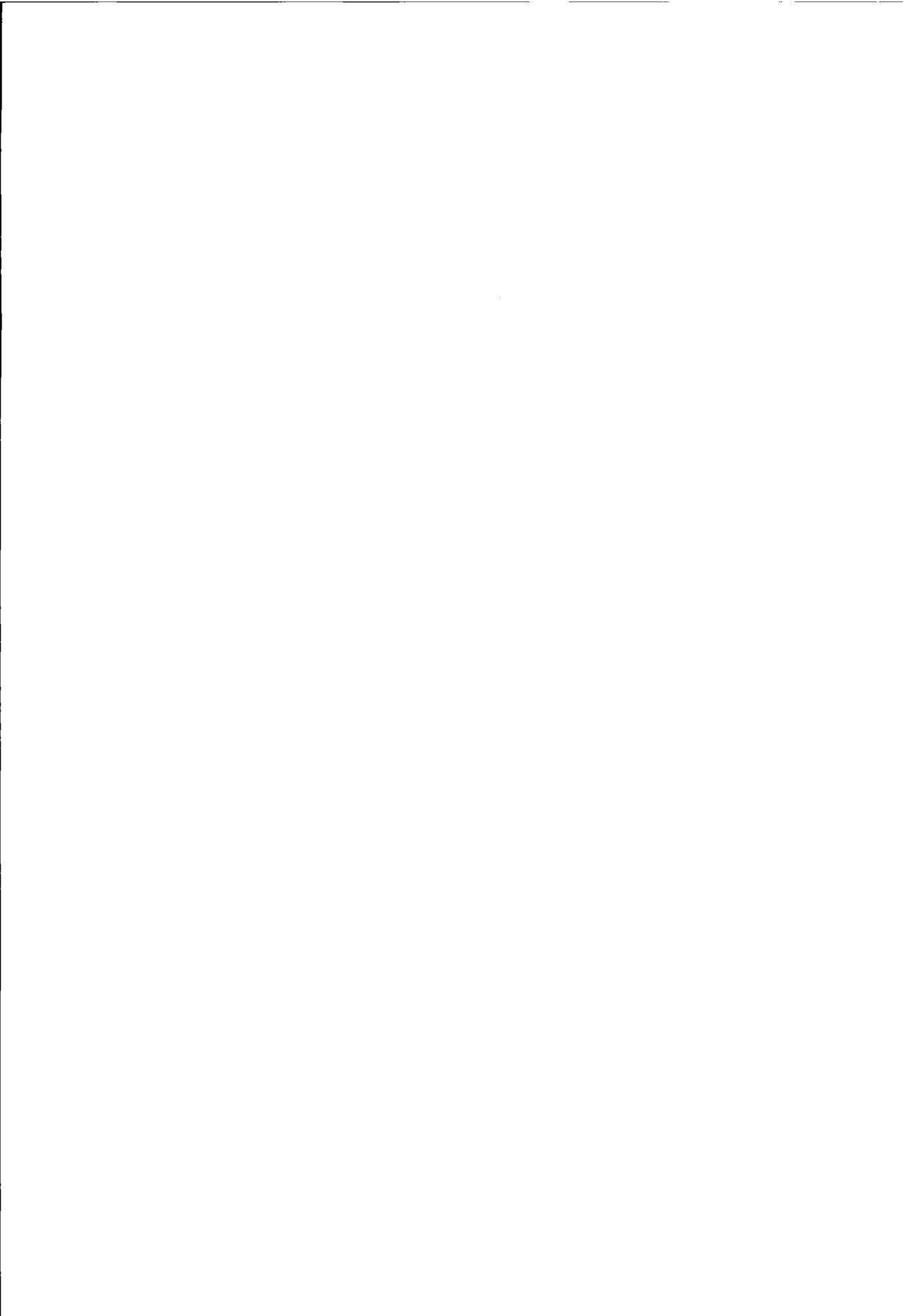
Fig. 3.28: Influence of energy resolution in the two detectors on the signal-to-noise ratio for single atom detection. All graphs are made for  $T_{\text{point}}=10$  s. The case with 1-eV energy resolution in both detectors is equivalent to the graph in Fig. 3.26a. Thin lines apply for the regular EELS case.

- <sup>2</sup> C. Mory-Prunier. *Etude théorique et expérimentale de la formation de l'image en microscopie électronique à balayage par transmission*. PhD dissertation, Université de Paris-Sud, Centre d'Orsay, July 1985.
- <sup>3</sup> L. Reimer, *Scanning Electron Microscopy, Physics of Image Formation and Microanalysis*, Vol. 45 of Springer Series in Optical Sciences. (Springer-Verlag, 1985).
- <sup>4</sup> J. K. Weiss, R. W. Carpenter and A. A. Higgs, *A study of small electron probe formation in a field emission gun TEM/STEM*, *Ultramicroscopy* **36**, 319 (1991).
- <sup>5</sup> M. Born and E. Wolf, *Principles of Optics*. (Pergamon Press, New York, 1985).
- <sup>6</sup> J. J. Vroemen. *A model for calculating and optimization of probe current density distributions*. Master's thesis, Delft University of Technology, Department of Applied Physics, August 1991.
- <sup>7</sup> P. M. Mul, B. J. H. Bormans and M. T. Otten, *Design of the CM20 FEG*, *Electron Optics Bulletin* **130**, 53 (1991).
- <sup>8</sup> P. M. Mul, November 1991, Private communication.
- <sup>9</sup> A. J. Bleeker. *Optical and mechanical design for 1 nm resolution Auger spectroscopy in an Electron Microscope*. PhD thesis, Delft University of Technology, June 1991.
- <sup>10</sup> R. F. Egerton, *Electron Energy-Loss Spectroscopy in the Electron Microscope*. (Plenum Press, New York, 1986).
- <sup>11</sup> B. Chornik, R. Sopizet and C. Le Gressus, *Deconvolution in electron spectroscopy revisited: computational aspects*, *J. of Electron Spectrosc. and Relat. Phenom.* **42**, 329 (1987).
- <sup>12</sup> P. E. Batson, *Prospects for high-resolution electron energy-loss experiments with the scanning transmission electron microscope*, *Ultramicroscopy* **18**, 125 (1985).
- <sup>13</sup> J. Fink, *Recent Developments in Energy-Loss Spectroscopy*, Vol. 75 of *Advances in*

### 3. Instrumental Aspects of the Coincidence Experiment

- Electronics and Electron Physics*, p. 121. (Academic Press, Inc., London, 1989).
- <sup>14</sup> A. J. Koster. *Autotuning of a Transmission Electron Microscope*. PhD thesis, Delft University of Technology, June 1989.
  - <sup>15</sup> P. Kruit and H. Shuman, *The influence of objective lens aberrations in energy-loss spectrometry*, *Ultramicroscopy* **17**, 263 (1985).
  - <sup>16</sup> H. Shuman and P. Kruit, *Quantitative data processing of parallel recorded electron energy-loss spectra with low signal to background*, *Rev. Sci. Instrum.* **56**, 231 (1985).
  - <sup>17</sup> R. F. Egerton and P. A. Crozier, *A compact parallel-recording detector for EELS*, *J. of Microscopy* **148**, 157 (1987).
  - <sup>18</sup> O. L. Krivanek, C. C. Ahn and R. B. Keeney, *Parallel detection electron spectrometer using quadrupole lenses*, *Ultramicroscopy* **22**, 103 (1987).
  - <sup>19</sup> O. L. Krivanek, T. Manoubi and C. Colliex, *Sub-1 eV resolution EELS at energy losses greater than 1 keV*, *Ultramicroscopy* **18**, 155 (1985).
  - <sup>20</sup> J. J. Livingood, *The Optics of Dipole Magnets*. (Academic Press, New York, 1969).
  - <sup>21</sup> P. Kruit and J. A. Venables, *High-spatial-resolution surface-sensitive electron spectroscopy using a magnetic parallelizer*, *Ultramicroscopy* **25**, 183 (1988).
  - <sup>22</sup> P. Kruit, *Magnetic Through-the-lens Detection in Electron Microscopy and Spectroscopy, Part 1*, Vol. 12 of *Advances in Optical and Electron Microscopy*, p. 93. (Academic Press Limited, London, 1991).
  - <sup>23</sup> A. J. Bleeker and P. Kruit, *The magnetic parallelizer as an optical element for Auger electrons: Further characterization*, *Nucl. Instrum. Methods A* **298**, 269 (1990).
  - <sup>24</sup> P. Kruit and F. H. Read, *Magnetic field paralleliser for  $2\pi$  electron-spectrometer and electron-image magnifier*, *J. Phys. E* **16**, 313 (1983).
  - <sup>25</sup> H. W. G. van der Steen, J. E. Barth and J. P. Adriaanse, *Engineering constraints and computer-aided optimization of electrostatic lens systems*, *Nucl. Instrum. Methods A* **298**, 377 (1990).
  - <sup>26</sup> M. A. J. van der Stam, J. E. Barth and P. Kruit. *Design of a multi-mode transport lens with optimization program SOEM*, To be published.
  - <sup>27</sup> R. E. Imhof, A. Adams and G. C. King, *Energy and time resolution of the  $180^\circ$  hemispherical electrostatic analyser*, *J. Phys. E* **9**, 138 (1976).
  - <sup>28</sup> P. Hayes, M. A. Bennett, J. Flexmann and J. F. Williams, *Position sensitive detectors in (e, 2e) coincidence measurements*, *Rev. Sci. Instrum.* **59**, 2445 (1988).
  - <sup>29</sup> W. P. Poschenrieder, *Multiple-focusing time-of-flight mass spectrometers: Part II. TOFMS with equal energy acceleration*, *Int. J. Mass Spectrom. Ion Phys.* **9**, 357 (1972).
  - <sup>30</sup> M. Völkel and W. Sandner, *Optimisation of electron energy analysers for application in coincidence experiments*, *J. Phys. E* **16**, 456 (1983).
  - <sup>31</sup> J. L. Wiza, *Microchannel plate detectors*, *Nucl. Instrum. Methods* **162**, 587 (1979).
  - <sup>32</sup> *Hamamatsu MCP product info*. Shipped with MCP's, 1992, Hamamatsu Photonics, Electron Tube Division, Shimokanzo, Japan.
  - <sup>33</sup> L. J. Richter and W. Ho, *Position-sensitive detector performance and relevance to time-resolved electron energy loss spectroscopy*, *Rev. Sci. Instrum.* **57**, 1469 (1986).
  - <sup>34</sup> P. E. Batson, *Parallel detection for high-resolution electron energy loss studies in the scanning transmission electron microscope*, *Rev. Sci. Instrum.* **59**, 1132 (1988).
  - <sup>35</sup> J. S. Faber. *Possibilities for parallel detectors in coincidence measurements*. Master's thesis, Delft University of Technology, Department of Applied Physics, July 1991.
  - <sup>36</sup> R. P. Tornow, *A new method to measure and increase the detection efficiency of a*

- microchannel plate for 100 keV electrons*, Meas. Sci. Technol. **1**, 576 (1990).
- <sup>37</sup> H. C. Wijnaendts van Resandt, H. C. den Harink and J. Los, *A position dependent particle counter using microchannel plates*, JPE **9**, 503 (1976).
- <sup>38</sup> *Texas Instruments Linear Circuits: Data Acquisition and Conversion Data Book*, Vol. 2. (Texas Instruments, Dallas, Texas, 1989), TLC 550 flash 8-bit analog-to-digital converter.
- <sup>39</sup> Burr-Brown, Tucson, Arizona. *ADS 7810 12-bit successive approximation analog-to-digital converter*.
- <sup>40</sup> *Burr-Brown Integrated Circuits Data Book*, Vol. 33. (Burr-Brown, Tucson, Arizona, 1989), DIV 100 analog divider.
- <sup>41</sup> *Burr-Brown Integrated Circuits Data Book*, Vol. 33 C. (Burr-Brown, Tucson, Arizona, 1993), MPY 600 analog multiplier.
- <sup>42</sup> P. Kruit, W. Th. Wenckebach and C. W. E. van Eijk. *(Coincidence) electron spectroscopy with nanometer scale resolution*, unpublished project proposal, 1991.
- <sup>43</sup> J. Westerman. *Realisatie van een meetprogramma met behulp van transputers ten behoeve van het coincidentie elektronen microscoop projekt*, unpublished report, 1992.
- <sup>44</sup> EG&G ORTEC, Silicon Valley, California. *Model 567 Time-to-amplitude Converter / Single-Channel Analyzer Operating and Service Manual*.



## 4. Setup of the Prototype Experiment

The coincidence experiments discussed in the previous chapters cannot routinely be performed on commercially available electron microscopes today. However, many requirements for coincidence experiments are already met in these instruments. We therefore decided to base our experiments on a modified version of a commercial instrument. Before designing a fully-featured UHV instrument we started experiments on a non-UHV instrument. Main purpose of the non-UHV instrument was to get experience with the optical system for the extraction and analysis of the secondary and Auger electrons, and with spectroscopy and coincidence techniques. This experience was intended to help in the design of the UHV instrument. Several shortcomings of the non-UHV instrument, like contamination and loss of spatial resolution were taken for granted.

The non-UHV prototype on which all experiments of this work have been performed is based on a standard transmission electron microscope with scanning attachment. This instrument is modified for emitted-electron analysis and equipped with an electron energy-loss spectrometer. Additional fast electronics is available to establish the coincidence experiment. A personal computer is used for data processing and storage.

A description of the prototype experimental set-up will be given here, first showing the modifications of the column and their influence on the primary beam. The specifications of the emitted-electron analyzer are followed by a description of the modifications made to the EELS spectrometer. Following that, some details of the coincidence electronics are given. The specimens that have been used are briefly described. Finally some general comments are given on experimental difficulties which have been encountered.

### 4.1. Microscope Column

The microscope is the (old) prototype of the EM400 series of Philips. Apart from minor modifications, the gun section (with hairpin tungsten emitter), the two condenser lenses and the magnification system are in their original state (Fig. 1.1). To perform the emitted-electron extraction a major modification was required.

An 180-mm extension was inserted between the second condenser and the objective lens. The emitted electrons are to be guided through the upper half of the objective lens into the extension where they are deflected over  $90^\circ$ . They then

#### 4. Setup of the Prototype Experiment

leave the extension through one of several vacuum ports, connected to the analyzer. To make this possible the upper half of the objective lens is furnished with an extra coil, placed inside the bore of the upper half of the objective lens. The field of this so-called parallelizator coil ends at a magnetic aperture just above the mechanical top of the objective lens. A 20-mm radius electrostatic hemispherical deflector directs the emitted electrons toward the detector. To enable the detection of different emitted-electron energies, without changing the voltage across the 90° deflector, the deflector entrance and exit apertures, the magnetic aperture (plus a short tube extending downwards from it) and the specimen holder are insulated from the rest of the column. The latter is done by mounting the grid holding part of a side-entry specimen holder on an insulated version of the objective-aperture holder. Adjustments on the objective aperture holder can shift the specimen in the two lateral directions and also along the microscope axis. The original specimen stage and objective aperture are removed. To let the primary electrons go through the 90° deflector, a small hole is drilled in the outer hemisphere and a little tube is fitted on top of it.

An extra set of deflectors was added directly underneath the second condenser lens. This is done because scanning in the upper half of the objective lens would influence the emitted electrons too much. The extra set is excited with a permanent offset to give some compensation for the deflection the primary electrons are subjected to in the 90° deflector.

All these modifications have some influence on the probe forming characteristics. First of all there is the extra length between the second condenser and the objective lens. Together with the modified shape of the axial field in the objective lens caused by the addition of the parallelizator coil, this requires a different setting of the condenser system. The demagnified gun image formed by the first two condensers must be imaged on the specimen by the objective lens pre-specimen field. The post-specimen field must then form an image of the specimen on the selected-area plane, which is further imaged by the magnification system. The pre- and post-specimen fields cannot be excited independently. A given specimen position requires a certain objective-lens excitation, thereby prescribing the position of the plane where the two condensers must form the gun image. As a consequence of the the modified column the smallest probe sizes are no longer available, and the achievable probe current in the larger probe sizes is smaller.

The 90° deflector has as important side effect a displacement of the spot over the sample. The displacement is corrected by placing a suitable offset on the extra set of deflectors. The resulting effect consists of two- and threefold astigmatism, of which the twofold astigmatism is easily compensated by adjustment of the condenser stigmator. The remaining threefold astigmatism can be clearly seen when moving through focus by adjusting the second condenser lens current.

Other effects of the extension are the increased sensitivity to (magnetic) stray fields and mechanical vibrations. The deflector and the empty space above it are shielded from magnetic stray fields by a mu-metal cover. However, some residual

effect of stray fields and vibrations could be observed at the smallest probe sizes.

As a result of the non-ideal lens distances and the effect of three-fold astigmatism the smallest probe size achievable, with a condenser aperture of  $30\ \mu\text{m}$  is about  $100\ \text{nm}$ , with a probe current of about  $2\ \text{pA}$ . Other measured values are shown in table 4.1. Probe sizes are larger by approximately two orders of magni-

Table 4.1: Measured probe current and probe size as a function of condenser aperture and first condenser lens setting.

$I_{\text{cond.1}}$ (A)	$d_{\text{aperture}}$ ( $\mu\text{m}$ )	$I_{\text{probe}}$ (pA)	$d_{\text{probe}}$ ( $\mu\text{m}$ )
0.46	500	5500	10
0.46	100	1500	5
0.46	30	500	3
2.14	500	700	4
2.14	100	30	0.8
2.14	30	2	0.1

tude compared to standard STEM probe sizes. For EELS the collection angle or energy resolution will be affected if the probe size becomes comparable in size to the chromatic or spherical aberration of the post-specimen section (Fig. 3.5). For emitted-electron analysis the transmission or energy resolution will be affected if the probe size is comparable with or larger than the Larmor radius in the magnetic field at the specimen (see 3.3). For both EELS and emitted-electron analysis, the smallest available probe sizes do not yet influence energy resolution or transmission. The loss of spatial resolution is taken for granted.

The vacuum system required some modifications as well. There has been made a connection between the extension and the ion getter pump and there is now a longer connecting tube between the gun section and the ion getter pump. The ion getter pump does however not function properly. To improve the vacuum level near the specimen a  $751/\text{s}$  turbo molecular pump has been added on one of the ports at the specimen level. The vacuum obtained with this pump, plus the standard oil diffusion pump is about  $10^{-4}\ \text{Pa}$ .

#### 4.1.1. Emitted-Electron Analyzer

The emitted-electron analyzer has a central radius of  $140\ \text{mm}$ . During most experiments the pass energy inside the hemispherical analyzer is kept constant at  $100\ \text{eV}$ . The inner and outer hemisphere have a radius of  $112\ \text{mm}$  and  $165\ \text{mm}$  respectively. Slitwidths at entrance and exit plane of the analyzer can vary from  $0$  to  $20\ \text{mm}$ . A MCP placed at about  $10\ \text{mm}$  from the exit slits is used as a (single channel) electron detector. A phosphor screen behind the MCP is used for visual

#### 4. Setup of the Prototype Experiment

feedback, in adjusting the settings of the analyzer and the transfer optics. In situations where not enough light was available, the phosphor was displayed by means of a low-light-level video camera.

The transfer optics consisted of ten 20-mm long, 20-mm diameter cylinders, connected to several adjustable (positive or negative) power supplies (0–5 kV).

##### 4.1.2. Electron Energy-Loss Analyzer

A magnetic sector analyzer, a Gatan 607,<sup>1</sup> is mounted at the end of the microscope column, after the microscope magnification system. The post specimen lenses can be set up in an image or diffraction pattern coupled mode, with variable magnification or cameralength. This enables different choices for the size of collection angle and analyzed sample area, limited by the post specimen lens aberrations; see, e.g., Kruit and Shuman.<sup>2</sup>

The EELS spectrometer is normally used with fairly large beam currents. For coincidence measurements one must be able to reduce the beam current to minimize false coincidences. Spectrum acquisition can therefore take much more time. The demands for stability on the EELS spectrometer and on the high-voltage supply of the microscope are consequently also more stringent. In a non-airconditioned room in our laboratory the temperature changes several degrees over a working day, caused by outside temperature changes and changes in the amount of equipment that is switched on. Local draughts and equipment heating cause changes in the current supply for the sector magnet, that are equivalent to several eVs. To overcome this problem a temperature control circuit is used, in thermal contact with the reference resistor of the current supply. This makes the magnet stable to an equivalent of a few tenths of an eV.

Remaining drifts are attributed to the slow changes in temperature of the reference resistors of the microscope high-voltage supply, inside the oil-filled isolation tank. With the room air-conditioned and the high-voltage supply switched on for a few hours the observed over-all spectral drift is less than 1 eV per 10 min. For most experiments this value is acceptable, since the intrinsic width of the zero loss peak in the spectrum is of the same order, and spectra which require more time to be gathered, can be split in separate parts with intermediate recalibration of the spectrum by hand without a significant loss of time.

#### 4.2. Coincidence Electronics

To perform the coincidence measurements, electrical pulses from the anode behind the MCP and from the PMT of the EELS detector are led toward a time-to-amplitude converter (TAC) (EG&G Ortec, model 567). Because the anode behind the MCP is at several kilovolts, an isolation transformer is used to bring the signal to ground level. A twisted pair of teflon coated wire-wrap wires, that have been tested to withstand voltage differences of over 5 kV, is wound several times around a ferrite coil, to give good high-frequency behavior.



A damping resistor in the line prevents reflections, at the cost of some signal amplitude. Because of the small signal a preamplifier is mounted almost directly behind the transformer (EG&G Ortec, model VT110 B). A  $50\ \Omega$  coaxial cable then leads the signal to a constant-fraction discriminator (EG&G Ortec, model CF4000). The pulses from the MCP have a total duration of about 50 nsec, and a risetime of about 15 to 20 nsec. Simple (constant-level) discrimination might lead to timing differences on the order of 5 to 10 nsec for different amplitudes of the MCP pulses. The use of a constant-fraction discriminator does not lead to timing inaccuracies, as long as the shape of the pulses is independent of the amplitude.

The EELS photomultiplier has a built-in preamplifier and constant-level discriminator. The ECL output signal of this discriminator runs from the spectrometer to the EELS control unit over a twisted wire pair. In the control unit a  $50\ \Omega$  line driver has been added, from which the signal is sent directly toward the time to amplitude converter. A possible improvement here would be the use of a constant-fraction discriminator, instead of the constant-level discriminator, although total pulse duration here is already on the order of 20 nsec. Total timing accuracy obtained in the coincidence measurements was 2.1 nsec FWHM (see Fig. 5.5). Comparison of measured time resolution with computed values (Fig. 3.8) suggests an analyzer acceptance angle of about 65 mrad.

The amplitude output of the TAC is led to a multi-channel analyzer (MCA) (consisting of a Canberra, model 8075 analog-to-digital converter, and a CMTE multichannel dataprocessor, with PC-interface). Dedicated software was developed to conveniently collect and manipulate the MCA data.

### 4.3. Specimens

During the experiments only a few different samples have been used. Because of the bad vacuum conditions, the top surface is expected to be covered with adsorbed residual gas molecules. In a column pumped with an oil diffusion pump the residual gas consists mainly of carbon compounds. The analyzed surface layer in this microscope is therefore expected to be mainly carbon. With the choice of an amorphous carbon thin foil as sample, the difference between bulk and surface material seems least critical.

Several attempts have been made to look at different elements. A thinned aluminum sample<sup>†</sup> was tried, but spectra changed quite fast from being almost pure aluminum(-oxide) to carbon-covered aluminum, under influence of the electron beam. A cone of carbon grows on the surface(s) of the aluminum. This same effect was also observed on the carbon films, but there it did not (visibly) change the composition of the sample.

To look at more different materials also sputter coated carbon films were examined. They have been prepared in a simple sputter coater in our laboratory.

†. Courtesy Mr. de Haan, Material Science Department

#### 4. Setup of the Prototype Experiment

Elements which were tried are silver, gold, and aluminum. Unfortunately the secondary/Auger electron spectra did not show appreciable signs of these elements. Expected improvements in coincidence techniques might ask for tests on these samples, but since the outer layer will be covered with carbon again, it will be hard to see anything in coincidence spectra if the original surface is not showing any interesting Auger peaks at all. Coincidence spectra on these samples did not show noticeable differences from the spectra on the pure carbon thin foils.

#### 4.4. Experimental Difficulties

Realization of coincidence spectroscopy in an existing electron microscope is certainly not trivial. Since the settings of the microscope itself, illumination and magnification system, as well as both analyzer systems must be matched well, a thorough understanding of the complete instrument is required. For example, on a large instrument as an electron microscope with lots of electronic circuitry the realization of single pulse counting requires low electric and electromagnetic noise levels and well-defined electrical ground levels (or better *one* ground level). Coupling of the coincidence electronics to a data processing computer even increases such problems.

The modifications to the vacuum system of the microscope have not been designed with UHV conditions in mind. In addition to the direct influence of contamination of specimen surfaces we observed degradation of detector performance. Since no extra pumps have been used for the evacuation of the concentric hemispherical analyzer, the vacuum at the position of the MCP was only on the order of  $10^{-3}$  Pa. Normally a vacuum of better than  $10^{-4}$  Pa is recommended to prevent ion feedback in the MCP channels. Positive ions are accelerated to the front of the MCP, where they release new secondary electrons, which causes an exponentially decaying background in the pulse height distribution. A compromise between large amounts of background counts and good detection efficiency should then be made, by selecting an optimum discriminator setting.

Before operation, the MCP should be carefully conditioned (by applying a slowly rising bias voltage, and preferably baking at high temperature) to prevent large amounts of ions to be released, which could cause permanent damage to the MCP; see, e.g., Norton *et al.*<sup>3</sup> In our situation baking was not possible (and at the available vacuum level, probably also not very useful). In the high-voltage supply lines for the MCP 'pickup transformers' were used which provided an indication of small discharges during initial conditioning. If the power of the discharges exceeded a certain threshold, the voltage was automatically removed from the MCPs.

Since the emitted electrons from the specimen do not form a monochromatic beam, the adjustment of the optical elements in the path of the emitted electrons, is quite complicated. Optimum settings for lenses, parallelizator, slits,  $90^\circ$  deflector and  $180^\circ$  analyzer supplies were found by manual adjustments, starting from

pre-computed settings. The adjustments made by the operator are based on interpretation of a combination of several sources of information. First of all there is the image which is visible on the phosphor screen behind the MCP. If enough signal is available, this image shows (or should show) a vertical band, signifying the spectrum, dispersed by the hemispherical analyzer. The effect of the slitwidths can be seen in the vertical direction. The width of the band is a measure for the spotsize at the analyzer entrance.

Most other information is found in the shape and intensity of emitted-electron, coincidence and time-delay spectra. From the shape of the emitted-electron spectrum the energy resolution and beamshape at some points in the optical path can be deduced. The intensity of the spectra tell something about the collection efficiency. The width and growth-rate of the true-coincidence peak in the time-delay spectrum is a good monitor for complete system performance.

Of course, before the information from coincidence and time-delay spectra can be used, the energy-loss analyzer should be optimized first. Normally this can be done independent from the emitted-electron analysis system, apart from some small displacement and focussing effects which occur if the 90° deflector and parallelizator are readjusted.

It may be obvious that optimizing the complete prototype instrument for good coincidence performance is a slow process, which requires many iterations. However, once some good basic settings were found it turned out to be possible to do some minor final adjustments (with some *Fingerspitzengefühl*), in relatively short time.

## 4.5. References

- <sup>1</sup> Gatan Inc., Pleasanton, California. *Instruction Manual for Electron Energy Loss Spectrometer Model 607*.
- <sup>2</sup> P. Kruit and H. Shuman, *The influence of objective lens aberrations in energy-loss spectrometry*, *Ultramicroscopy* **17**, 263 (1985).
- <sup>3</sup> T. J. Norton, R. W. Airey, B. L. Morgan, P. D. Read and J. R. Powell, *A 40 mm MCP Intensifier for Photon Counting*, Vol. 74 of *Advances in Electronics and Electron Physics*, p. 41, in *Photo-Electronic Image Devices*, edited by P. W. Hawkes. (Academic Press, London, 1988).



## 5. Results of the Measurements<sup>†</sup>

### Abstract

The ultimate resolution in secondary-electron images, obtained in a scanning transmission electron microscope depends strongly on secondary-electron-production mechanisms. In such a microscope, equipped with an electron-energy-loss spectrometer as well as a secondary-electron-energy analyzer, coincidences have been achieved between secondary electrons and energy-loss electrons. This has resulted in additional information on the origin of secondary electrons in thin carbon films. The average probability for the production of secondary electrons of a given kinetic energy rises linearly with the energy lost by the primary electrons minus this kinetic energy and a few eV. These secondary electrons seem to appear from a cascade which was started by the original energy-loss event. Since most of these events are volume-plasmon excitations, volume-plasmon decay followed by a cascade contributes strongly to the secondary-electron emission. The linear relation seems to break down at energy losses of more than  $\approx 125$  eV. Energy losses associated with surface plasmons give a high probability for emission and detection of secondary electrons with a kinetic energy of 2–3 eV. For losses which are about 11 eV higher than the kinetic energy of the secondary electrons, an enhanced probability of emission exists. This enhancement is attributed to direct ionization from the valence band. The results are obtained in non-ultrahigh-vacuum conditions but show one of the many possibilities of coincidence spectroscopy in a scanning transmission electron microscope.

### 5.1. Introduction

The impact of a primary electron on a specimen in the electron microscope can cause several scattering events. If more than one scattering product is detected, additional information on the scattering event and thus on the specimen can be extracted. Coincidence techniques are required to find out which scattering products belong together. They rely on the fact that the creation of a secondary particle by an energy-loss process of the primary electron occurs almost immediately. We report on preliminary coincidence experiments between secondary electrons and

<sup>†</sup> The text of this chapter has been published in *Phys. Rev. B*, Vol. 44, No. 17, 1 November 1991-I, p. 9192–9200, under the title: ‘Detection of energy-selected secondary electrons in coincidence with energy-loss events in thin carbon foils’, by Folbert J. Pijper and Pieter Kruit.

## 5. Results of the Measurements

the transmitted energy-loss electrons. The results are preliminary since only in a later stage ultrahigh-vacuum (UHV) conditions, high spatial resolution and other energy ranges will be available. Nevertheless, these results give indications on the origin of secondary electrons. Before describing the experiment and the results we shall give a short review of related coincidence work.

Most early coincidence spectroscopy studies were performed on gases. Van der Wiel and Brion<sup>1</sup> have reported on so-called near-dipole ( $e, 2e$ ) spectroscopy experiments, which rely on the similarity with photo electron spectroscopy, or the theoretical correspondence between photon- and electron-induced excitations; see, e.g., Jackson.<sup>2</sup> The significance of ( $e, 2e$ ) spectroscopy or any coincidence spectroscopy in which the electron-energy-loss spectroscopy (EELS) signal is involved, is best understood if we interpret the absorption of energy from the primary electron as a virtual photon: by the impact of the primary electron the secondary electron can obtain a kinetic energy, equal to the difference of the energy loss and its original binding energy.

Coincidence spectroscopy has been used by Ungier and Thomas<sup>3</sup> to decompose the Auger spectrum in specific Auger decay processes, by acquiring the Auger electrons in coincidence with certain well-defined energy losses.

If both energy and direction of the scattering products is available, the original momentum distribution of the ejected electrons can be found. Normally this is done with lower primary energies and consequently larger scattering angles. McCarthy and Weigold<sup>4</sup> have reviewed studies aimed at the reconstruction of this distribution. Most of these experiments are done on gases, some on solids.

The study of solids has always been more complicated. In a solid, before escaping from the surface, an unknown amount of energy can be lost in a "cascade" of subsequent scattering events. Besides this, the workfunction must be overcome. Some electrons of the original energy distribution will have moved toward the low-energy part of the spectrum; others will not escape.

Haak *et al.*<sup>5</sup> used Auger-photoelectron coincidence spectroscopy (APECS) to study solids. The energy of the (x-ray excited) photoelectron defines the intermediate state in the Auger process. The decay from these states shows up in the APECS spectrum.

Ritter, Dennison, and Jones<sup>6</sup> measured the spectral momentum density of the valence band of amorphous carbon by ( $e, 2e$ ) spectroscopy, using 25-keV electrons and scattering angles close to 45°. Two separate bands (energy against momentum transfer) were distinguished. One band extends from 10 to 23 eV; the other is situated at about 9-eV binding energy. This indicates the possible occurrence of different bonding types between the carbon atoms in the film. More recent work by Gao *et al.*<sup>7</sup> and Hayes and co-workers<sup>8,9</sup> on evaporated carbon, graphite and aluminum (oxide) films give good support for theoretical momentum density calculations (local-density approximation). Due to low incident electron energy the data are strongly influenced by multiple scattering effects.

The scanning transmission electron microscope or STEM, has proven to be a

powerful instrument which can combine many analytical techniques. Coincidences between x rays and energy-loss events were established in a STEM by Kruit, Shuman and Somlyo<sup>10</sup> and showed the possibility of background reduction in the x-ray spectrum and the energy-loss spectrum. Unfortunately an energy-dispersive x-ray detector collects x-rays from only a limited solid angle. Together with the fact that such a detector is relatively slow, this kept them from using high count rates and therefore led to poor statistics.

Also in a STEM, Voreades<sup>11</sup> collected secondary electrons in coincidence with energy-loss events, but energy selection of the secondary electrons was not possible. Wittry<sup>12</sup> suggested to perform such energy analysis and detect specific Auger electrons in coincidence with primary electrons that have lost just enough energy to create the required inner shell hole. Compared with normal Auger spectroscopy, the coincidence detection will yield only slightly fewer counts in the Auger feature, since all emission processes of Auger electrons must be preceded by such energy losses. The background under such an Auger feature is expected to be much more reduced, since it is normally composed of tails of other Auger transitions and the secondary electron contribution from higher-energy losses, which are not selected. An equally interesting application is the idea of reducing the high background in EELS spectra in a similar way. From an increased signal to background ratio an improvement in detection limits might be expected, provided that the spectra are still statistically useful; cf., Cazaux.<sup>13</sup>

In high spatial resolution STEM instruments, the magnetic field required for the fine focusing of the electron probe limited the possibility of extracting secondary electrons from the specimen and performing energy analysis on them. High collection efficiency for secondary electrons becomes possible at high spatial resolution with the introduction of the magnetic parallelizer objective lens; see, e.g., Kruit and Venables.<sup>14</sup> A deflector is required for separating the secondary electrons from the primary beam. The secondary electrons can then be led to an external energy analyzer.

For statistically interesting coincidence results high collection efficiency in both detectors is required. At high primary beam energies the scattering involved in the energy-loss process is confined to small scattering angles. In combination with the large range of angular demagnifications available in the STEM (necessary to ensure good matching with the analyzer), this implies that for EELS in STEM high collection efficiency is possible.

The availability of energy selection for the secondary electrons opens up many interesting possibilities for coincidence techniques. The simplest possibility discussed here, employs coincidences between energy selected secondary electrons and EELS events. Such a coincidence technique yields surface sensitive EELS information, since secondary electrons have only a very short mean free path, (on the order of a few nanometers). This implies the requirement of UHV conditions, something we do not have (yet). The technique can be useful for studying the (valence) band structure. Furthermore it is of interest to determine the origin of

secondary electrons.

The fact that very-high-resolution scanning images have been obtained using secondary electrons,<sup>15</sup> seems to contradict the delocalization that can be expected for the excitation of low energy (large wavelength) secondary electrons.<sup>15-17</sup> One might circumvent the problem of delocalization by observing secondary electrons only if they are accompanied by primary electrons that have lost a certain minimum amount of energy or have scattered more than a minimum scattering angle. More knowledge on secondary-electron-production mechanisms could help in explaining the observed results. A mere comparison of secondary electron information with other modes of operation of the STEM as Liu and Cowley<sup>16</sup> suggested, will prove useful but only in an indirect way. Experiments which show what energy losses are responsible for the production of secondary electrons of certain energy, are expected to tell us more about the creation mechanisms. Voreades<sup>11</sup> collected secondary electrons in coincidence with energy-loss events, but due to the lack of energy selection for the secondary electrons he was unable to tell what production mechanisms take place. From measurements on carbon films of different thicknesses he concludes that secondary electrons are predominantly produced as a result of energy losses of about 20 eV. To decide if this happens as a result of volume plasmon decay (Gorny<sup>18</sup>) or as a result of interband transitions (Willis, Fitton, and Painter<sup>19</sup>), he implicitly suggests the use of energy selection on the secondary electrons. Gorny and Makarova<sup>20</sup> interpreted his data in terms of the decay of volume and surface plasmons, resulting in secondary-electron emission. Surface-plasmon decay dominated for thin samples, whereas volume-plasmon decay dominated for thicker samples.

This article reports on experimental coincidences between energy-selected secondary electrons and energy-selected energy-loss events. The data presented here are considered to be preliminary results of our research toward new instrumentation for high-resolution surface analysis. They have been obtained with a (S)TEM, which is equipped with a secondary-electron analyzer, an EELS detector and some additional coincidence electronics. This instrument has been used as an electron optical test bench for a new (scanning) Auger microscope and works at an operating pressure of  $10^{-4}$  Pa. In this vacuum any specimen is contaminated almost immediately with carbon. A thin amorphous carbon film is chosen as specimen. This way we minimize elemental changes, but we cannot avoid structural changes. One should be aware of the limitations this imposes on some of the data.

### 5.2. Experimental Setup

The experiments described here have been performed on a modified Philips EM 400, which has been described before.<sup>14,21</sup> Figure 5.1 shows the microscope in which the magnetic objective lens is equipped with a parallelizer coil, designed to produce a gradually decreasing field. This field focuses the primary (80-keV) electrons on the specimen, which is located in the high-field region. The secondary electrons,



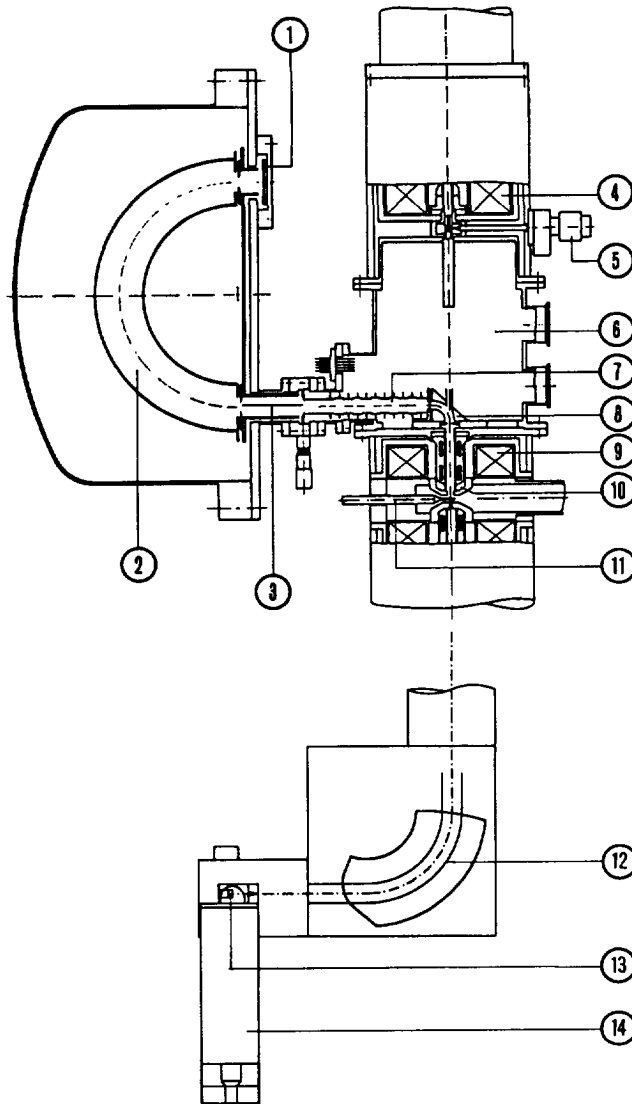


Fig. 5.1: Microscope column used for coincidence measurements.

(1) Micro-channel-plate detector, (2)  $180^\circ$  analyzer, (3) beam defining slits, (4) second condenser lens, (5) condenser diaphragm, (6) microscope extension, (7) electrostatic lenses, (8)  $90^\circ$  deflector, (9) objective lens, (10) parallelizer coils, (11) specimen holder, (12) EELS spectrometer, (13) scintillator, and (14) photomultiplier.

## 5. Results of the Measurements

which can be emitted with large angles with the optical axis, are forced to move to the low-field region. In the low field they move much more parallel to the optical axis, and they are guided through a magnetic aperture that ends the field. The principle of the magnetic parallelizer is discussed in detail by Kruit<sup>22</sup> and Bleeker and Kruit.<sup>23</sup> After the magnetic aperture the electrons enter a 90° electrostatic deflector, with a 20-mm central radius. This deflector is placed in an extension between condenser and objective lens and has a hole in the outer sphere for the primary electrons to pass through. Electrostatic lenses guide the secondary electrons to a 180° concentric hemispherical analyzer, which has a central radius of 140 mm.

To ensure good parallelization the objective lens and parallelization coil current are set to their computed values. The specimen, which is mounted on an insulated holder, is adjusted in height to ensure focusing on the TEM screen. Fine focusing is still done with the objective lens current. The condenser lenses are used to focus a spot on the sample. The spotsize on the specimen is only of the order of 1  $\mu\text{m}$ , due to a nonoptimized condenser system and objective lens.

Scanning in energy for the secondary-electron analysis is performed by raising the intermediate lenses, the 90° deflector and the 180° analyzer all with the same potential. This also means that the primary electrons are accelerated or decelerated while they pass the 90° deflector. The actual deflection they experience will therefore change with the selected secondary-electron energy. Feedback of the energy scan to the condenser deflectors minimizes this effect.

In a coincidence system, secondary-electron analysis must be performed with preservation of the timing information. Especially slow secondary electrons which leave the sample under different angles, can experience different flight times toward the detector. To minimize this effect the sample is negatively biased (-18 V). Before the end of the parallelizer the electrons are accelerated (or decelerated) to the central potential of the 90° deflector. The pass energy for this deflector is set to 350 eV. The electrostatic lens is adjusted to get as many electrons through the entrance slit of the 180° analyzer as possible. Just before the analyzer they are slowed down to the pass energy of 100 eV.

Figure 5.2 shows an example of a secondary-electron spectrum of a thin carbon foil. This spectrum is obtained with the analyzer slits almost closed, so that the energy resolution is well below the intrinsic width of the secondary-electron distribution. In Fig. 5.3 a larger range secondary-electron spectrum is shown at a resolution of  $\approx 5$  eV. Due to the large dynamic range that must be covered, the vertical scale is logarithmic. At about 260 eV the carbon *KVV* Auger feature can be distinguished.

EELS is performed in low camera length diffraction mode or EELS image coupling mode, which enables large scattering angles to be accepted. The GATAN 607 serial EELS system is adjusted in the usual way for a given energy resolution. Since relatively long collection times can be necessary in coincidence methods, drifts must be minimized. With some care drifts could be kept as low as 1 eV per

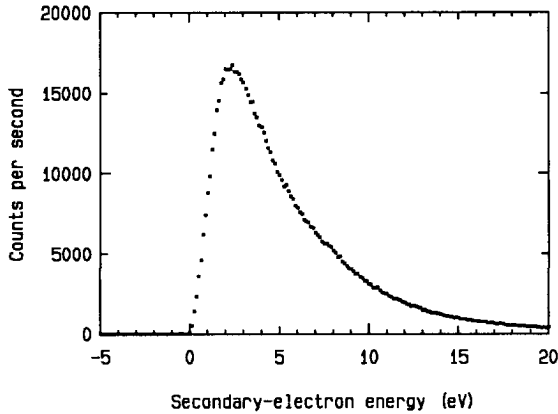


Fig. 5.2: Low-energy-range secondary electron spectrum from thin amorphous carbon film.

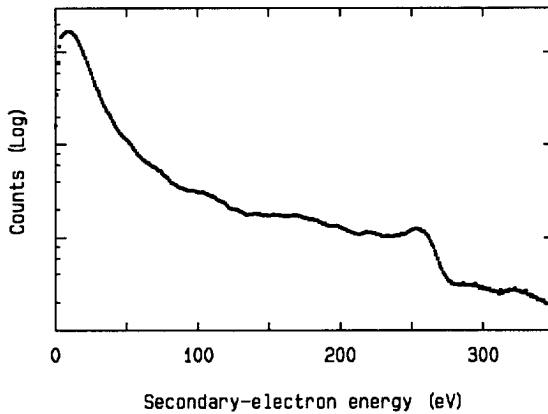


Fig. 5.3: Semilogarithmic plot of the secondary-electron spectrum (0-350 eV) from thin amorphous carbon film.

10 min.

The coincidence setup required for the described measurements is shown in Fig. 5.4. Of course each channel must have single-electron counting detectors. The secondary-electron analyzer is equipped with a microchannel plate detector (chevron mounted), whereas the EELS detector makes use of a plastic scintillator with photomultiplier. Electrical pulses from the anode behind the microchannel plate and from the photomultiplier of the EELS detector are led toward a time-to-amplitude converter (TAC), with a built-in single-channel analyzer (SCA). Because the anode behind the microchannel plate is at several kilovolts, an isolation trans-

## 5. Results of the Measurements

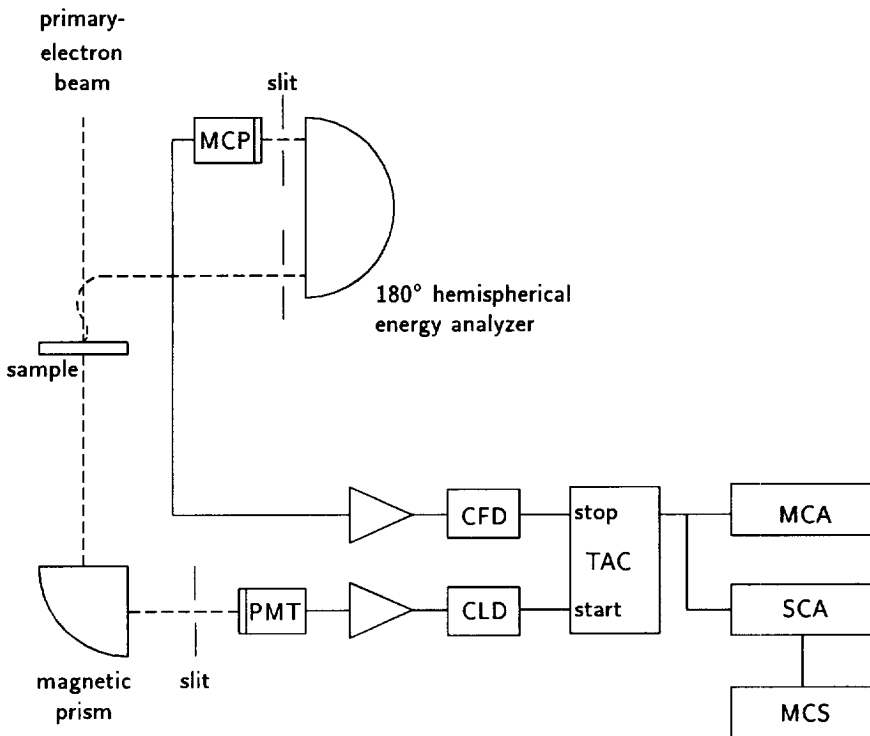


Fig. 5.4: Schematic coincidence setup. MCP is the microchannel plate, PMT is the photomultiplier tube, CFD is the constant fraction discriminator, CLD is the constant level discriminator, TAC is the time-to-amplitude converter, MCA is the multichannel analyzer, SCA is the single channel analyzer, and MCS is the multichannel scaler.

former is used to bring the signal to ground level. A twisted pair of Teflon-coated wire-wrap wires, which have been tested to withstand voltage differences of over 5 kV, is wound several times around a ferrite coil, to give good high-frequency performance. Because of the small signal a preamplifier is mounted almost directly behind the transformer. The signal is then led to a constant fraction discriminator, which minimizes timing inaccuracies.

The EELS photomultiplier has a built in preamplifier and constant level discriminator. In the EELS control unit a 50  $\Omega$  line driver has been added, from which the signal is sent directly to the time-to-amplitude converter. A possible improvement here would be the use of a constant fraction discriminator, instead of the constant level discriminator.

To determine if coincidences occur one first has to find out the time difference

between the arrival of the electrons. For this, both detectors are set for relatively high countrates. The multichannel analyzer (MCA) accepts pulses from the TAC which is set for a large time range, using a low primary beam current and long collecting times. The background in the spectrum represents the detection of noncoincident, unrelated electrons. A peak in the MCA spectrum represents the true coincidences. Once the peak is found, a narrow timescale such as shown in Fig. 5.5 can be chosen. This spectrum was obtained with narrow analyzer slits as

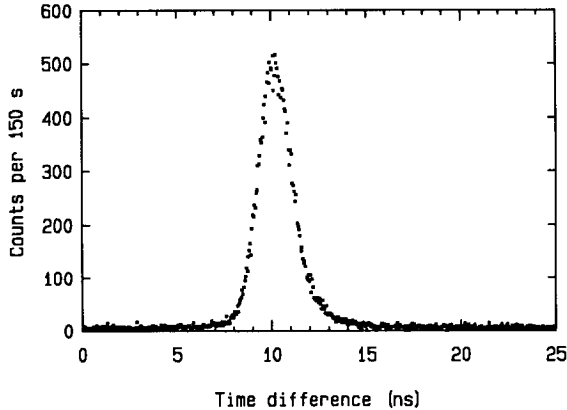


Fig. 5.5: MCA time difference spectrum, showing difference in arrival of secondary electrons with respect to their “creator” energy-loss electrons. Secondary electrons have an energy of 2.5 eV (this represents the maximum in Fig. 5.2). The energy loss selected is  $\approx 16$  eV.

in Fig. 5.2. The remaining full width at half maximum (FWHM) of 2.1 nsec, and base width of about 6 nsec, is attributed to different opening angles (leading to different flightpaths in the analyzer) and the energy range that is selected (different velocities).

To collect a coincidence spectrum the single channel analyzer (SCA) is set to accept all counts that fall in the time window, given by the base width of the true coincidence peak. The data are then collected in the multichannel scaler (MCS). Pulses output by the MCS, signifying the step to a next data channel, are used to scan the EELS spectrometer. A spectrum collected in this way will suffer from an energy-dependent background of false coincidences. The false coincidence count rate  $R_F$  is given by the count rate of the secondary-electron signal  $R_{SE}$  multiplied by the fraction of time that the time window is open, which is the count rate of the EELS signal  $R_{EELS}$  times the time window  $\tau$ , or  $R_F = R_{SE}R_{EELS}\tau$ . This means that  $R_F$  has a quadratic relationship with the primary beam current  $I_p$ , whereas the true coincidence count rate  $R_T$ , just like  $R_{SE}$  and  $R_{EELS}$  behaves linearly with  $I_p$ . Together with the need for low primary beam current, it is important to keep  $\tau$  as low as possible.

## 5. Results of the Measurements

To determine the false coincidence background, a separate scan with different time-window setting can be made. Alternatively, this spectrum could be collected simultaneously with a differently set SCA with accompanying MCS. Since no second SCA or MCA was available, an alternate method was employed. The MCA time spectrum is recorded for a given dwell time, and the data are transferred to a microcomputer (IBM AT). In the computer a fast analysis of the time spectrum yields both true and false counts, which are both stored in memory. The scan pulses, normally output by the MCS, are now provided by the microcomputer program. They restart the process for the next energy channel. In this way the effects of primary-beam current fluctuations, or drifts of the EELS analyzer are similar for the true and false coincidence spectra.

### 5.3. Results and Discussion

With the secondary-electron analyzer set to accept all secondary electrons with energy below 5 eV and the energy resolution of the EELS detector approximately set for 5 eV, a coincidence EELS spectrum is recorded. This spectrum, collected during 20 sweeps with a dwell time of 0.1 sec per channel, is shown in Fig. 5.6. Here no false coincidence background has been subtracted. Also shown is a nor-

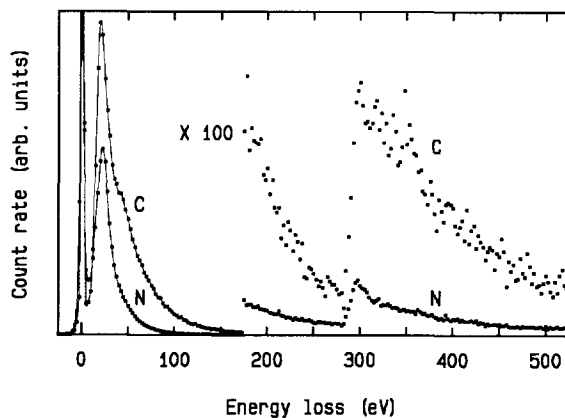


Fig. 5.6: Large energy range (0-500 eV) coincident (*C*) and normal (*N*) energy-loss spectra. The  $180^\circ$  analyzer is set for the maximum of the secondary-electron distribution. The normal EELS spectrum is shown on a 200 times reduced countrate scale. Vertical full scale represents 10 000 counts per second. At 175 eV a gain change is introduced to show both the low and high range of the spectra. For both spectra the gain change is 100 $\times$ .

mal EELS spectrum collected during two sweeps with equal dwell time. We observe some interesting differences. Just above the (false) zero loss peak the coincidence

spectrum exhibits a sharper rising edge. The largest countrates occur for energy losses around 25 eV, the plasmon energy for carbon. Toward the  $K$  edge of carbon the countrate gradually decreases. However, the slope in both spectra differs considerably. The carbon  $K$  edge in the coincidence spectrum, admitting that it is more noisy, has a slightly better jump ratio, although in some measurements (not shown here) the opposite effect occurred. After the edge the coincidence spectrum does not drop as quickly as the normal spectrum. Some of the differences might be attributed to the relatively long exposure rates, which can cause beam-induced contamination. To minimize this effect, different specimen positions were selected in between the sweeps that composed the coincidence spectrum. The uniformness of the film has been checked qualitatively.

To estimate the thickness  $t$  of the film, the regular EELS data can be used. Normally<sup>24</sup> one would compute  $t$  from  $t = -\ln(I_{z1}/I_{\text{tot}})\lambda$ , where  $I_{z1}$  is the zero loss intensity,  $I_{\text{tot}}$  the total intensity, and  $\lambda$  the mean free path of the primary electrons for all possible energy losses. Since the height of the zero loss peak might be severely underestimated due to dead-time effects in the pulse counting process, we chose not to use this method. Instead the data have been fitted to a model function. The model is based on the jellium model for plasmon excitation (Egerton,<sup>24</sup> Eq. (3.43)):

$$I_1(E) \propto \frac{E_p^2 E \Delta E_p}{(E^2 - E_p^2)^2 + (E \Delta E_p)^2} \quad (5.1)$$

Fitting the EELS spectrum by means of a Levenberg-Marquardt<sup>25</sup> method yields the plasmon energy  $E_p$  (24.1 eV) and the FWHM of the plasmon distribution  $\Delta E_p$  (18.3 eV).

From the found distribution a double-scattering distribution is computed by means of (self-) convolution and the fitting procedure is repeated, but now with double scattering included. This iterative process yields the intensity of single- ( $J_1$ ) and double- ( $J_2$ ) scattering distribution, from which the thickness can be estimated by  $t = J_2/(2J_1)\lambda$  (cf., Egerton,<sup>24</sup> Eq. (4.1)). For the spectrum of Fig. 5.6 this yields  $t = 0.25\lambda$ .

The mean free path  $\lambda$  is a mean free path for scattering events that are actually recorded and therefore  $\lambda$  depends on the effective collection angle. In this experiment there is no objective aperture that limits the collection angle. We expect to collect about 10 mrad. For energy losses up to 50 eV (Egerton,<sup>24</sup> Fig. 3.15) we find  $\lambda \approx 70$  nm, which gives  $t \approx 18$  nm.

A different presentation of the data of Fig. 5.6 is given in Fig. 5.7. Here the ratio of the coincidence and normal EELS spectrum is shown, which gives a measure for the number of secondary electrons that are produced and detected per detected energy-loss event. The overall trend, from  $\approx 25$  eV up to  $\approx 125$  eV and also directly following the carbon  $K$ -edge, is a linear increase in the probability of secondary-electron production, with energy loss. This trend is plausible, since with higher-energy losses more energy is available for the creation of slow secondary electrons, which agrees with the cascade description.<sup>26</sup> The exact processes that

## 5. Results of the Measurements

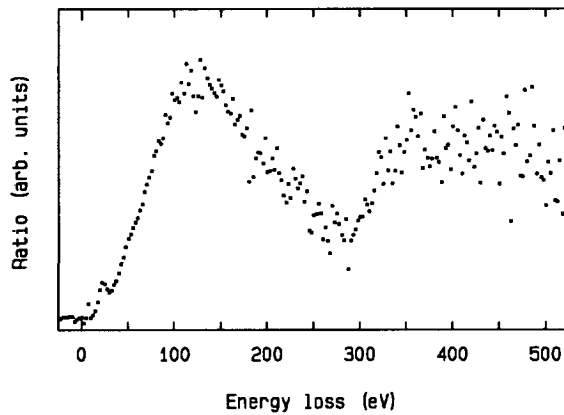


Fig. 5.7: Ratio of the two spectra in Fig. 5.6 showing the probability of low-energy secondary-electron production for a given energy-loss event. The  $180^\circ$  analyzer is set for the maximum of the secondary electron distribution. Vertical full scale represents a ratio of 6.25 %.

occur in the specimen will determine in what way and to what extent this energy is really available for secondary-electron production and emission. Emission of these secondary electrons depends on the depth in the film where the scattering takes place, the scattering directions and the mean free paths of possibly involved intermediate products. The drop in the ratio spectrum at  $\approx 125$  eV may be a thickness-dependent effect. Maybe on average the faster secondary electrons, which are directly knocked out of their atomic orbits, travel more forward (away from the top surface). This way they reach deeper before they can start a cascade that yields a slow secondary electron. The fact that different positions for the maximum in the ratio spectrum were found (not shown here) suggests the need for further studies.

In relation to the delocalization problems in scanning electron microscopy, the coincident energy-loss spectrum can be an interesting result. The different contributions to the secondary-electron detector signal can be related to the original energy-loss processes of which the degree of localization is well understood. It should then be possible to find the secondary-electron delocalization profile by summing the expected delocalization profiles for given energy loss (including the cascade effect) scaled with the height of the coincidence EELS spectrum.

We will now focus our attention to the low-energy part of the spectrum. A coincidence spectrum, collected with better energy resolution for both detectors (approximately 1.5 eV) in which the  $180^\circ$  analyzer is set for the maximum of the secondary-electron distribution, is shown in Fig. 5.8. Also shown is the normal EELS spectrum. The accompanying ratio spectrum is shown in Fig. 5.9. These data are taken from a different part of the specimen, of which the thickness is



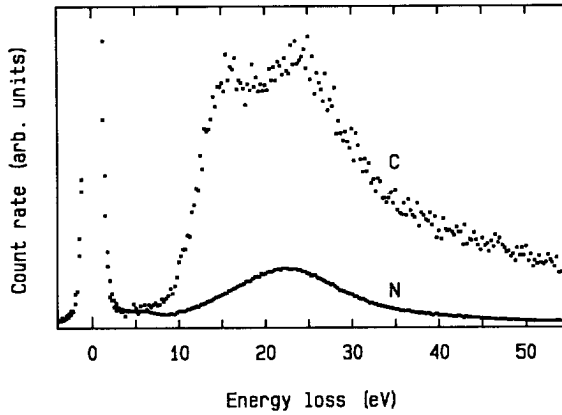


Fig. 5.8: Low-energy range coincident and normal energy-loss spectrum. The coincidence spectrum (*C*) represents energy-loss events coincident with the detection of secondary electrons of the maximum of the secondary-electron distribution. The normal energy-loss spectrum (*N*) is shown on the scale of the false coincidences as they appear in the coincidence spectrum.

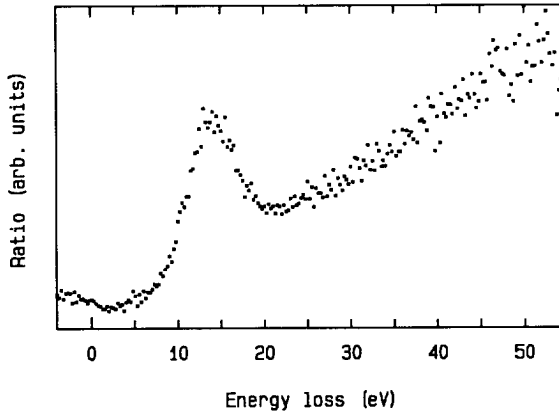


Fig. 5.9: Low-energy range ratio spectrum showing the prominent peak in the surface plasmon region and the general trend of a higher probability of low-energy secondary electron production for higher-energy-loss events.

estimated to be  $0.19\lambda$  ( $E_p = 24.1\text{ eV}$ ,  $\Delta E_p = 16.7\text{ eV}$ ). An extrapolation of the linear slope that occurs at the right of the peak crosses the horizontal axis somewhere near  $5\text{ eV}$ . We see a clearly distinguished peak with its center position at about  $14\text{-eV}$  loss and a FWHM of  $6\text{ eV}$ . Energy losses of about  $14\text{ eV}$  can be used for the excitation of surface plasmons. A decomposition of the normal EELS spec-

## 5. Results of the Measurements

trum into bulk and surface plasmons by means of a Kramer-Kronig analysis (the program KKS, described by Egerton<sup>24</sup>), yields a surface-plasmon distribution with closely matching characteristics. It is unclear if all energy of the surface plasmon must be converted to a single secondary electron (and accompanying hole), but if surface plasmons decay toward secondary electrons, roughly half of these can escape without scattering; the other half moves away to the bulk. With respect to other processes, which are not related to the surface, this gives an enhanced probability to create detectable secondary electrons.

A measure for the spatial extension of the surface plasmon<sup>27</sup> is the  $1/e$  value of the field amplitude, which is reached at a certain depth. This depth is of the order of a few nanometer but depends strongly on the relative permittivity at the surface and the energy of the plasmon. Within such a range from the surface, the surface plasmons probably dominate over the bulk plasmons. Escaping without scattering is only possible from within the escape depth. For the selected secondary electrons, Seah and Dench<sup>28</sup> give a value for the mean free path of about 3 nm. Bulk plasmons are therefore unlikely to generate unscattered secondary electrons. The fact that in the ratio spectrum no trace of enhanced secondary-electron production appears at energy losses normally attributed to bulk plasmons suggests that in their decay bulk plasmons behave exactly like those electrons that are directly hit by a primary electron and then start a cascade process.

To study how the kinetic energy of the secondary electrons influences the energy-loss coincidence spectrum, a series of measurements has been done with different settings of the  $180^\circ$  analyzer. In Fig. 5.10, 15 energy-loss coincidence spectra are shown, each collected during ten sweeps with 0.1-sec dwell time per channel. Secondary-electron energy was manually set, with  $\approx 1$ -eV steps, ranging from 1 to 15 eV. The original data were taken over a 128-eV range with 0.5-eV steps. Above 40-eV we observe no interesting features. False coincidence counts have been subtracted offline. The original EELS data recorded with these spectra gave the specimen thickness  $t = 0.1\lambda$ , the plasmon energy  $E_p = 24.9$  eV and the FWHM of the plasmon peak  $\Delta E_p = 19.2$  eV.

To analyze the data and to guide the eye along the spectra, fitting functions have been added. What we see in the spectra is a superposition of two features. One is a smooth peak, approximately 5 eV wide at half maximum, which seems to walk toward higher energy loss with higher kinetic energy of the secondary electron. This feature has been fitted by a Gaussian function. We observe that for the top ten spectra this peak shifts (on average) 1 eV toward higher energy loss with the 1 eV kinetic energy step of the selected secondary electrons. This suggests the interpretation of this feature as one that represents the emission of secondary electrons with equal binding energy, approximately 11 eV below vacuum level. In this way the feature is interpreted as a (virtual) photoelectron peak. Figure 5.11 shows the positions of the found peaks together with a line that represents a binding energy of 11 eV.

Noticeable is the slight deviation of the peak position from this linear rela-

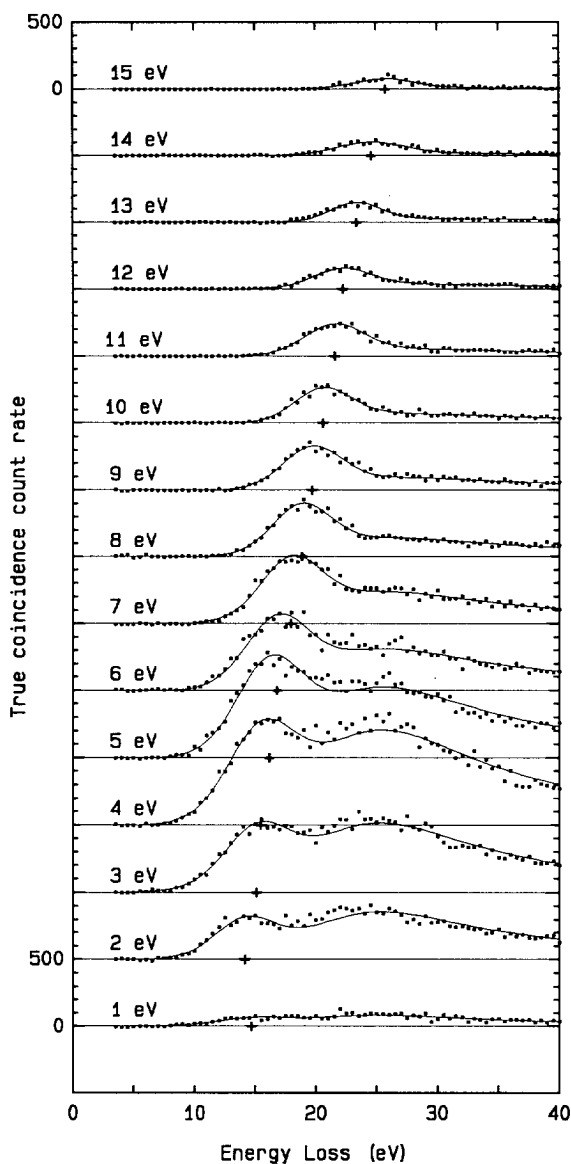


Fig. 5.10: Energy-loss coincidence spectra (shown as dots) for 15 consecutive values of the secondary-electron energy. Spectra have been vertically displaced over an equivalent of 500 counts. False coincidence counts have been subtracted. Secondary-electron energy was manually set, with  $\approx 1$ -eV steps. Fitted functions according to the model described in the text are drawn as solid curves. The position of the Gaussian peak of this fitting model is indicated on the baseline of each spectrum (+).

## 5. Results of the Measurements

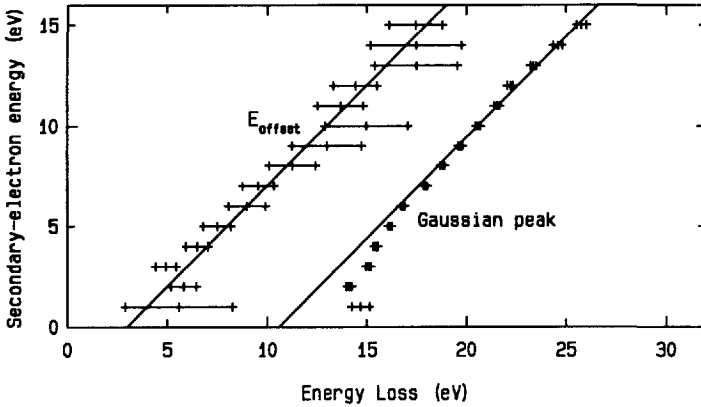


Fig. 5.11: Positions of the energy offset  $E_{\text{offset}}$  and Gaussian peak in the twodimensional coincidence spectrum, as found by the fitting procedure. Error bars indicate the 95% probability interval around the computed value. Drawn lines are for  $\Delta E - E_{\text{SE}} = 3$  and 10.6 eV, respectively.

tionship at lower kinetic energies. In fact the peak seems to stay at about 14-eV energy loss, which could indicate that the peak results from plasmon decay. The Gaussian peak then represents surface plasmons decaying into electron-hole pairs at low kinetic energies and photo electrons at higher energies. For some of the lower spectra the single-electron excitation seems enhanced by a surface plasmon excitation and the subsequent decay process.

The other feature in the spectra of Fig. 5.10 is a much wider nondescript bump. We know from Fig. 5.9 that in this region the ratio spectrum rises linearly with the energy loss scale. The second feature has therefore been fitted to a multiplication of the plasmon-loss function of Eq. (5.1) with a factor  $(E - E_{\text{offset}})$ , where  $E_{\text{offset}}$  gives the minimum energy required for secondary-electron production. Below  $E_{\text{offset}}$  this function is zero. In the fitting procedure followed for Fig. 5.10 five parameters were free: the heights of the two features, the width and position of the Gaussian peak and  $E_{\text{offset}}$ . Values found for  $E_{\text{offset}}$  are also indicated in Fig. 5.11.

Since the data are collected in a counting process, they are regarded as being Poisson distributed. The noise level on each datapoint is given by the square root of the number of counts. This forces the Levenberg-Marquardt method to "overestimate" the necessity of a good fit in regions with low count rates (and thus low absolute errors). Therefore, for some spectra the fit does not seem optimum. Some different schemes of free parameters in the fitting model can give better looking fits, but make the interpretation of such a fit less clear. At least the general trend that (disregarding the lower few spectra) the positions of the Gaussian peaks form a straight line is never missing. Small deviations of the actual peak position from this line (less than  $\pm 0.5$  eV) are attributed to the manual setting of the

analyzer energy and noise in the data. The deviations of the energy offset from a straight line are less than  $\pm 1.5$  eV.

Practical use of this and other coincidence techniques in the STEM still awaits high spatial resolution<sup>29</sup> and the clean specimen environment of a UHV microscope, which now nears completion.<sup>30</sup> With clean suitably chosen specimens other coincidence techniques are at hand. High resolution near-dipole (e, 2e) spectroscopy<sup>31</sup> and background reduction in Auger or energy-loss spectroscopy are just a few examples.

## 5.4. Acknowledgments

This work was part of a research program of the Foundation for Fundamental Research on Matter (FOM) and financially supported by the Netherlands Technology Foundation (STW), under Contract No. DTN 44-0745.

## 5.5. References

- <sup>1</sup> M. J. van der Wiel and C. E. Brion, *Energy dependence of the photoelectron angular distribution parameter for Ne 2p electrons, measured in an electron-electron coincidence experiment*, J. Electron Spectrosc. Relat. Phenom. **1**, 439 (1972/73).
- <sup>2</sup> J. D. Jackson, *Classical Electrodynamics*, p. 719. (Wiley, New York, 1962).
- <sup>3</sup> L. Ungier and T. D. Thomas, *Near threshold excitation of KVV Auger spectra in carbon monoxide using electron-electron coincidence spectroscopy*, J. Chem. Phys. **82**, 3146 (1985).
- <sup>4</sup> I. E. McCarthy and E. Weigold, *Wavefunction mapping in collision experiments*, Rep. Prog. Phys. **51**, 299 (1988).
- <sup>5</sup> H. W. Haak, G. A. Sawatzky, L. Ungier, J. K. Gimzewski and T. D. Thomas, *Core-level electron-electron coincidence spectroscopy*, Rev. Sci. Instrum. **55**, 696 (1984).
- <sup>6</sup> A. L. Ritter, J. R. Dennison and R. Jones, *Spectral momentum density of amorphous carbon from (e, 2e) spectroscopy*, Phys. Rev. Lett. **53**, 2054 (1984).
- <sup>7</sup> Chao Gao, A. L. Ritter, J. R. Dennison and N. A. W. Holzwarth, *Spectral momentum density of graphite from (e, 2e) spectroscopy: Comparison with first-principles calculation*, Phys. Rev. B **37**, 3914 (1988).
- <sup>8</sup> P. Hayes, M. A. Bennett, J. Flexmann and J. F. Williams, *Symmetric transmission electron momentum (e, 2e) spectroscopy of an aluminum-aluminum oxide thin foil*, Phys. Rev. B **38**, 13371 (1988).
- <sup>9</sup> P. Hayes, J. F. Williams and J. Flexmann, *Transmission (e, 2e) coincidence measurements of thin evaporated carbon, graphite, and aluminum-aluminum oxide thin foils*, Phys. Rev. B **43**, 1928 (1991).
- <sup>10</sup> P. Kruit, H. Shuman and A. P. Somlyo, *Detection of x-rays and electron energy loss events in time coincidence*, Ultramicroscopy **13**, 205 (1984).
- <sup>11</sup> D. Voreades, *Secondary electron emission from thin carbon films*, Surf. Sci. **60**, 325 (1976).
- <sup>12</sup> D. B. Wittry, *Use of coincidence techniques to improve the detection limits of electron spectroscopy in STEM*, Ultramicroscopy **1**, 297 (1976).

## 5. Results of the Measurements

- <sup>13</sup> J. Cazaux, *Detection limits in Auger electron spectroscopy*, Surf. Sci. **140**, 85 (1984).
- <sup>14</sup> P. Kruit and J. A. Venables, *High-spatial-resolution surface-sensitive electron spectroscopy using a magnetic parallelizer*, Ultramicroscopy **25**, 183 (1988).
- <sup>15</sup> J. Liu and J. M. Cowley, *High resolution secondary electron imaging in a scanning transmission electron microscopy instrument*, Scanning Microscopy **2**, 65 (1988).
- <sup>16</sup> J. Liu and J. M. Cowley, *Contrast and resolution of secondary electron images in a scanning transmission electron microscope*, Scanning Microscopy **2**, 1957 (1988).
- <sup>17</sup> A. L. Bleloch, A. Howie and R. H. Milne, *High resolution secondary electron imaging and spectroscopy*, Ultramicroscopy **31**, 99 (1989).
- <sup>18</sup> N. B. Gornyi, *Plasmon photoelectric and secondary electron emission*, Fiz. Tverd. Tela **8**, 1939 (1966), [Sov. Phys. Solid State **8**, 1535 (1966)].
- <sup>19</sup> R. F. Willis, B. Fitton and G. S. Painter, *Secondary-electron emission spectroscopy and the observation of high-energy excited states in graphite: Theory and experiment*, Phys. Rev. B **9**, 1926 (1974).
- <sup>20</sup> N. B. Gornyi and E. N. Makarova, *Interpretation of the experimental data on secondary electron emission from thin carbon films*, Fiz. Tverd. Tela **21**, 2187 (1979), [Sov. Phys. Solid State **21**, 1258 (1979)].
- <sup>21</sup> P. Kruit, A. J. Bleeker and F. J. Pijper, *High resolution Auger analysis in STEM*, in *Proceedings of European Congress on Electron Microscopy, York, 1988*, edited by P. J. Goodhew and H. G. Dickinson, Vol. 1 of *Institute of Physics Conference Series*, No. 93, p. 249, London, 1988. IOP.
- <sup>22</sup> P. Kruit, *Magnetic Through-the-lens Detection in Electron Microscopy and Spectroscopy, Part 1*, Vol. 12 of *Advances in Optical and Electron Microscopy*, p. 93. (Academic Press Limited, London, 1991).
- <sup>23</sup> A. J. Bleeker and P. Kruit, *The magnetic parallelizer as an optical element for Auger electrons: Further characterization*, Nucl. Instrum. Methods A **298**, 269 (1990).
- <sup>24</sup> R. F. Egerton, *Electron Energy-Loss Spectroscopy in the Electron Microscope*. (Plenum Press, New York, 1986).
- <sup>25</sup> W. H. Press, B. P. Flannery, S. A. Teukolsky and W. T. Vetterling, *Numerical Recipes: The Art of Scientific Computing*. (Cambridge University Press, Cambridge, England, 1986).
- <sup>26</sup> P. A. Wolff, *Theory of secondary electron cascade in metals*, Phys. Rev. **95**, 56 (1954).
- <sup>27</sup> H. Raether, *Surface Plasmons on Smooth and Rough Surfaces and on Gratings*, Vol. 111 of *Springer Tracts in Modern Physics*. (Springer-Verlag, Berlin, 1988).
- <sup>28</sup> M. P. Seah and W. A. Dench, *Quantitative electron spectroscopy of surfaces: A standard data base for electron inelastic mean free paths in solids*, Surf. Interface Anal. **1**, 2 (1979).
- <sup>29</sup> A. J. Bleeker and P. Kruit, *A condenser objective lens with asymmetric polepieces to facilitate the extraction of secondary and Auger electrons*, Rev. Sci. Instrum. **62**, 350 (1991).
- <sup>30</sup> A. J. Bleeker. *Optical and mechanical design for 1 nm resolution Auger spectroscopy in an Electron Microscope*. PhD thesis, Delft University of Technology, June 1991.
- <sup>31</sup> F. J. Pijper, A. J. Bleeker, R. J. Endert and P. Kruit, *Prospects for photo electron spectroscopy in a scanning transmission electron microscope*, Scanning Microscopy **3**, 65 (1989).

## 6. Conclusions and Perspectives

### 6.1. Conclusions

This research shows that there are exciting possibilities to perform coincidence spectroscopy in a STEM. It concentrates on coincidence experiments between fast energy-loss electrons and emitted electrons released by them. It investigates under what conditions coincidence spectroscopy yields best results.

From the research described in this thesis several conclusions can be drawn. First we may conclude that coincidence spectroscopy is an interesting new technique. It provides a direct connection between electron emission and fast-electron energy loss. The energy lost by the fast electron and the energy of the emitted electron form a 2-dimensional spectrum (Fig. 1.2). The individual techniques only provide a 1-dimensional projection of this spectrum along one of its axes. A full 2-dimensional coincidence spectrum will simplify interpretation of spectral features.

The coincidence technique provides several new possibilities. Coincidence spectroscopy can provide high spatial resolution elemental information, down to single atom identification, provided that the sample can withstand high electron doses. From virtual-photo electron spectroscopy both elemental and chemical shift information can be deduced. It is possible to identify specific Auger features, by distinguishing between excitation and ionization losses. Bulk and surface plasmon decay via emission of secondary electrons can be studied. A strong effect of electron emission at surface plasmon losses was observed in carbon foils. Spatial resolution in secondary-electron imaging can be improved. Energy-loss spectroscopy can be made surface sensitive. Furthermore, since it is possible to find absolute detection efficiencies of both detectors, absolute cross sections can be found.

An important conclusion is that coincidence spectroscopy can be realized in a STEM. This thesis shows that the choice of a STEM for these experiments is a good one. The STEM provides conditions that are favorable for coincidence experiments. It combines high acceleration voltage operation with high spatial resolution and high collection efficiency.

High acceleration voltage is accompanied with high brightness of the source and therefore high current density in the probe. Due to high current density the spatial resolution can be better, which lowers the amount of atoms in the analyzed volume. The signal-to-noise ratio, which is required to tell if a species is present, is then decreased for a given probing volume.

The high collection efficiency for energy-loss electrons is caused by increased

forward momentum, which favors scattering at smaller angles. Despite lower total cross sections with increased acceleration voltage, the net effect on the product of current density and energy-differential cross section is positive (Fig. 3.3a).

High collection efficiency for emitted electrons is possible with a magnetic parallelizer objective lens. In the high magnetic field the electrons start spiraling and the parallelizer guides electrons away from the specimen to a position where they can be separated from the fast electrons. In this process almost all motion perpendicular to the magnetic field is converted into motion parallel to the field (parallelization), which enables large acceptance angles. The focusing properties of the objective lens (for the fast electrons) are not seriously influenced by the parallelizer field. A deflector is required to separate (slow) emitted electrons from the (fast) primary electrons. This will have some effect on probe formation, but we expect no unacceptable degradation.

The fact that the sample is a thin solid sample does not play a very important role in the discussion of instrumental parameters. It is therefore suggested that the principle of coincidence spectroscopy in the STEM, as discussed in this thesis, could be applicable to gas-phase coincidence experiments as well. Since the density in a gas is much lower than in a solid a much larger sampling volume will be required. No lateral resolution is required and therefore probe size and probe current can be much higher. To perform such an experiment, the STEM sample should be replaced with a small gas jet. Main instrumental complication will be the requirement of an effective differential pumping system.

Angular emission distribution functions for single-electron scattering events have been computed based on existing theoretical models. This was done for emitted electrons of a given energy, which have been released in a *K*-shell ionization energy-loss process. The scattering angle involved in this process was limited to a value, which represents an actual collection aperture. The distributions showed only a slight preference for forward emission. The inclusion of workfunction effects causes the 'reflection' of some of the emitted electrons on the solid/vacuum interface. The fraction of electrons that can escape from the top or bottom surface, of course depends on the ratio of emitted-electron energy and workfunction. As an example, we have studied the emission of 30-eV electrons, released from the carbon *K*-shell by 100-keV electrons, scattering up to 50 mrad. About 37% and 40% are expected to escape from top and bottom surface respectively.

Electron-impact excitation has been compared with photon excitation. The cross section for photon excitation is larger by five to six orders of magnitude (Fig. 2.14b). On the other hand the brightness of available photon sources is many orders of magnitude smaller than that of electron sources. The comparison of spectral-brightness data for small sample areas shows that the number of virtual photons in a STEM (equipped with a Schottky FEG) compares well with the number of 'true' x-ray photons in some of the brightest synchrotron radiation sources (Fig. 2.15a). A comparison, which includes usable solid angle for small-probe formation (1 nm), turns out even more in favor of the electron-impact case



(Fig. 2.15b). The possibility to simulate many parallel photon energies by parallel energy-loss detection in a coincidence setup, may give a further advantage.

Energy-loss measurement in the STEM can be done using a magnetic sector analyzer. For 100-keV electrons, at an energy resolution of 1 eV, this is possible with acceptance angles of over 50 mrad. Both objective-lens and spectrometer aberrations must be considered for setting the imaging conditions of the post-specimen part. Due to higher dispersion at lower acceleration voltages, acceptance angle or energy resolution can be better, but not enough to compensate for the wider scattering distribution.

Emitted electrons with energies up to 2 keV can be collected with a combination of magnetic parallelizer, 90° deflector, transfer optics and hemispherical analyzer. The parallelizer keeps electrons close to the optical axis, but acts a little differently for different energies. For each energy value the phase space is filled differently. For energies up to  $\approx 300$  eV, the collection angle can be  $2\pi$  solid angle, (at 1-eV energy resolution), equivalent to 100% transmission (Fig. 3.14). For parallel detection with more than eight detector channels, the upper energy limit for 100% transmission is decreased. The main advantage of spectra collected with 100% transmission is the simple interpretation of the spectra.

Operation at lower transmission values is also possible, and allows for more parallel detector channels or improved energy resolution. Computations based on a homogeneously filled phase space predict a small increase in detected signal for this mode of operation (at high energies, Fig. 3.13). Cutting off the outer part of a nonhomogeneously filled phase space results in additional intensity variations in the spectrum that are related to the parallelizer operation. Intensity variations are also present in the 100% transmission mode in the form of energy resolution variations, but they can in principle be low pass filtered.

At lower transmission values the spectrometer can be operated at constant pass energy and constant energy resolution. Constant pass energy operation minimizes adjustments on the spectrometer settings. Constant energy resolution then implies that each detector channel keeps representing the same spectral width, while scanning the spectrum. At 100% transmission operation, constant energy resolution is only possible by effectively changing this width. The emission spectrum should be computed by weighted summation of several adjacent channels, where the weights vary while scanning the spectrum.

For an idealized parallelizer-spectrometer combination, the transmission function of a homogeneous emission distribution was compared with a more realistic cosine emission distribution. The cosine distribution shows a little better transmission characteristics.

A deflector and lens system are used for transferring the electrons from the parallelizer to the spectrometer. This transfer optics must be designed to operate at a large range of magnifications and operating energies. Aberrations of the transfer optics can degrade energy resolution and/or transmission.

By placing a detector at the spectrometer exit plane, post-spectrometer op-

tics can be omitted. For practical energy resolution values, the spectrometer pass energy approximately coincides with maximum detection efficiency of MCP-based detectors.

For single-channel coincidence experiments we used a slit-scintillator-PMT detector for EELS and a MCP for emitted-electron spectroscopy. Parallel detectors for both slow (emitted) electrons and (fast) energy-loss electrons are expected to be based on MCPs. For fast electrons an intermediate conversion seems inevitable, to assure high detection efficiencies. The maximum count rate of MCP-based detectors is determined by the recovery time after charge depletion of the micro channels and the number of available channels. For a 96-strip detector a total countrate of  $5.5 \times 10^6$  cts/sec is estimated.

Several detection schemes for parallel detectors have been discussed. The most promising is the one in which several detector strips are connected to individual amplifiers and the timing signal is available from a shared output. By compensating for differences in flight time, associated to different detector channels, determining the time difference can be made almost as fast as the time resolution itself. High countrate performance will then be limited by data transport to memory.

The quality of the coincidence spectra is determined by the level of true and false signal components. For a given measurement time or dose density, the signal-to-noise ratio of the true signal increases with the square root of the probe current up to some value above which no improvement is possible (Fig. 3.24). For a given total dose the signal-to-noise ratio is maximum at low probe currents (at very long measurement times), and slowly decreases at higher probe currents (Fig. 3.25a).

For the smallest probesizes it was computed that the coincidence signal of single atoms on top of a surface has adequate signal-to-noise ratio to enable single-atom identification. The sample should be very stable to survive the accompanying electron bombardment. The computations show that both with FEG and  $LaB_6$  emitters the signal-to-noise ratio is about 20 times higher than obtainable with normal EELS (Fig. 3.26). By using wider energy windows in both analyzers, the signal-to-noise ratio can be improved for probe sizes below 1 nm (Fig. 3.28).

Coincidence measurements have been performed in a prototype experiment. Because the instrument lacked UHV conditions and did not have very high spatial resolution, only a limited choice of possible applications could be tested. The time resolution of our coincidence experiment was shown to be 2.1 ns FWHM and 6 ns base width. This was for emitted electrons of 2.5 eV, at a pass energy of 100 eV inside the CHA, with slits almost closed, at an acceptance angle of about 65 mrad.

An EELS spectrum, taken in coincidence with slow secondary electrons (0–5 eV), is clearly different from a regular EELS spectrum. The differences are best interpreted in a ratio spectrum, showing the probability of secondary-electron generation and detection per detected energy-loss event. Over the range from 25–125-eV loss and directly following the carbon *K*-edge, this probability rises with energy loss, which agrees with the cascade description. The drop at 125-eV loss is possibly a thickness dependent effect, but it also might be caused by noise components in

the regular EELS spectrum, mainly affecting the signal just below the  $K$ -edge. Müllejans and Bleloch<sup>1</sup> performed a comparable experiment (in coincidence with electrons emitted in the forward direction, without energy selection) and did not observe the drop. They suggested that such noise components are formed by an instrumental background. Although scattering of electrons at residual-gas particles in the post-specimen part of our microscope could have caused an instrumental background, it is also possible that the decreased jump ratio is caused by a larger acceptance angle of our EELS system. Omitting the objective-lens aperture in our experiment decreases the jump ratio by accepting a stronger contribution of small impact-parameter collisions with valence electrons. Apparently these collisions show up less pronounced in the coincidence spectrum.

At low energy ( $\approx 14$  eV) the ratio spectrum shows a very pronounced peak over a linearly rising slope. The peak is attributed to the excitation of surface plasmons. In their decay process, surface plasmons are more likely to emit electrons that can actually escape from the surface. The slope is attributed to an increased amount of energy available in the decay process, leading to more electrons that can be involved in a cascade process.

A scan of emitted-electron energy shows a linear shift of the offset of the slope. The offset reflects the difference between energy loss and the sum of emitted-electron energy and workfunction. The peak in the ratio spectrum also shifts with the scan in emitted-electron energy, and appears to reflect direct emission of valence electrons (virtual-photo electrons). At the lowest emitted-electron energies this feature starts to deviate from the linear behavior and seems to represent an enhancement by surface-plasmon excitation and decay.

## 6.2. Perspectives

The experiments at low emitted-electron energy, which have been described in this thesis do not give definite answer to questions of secondary-electron production. For this, one should carry out more extensive studies under better controlled conditions. Under UHV conditions, the effects of different acceptance angles, specimen thicknesses and materials should be investigated. By measuring two-dimensional coincidence spectra as a function of these parameters, a more complete picture may arise. The relation between certain interaction phenomena and spectral features should become more clear. It is satisfying to notice that two of the world's leading electron microscopy laboratories have decided to work on coincidence spectroscopy and repeated some of our experiments.<sup>1,2</sup>

The non-UHV conditions in our instrument also kept us from carrying out many other possible coincidence applications, mainly at higher emitted-electron energies. In a UHV instrument these applications are expected to provide additional analytical information on the specimen under study. In addition, they may provide data on absolute detection efficiencies of the EELS and emitted-electron analyzers.

## 6. Conclusions and Perspectives

As such the coincidence technique can be a valuable tool for studying material properties.

To realize these perspectives several instrumental conditions are essential. Of course the microscope column should meet UHV requirements. For the smallest probes at high current densities the microscope should be equipped with a high-brightness FEG. The objective lens should be of the parallelizer type and have low probe-forming and imaging aberrations. The deflector for separation of fast and emitted electrons should ideally be operated at fixed settings during spectrum acquisition. The (lateral) scanning system must be placed in a position where emitted-electron trajectories will not be influenced.

To enable shorter data-acquisition times and reduce total dose on samples the coincidence setup should be based on parallel detection. Analyzers and detectors should be designed for parallel detection and low background signals. Soft- and hardware should be designed to handle the data-acquisition system of a parallel-parallel coincidence setup.

Obviously, all these improvements add up to a large effort. Presently a large part of these improvements have been incorporated and the ideal microscope for coincidence spectroscopy is almost finished. I hope the work described in this thesis demonstrates that it is a worthwhile effort: it will be a unique instrument!

### 6.3. References

- <sup>1</sup> H. Müllejans and A. L. Bleloch, *Ratio between the energy-loss spectrum in coincidence with secondary electrons and the normal energy-loss spectrum for thin carbon films in the carbon K-edge region*, Phys. Rev. B **46**, 8597 (1992).
- <sup>2</sup> M. R. Scheinfein, J. Drucker and J. K. Weiss, *Secondary-electron production pathways determined by coincidence electron spectroscopy*, Phys. Rev. B **47**, 4068 (1993).

## Summary

An important innovation in scanning transmission electron microscopy (STEM) has opened the possibility for efficient analysis of electrons released from the specimen. The electrons are released by collisions of high-energy primary electrons, which lose energy in these collisions. Spectroscopy of these energy losses is a well-based analytical technique. In this research those two techniques are combined. By using coincidence techniques one can determine if electrons that are detected simultaneously in both analyzers originate from a single scattering event.

Possible applications of this new technique are described in this thesis. The energy, lost by the primary electron and transferred to the emitted electron, can be considered as a virtual photon. Analysis of emitted virtual-photo electrons yields a virtual-photo electron spectrum, which contains elemental as well as chemical information. By selecting a different energy loss, the virtual-photon energy can be tuned. This tunability is also found in synchrotron radiation sources.

Performing Auger spectroscopy, in coincidence with energy losses which belong to inner-shell excitation or ionization, can offer good background reduction compared to regular Auger spectroscopy. Above that, certain spectral features can be identified more easily. Selection of specific well-localized energy-loss processes, in coincidence with secondary electrons, can provide improved spatial resolution for secondary-electron imaging techniques. Furthermore, one can study what processes play a role in secondary-electron production.

Background reduction can also be achieved in energy-loss spectra taken in coincidence with specific Auger electrons. The energy-loss spectrum becomes very surface sensitive because of the limited escape depth of emitted electrons. In combination with the very small diameter of the primary-electron beam at the position of the specimen (order of 1 nm) this technique yields information from very small volumes. Because of good background reduction it should become possible to demonstrate the presence of individual atoms within such a volume.

The coincidence technique can give absolute detection efficiencies and with that also absolute cross sections.

An analysis of scattering processes with bound electrons was made to determine the angular emission probability of emitted electrons. Only those processes are included for which the scattering angle of the primary electron is smaller than the acceptance angle of the energy-loss detector. Especially for emitted electrons with low energy the workfunction barrier has a strong influence on the angular distribution.

## Summary

Comparison of coincidence spectroscopy with photo-absorption spectroscopy shows that the number of (virtual) photons that can be realized in a focussed STEM reaches comparable values to the number of true x-ray photons from synchrotron radiation sources that can be focussed in a similar spot. However, spatial resolution of x-ray systems cannot compete with electron-based system.

Several instrumental aspects which play a role in coincidence spectroscopy are discussed in Ch. 3. High primary-electron energies are preferred because faster electrons are scattered over smaller angles, which enables easier detection.

The detection system for emitted electrons can be operated in several modes. Several options are discussed and optimized for the coincidence technique. The signal-to-noise ratio of the coincidence signal is derived for several experimental conditions. Even for cases where a single atom is present on top of a background of different material, the signal-to-noise ratio is sufficient to demonstrate the presence of that atom. The specimen should be able to withstand high electron doses.

Chapter 4 describes the experimental microscope that has been used for the experiments described in Ch. 5. Despite the lack of ultrahigh vacuum conditions, several interesting measurements have been done. Comparison of a regular and coincident energy-loss spectrum shows that especially surface plasmons have increased probability of electron emission. The probability for emission of electrons with low energy is a linear function of primary-electron energy loss. In the low-energy region of a 2-dimensional coincidence spectrum a constant binding-energy feature is observed which shows the virtual-photo electrons.

Due to the lack of ultrahigh vacuum conditions and high spatial resolution in our experimental microscope, many possible applications could not yet be studied. Presently, in our laboratory tests are in progress on a microscope which does fulfil these conditions. Above that, several improvements have been implemented, some of which were based on this research.

Hopefully this thesis may contribute to a better understanding and realization of optimum conditions for coincidence spectroscopy.

## Samenvatting

Een belangrijke innovatie in de raster transmissie elektronen microscoop (STEM) heeft het mogelijk gemaakt om de elektronen die in het preparaat worden vrijgemaakt met hoge efficiëntie te kunnen analyseren. Deze elektronen worden vrijgemaakt door botsingen van hoog-energetische primaire elektronen, die daarbij energie verliezen. Het meten van deze energieverliezen is een bestaande analysetechniek die in dit onderzoek wordt gecombineerd met de analyse van uitgezonden elektronen. Met behulp van coïncidentie technieken kan worden vastgesteld of de elektronen, die tegelijkertijd worden gedetecteerd in de beide analysatoren, afkomstig zijn van hetzelfde verstrooiingsproces.

In dit proefschrift wordt aangegeven welke toepassingen voor deze techniek mogelijk zijn. De hoeveelheid energie die het primaire elektron verliest en dus overdraagt aan het uitgezonden elektron, kan worden beschouwd als een virtueel foton. Analyse van de uitgezonden virtuele foto elektronen levert een virtueel-foto elektron spectrum op, wat behalve fysische informatie ook chemische bindingsinformatie kan bevatten. Door een ander energieverlies te kiezen kan de virtuele foton energie worden afgestemd, analoog aan de afstembaarheid van synchrotron stralingsbronnen.

Door Auger spectroscopie te doen in coïncidentie met energieverliezen die behoren bij binnenschil excitaties of ionisaties, is een flinke achtergrondreductie mogelijk ten opzichte van standaard Auger spectroscopie. Bovendien kunnen bepaalde pieken in het spectrum eenvoudiger worden geïdentificeerd. Door selectie van specifieke goed gelocaliseerde energieverlies processen, in coïncidentie met secundaire elektronen, is het mogelijk de plaatsresolutie van secundaire elektronen afbeeldingstechnieken te verbeteren. Bovendien kan onderzocht worden in welke mate bepaalde processen een rol spelen bij de vorming van secundaire elektronen.

Het uitvoeren van energieverlies metingen in coïncidentie met bepaalde Auger elektronen kan ook een achtergrond reductie van energieverlies spectra opleveren. Het energie verlies spectrum wordt bovendien sterk oppervlakte gevoelig, door de geringe diepte waarvandaan de vrijgemaakte elektronen het preparaat kunnen verlaten. In combinatie met de zeer kleine doorsnede die de primaire elektronenbundel op het preparaat heeft (orde van 1 nm), wordt informatie van zeer kleine volumina verkregen. Door de goede achtergrond reductie moet het mogelijk zijn de aanwezigheid van individuele atomen binnen zo'n volume aan te tonen.

De coïncidentie techniek levert de mogelijkheid om absolute detectie gevoeligheden en daarmee ook absolute werkzame doorsneden te bepalen.

Door analyse van verstrooiingsprocessen aan gebonden elektronen wordt de waarschijnlijkheid berekend van de hoekverdeling waarmee de vrijgemaakte elektronen het preparaat verlaten. Alleen die processen worden meegenomen waarbij de verstrooiingshoek van het primaire elektron binnen de acceptatiehoek van de energieverlies meting valt. Vooral voor langzame vrijgemaakte elektronen heeft de overgang naar het vacuüm een belangrijke invloed op de hoekverdeling.

De vergelijking van coïncidentie spectroscopie met fotoabsorptie spectroscopie toont aan dat de hoeveelheid (virtuele) fotonen die kan worden gerealiseerd in de gefocusseerde spot in de STEM een vergelijkbare waarde bereikt als het aantal echte röntgen fotonen, afkomstig uit synchrotron stralingsbronnen, dat kan worden gefocusseerd in een vergelijkbare spot. De plaatsresolutie die haalbaar is met röntgen straling kan echter nog niet concurreren met die voor elektronen.

In hoofdstuk 3 worden verschillende instrumentele aspecten behandeld die een rol spelen bij coïncidentie spectroscopie. Het blijkt voordelig om te werken bij hoge primaire energieën, met name doordat de elektronen daarbij over smallere hoeken worden verstrooid, zodat de detectie eenvoudiger wordt.

Het detectie systeem voor de geëmitteerde elektronen kan op verschillende manieren worden bedreven. Diverse methodes worden uitgewerkt en geoptimaliseerd voor de coïncidentie techniek. De signaal/ruis verhouding van het coïncidentie signaal wordt afgeleid voor verschillende experimentele voorwaarden. Zelfs voor detectie van een enkel atoom op een achtergrond van een ander materiaal blijkt de signaal/ruis verhouding voldoende om dat atoom aan te tonen. Wel moet het preparaat bestand zijn tegen hoge elektronen doses.

Hoofdstuk 4 behandelt de experimentele microscoop die is gebruikt voor de metingen beschreven in hoofdstuk 5. Hoewel geen ultrahog vacuum beschikbaar was konden toch interessante metingen gedaan worden. Vergelijking van een coïncident met een normaal energieverlies spectrum leert dat vooral oppervlakte plasmonen een verhoogde kans op elektronen emissie geven. Verder neemt de kans op geëmitteerde langzame elektronen lineair toe met het energieverlies van de primaire elektronen. Een 2-dimensionaal coïncidentie spectrum in het gebied van lage energieën toont een structuur die duidt op elektronen die voor de botsing gelijke bindingsenergie hadden: dit zijn de virtuele foto elektronen.

Door het ontbreken van hoogvacuum condities en hoge plaatsresolutie in de experimentele microscoop konden veel mogelijke toepassingen niet worden onderzocht. In een vervolgonderzoek wordt momenteel gewerkt aan een elektronenmicroscoop die deze condities wel heeft. Bovendien zijn in dit instrument verbeteringen aangebracht die veelal zijn gebaseerd op de bevindingen die tijdens dit onderzoek zijn gedaan.

De hoop bestaat dat dit proefschrift kan bijdragen aan het begrijpen en realiseren van condities die nodig zijn om de coïncidentie techniek optimaal te laten werken.



## Curriculum Vitae

Ik ben geboren op 9 september 1963 in Spijkenisse. Na het succesvol doorlopen van de kleuter- en basisschool begon ik in 1975 aan de 'Christelijke Scholengemeenschap Blaise Pascal' met het voorbereidend wetenschappelijk onderwijs (VWO). In 1977 verruilde ik Spijkenisse voor Terneuzen, waar ik het VWO vervolgde aan het 'Zeldenrust College'.

Daarna heb ik van 1981 tot 1987 Technische Natuurkunde gestudeerd aan de Technische Universiteit Delft. Als afstudeerrichting koos ik voor de deeltjes optica. Onder begeleiding van prof. dr. ir. K. D. van der Mast werkte ik gedurende mijn vierde jaar aan een multipool systeem ter correctie van spherische aberratie. Doel was het verhogen van de resolutie van de transmissie elektronen microscoop. In mijn vijfde jaar werd de kennis van het correctie systeem gebruikt om een nieuw type bundel vervormend systeem te ontwikkelen ten behoeve van de elektronenstraal lithografie.

Na mijn afstuderen ben ik als assistent in opleiding (AIO) gaan werken bij dezelfde vakgroep. Onder supervisie van dr. ir. P. Kruit, die later prof. van der Mast opvolgde, heb ik mij vier jaar ingezet voor het realiseren van coïncidentie spectroscopie in de elektronen microscoop. Dit werk vormt de basis voor het voor u liggende proefschrift.

In het kader van mijn vervangende dienst heb ik in 1992 en 1993 gewerkt aan de detectie van neutrale deeltjes afkomstig uit Tokamak plasma's. Dit werk werd uitgevoerd op het FOM-instituut voor Plasmafysica 'Rijnhuizen', te Nieuwegein. Op dit moment werk ik op 'Rijnhuizen' aan Thomson verstrooiing aan vrije elektronen in het Tokamak plasma.